d-Collection

A Study on Corrosion Behaviors of Ferritic/Martensitic Steels in Liquid Sodium Condition for Sodium-cooled Fast Reactor Application

Sang Hun Shin

Department of Nuclear Engineering

Graduate School of UNIST

2015

A Study on Corrosion Behaviors of Ferritic/Martensitic Steels in Liquid Sodium Condition for Sodium-cooled Fast Reactor Application

A thesis
submitted to the Graduate School of UNIST
in partial fulfillment of the
requirements for the degree of
Doctor of Philosophy of Science

Sang Hun Shin

01.19.2015
Approved by

Major Advisor
Ji Hyun Kim

II

A Study on Corrosion Behaviors of Ferritic/Martensitic Steels in Liquid Sodium Condition for Sodium-cooled Fast Reactor Application

Sang Hun Shin

This certifies that the thesis of Sang Hun Shin is approved.
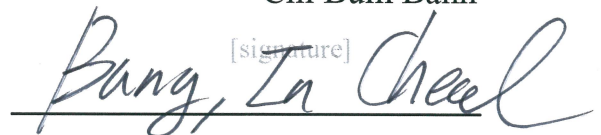
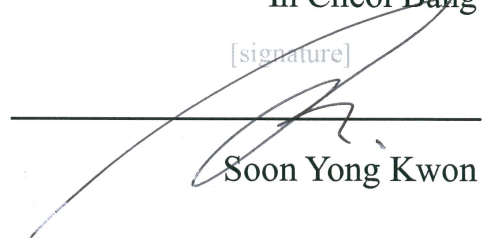01. 19. 2015

Thesis Supervisor: Ji Hyun Kim

Jun Hwan Kim

Chi Bum Bahn

In Cheol Bang

Soon Yong Kwon

ABSTRACT

Research purpose is the study on corrosion of Gr. 92 steel (ferritic/martensitic steel) with liquid sodium for advanced nuclear reactors application. Moreover, development of new measurement methods of oxygen and carbon dissolved in sodium has been carried in this study.

In this study, ASTM A182 Grade 92 steel was exposed to liquid sodium at 650℃ in order to investigate surface oxidation and corrosion behavior as well as microstructure changes, especially production of precipitates. Comparisons were made to the same material exposed to argon gas at 650℃. In sodium-exposed specimens, intergranular oxidation and chromium depletion were observed at the near surface by an electron probe micro analyzer (EPMA) used for elemental analysis. The chromium, oxygen, and sodium X-ray images overlapped, indicating $NaCrO_2$ oxidation. Since, the carbon image overlapped on $NaCrO_2$ oxide, the carbon was trapped in the oxide. The chromium image shows the chromium-depleted zone. With the argon-exposed specimen, however, this behavior at the surface was not observed. Different types of precipitates in the Gr.92 steel matrix were observed. At the interface between the Cr-depleted zone and the bulk steel matrix in specimens exposed to 650℃ liquid sodium showed mainly $M_{23}C_6$ carbide, while specimens in the bulk steel matrixes which exposed to 650℃ sodium as well as argon showed mainly a $M_2(W,Mo)$ phase. These differences may be mainly a result of oxidation ($NaCrO_2$) and chromium depletion, and presumably decarburization observed in the sodium-exposed specimens, which are different from the precipitate behavior in the case of the bulk steel matrix in sodium as well as argon-exposed specimens.

Non-metallic elements, such as carbon, oxygen, and nitrogen in sodium have a large effect on the mechanical behavior and corrosion rates of materials in the primary and secondary coolant heat transport system in sodium-cooled fast reactors (SFRs). Austenitic Fe-18%Cr-8%Ni foil and ferritic Fe foil were equilibrated at 550℃ sodium. After the equilibration, the concentration of carbon in the foils was analyzed by carbon analyzer (Leco). The carbon activity in liquid sodium was calculated. Also the thermodynamic activity of carbon in ferrite iron (Fe-C alloy) were calculated in the temperature range of 682 - 848℃. An equilibrium method using ferrite iron steel has been developed to measure the activity of carbon in liquid sodium. The results obtained are discussed and a new expression is proposed relating carbon activity with the composition of steel. The thermodynamics of carbide equilibrium in the steel are discussed by characterizing the carbide phase. These data have been analyzed using regular solution model for the carbide phase, Fe_3C and based on this observed composition of Fe_3C as well as the variation of the carbon potential of steel with temperature have been explained.

Contents

List of Figures

List of Tables

I. INTRODUCTION

1. 1 Background

In recent years, there has been a revival of research and development activities on liquid metal cooled fast reactor (LMFR) fuels and fuel cycle options. In addition to various national programmes there are international initiatives underway, including the International Project on Innovative Reactors and Fuel Cycles (INPRO), the Generation IV International Forum (GIF) and the Global Nuclear Energy Partnership (GNEP).

LMFR fuel development activities have so far been limited to a few countries, namely, the USA, France, United Kingdom, Russian Federation, Kazakhstan, Republic of Korea, Japan, India, China, and Germany. Twenty four LMFRs have been constructed and operated since the 1950s and approximately 400 reactor-years of operating experience have been accumulated. While the USA initially had a very strong fast reactor programme conducted in EBR-II and FFTF, this programme was discontinued in the late 1980s and early 1990s. A similar situation occurred in the UK where DFR and PFR were decommissioned and the fast reactor programme was discontinued. Fast reactor programmes in Germany (KNK, SNR-300) and Kazakhstan (BN-350) were also discontinued. Superphénix and Phénix in France have been decommissioned. Although the BR-10 reactor has also been decommissioned, the fast reactor programme in the Russian Federation continues to be very active in the BOR-60 and BN-600 reactors.

Fast reactors can be classified in two categories: 'first generation' reactors with relatively low coolant inlet temperatures (280–320°C) and 'second generation' reactors with inlet temperatures on the order of 360–380℃. The fast reactors designated EBR-I, DFR, BN-350 and BOR-60 are examples of the first generation category. Only six LMFRs can be considered to be currently in operation or capable of operation. These are BOR-60 and BN-600 in the Russian Federation, China Experimental Fast Reactor (CEFR) in China, JOYO and MONJU in Japan, and the fast breeder test reactor (FBTR) in India. Unfortunately both JOYO and MONJU have suffered operational accidents that have kept them from operating over the last several years. Two new fast reactors are now under construction. These are located in India (prototype fast breeder reactor, (PFBR)) and in the Russian Federation (BN-800). Figure 1-1 shows a schematic illustration of sodium-cooled fast rewacor [1].

While the various international efforts of INPRO, GIF and GNEP envision the eventual redeployment of fast reactors in Western countries, current and near term utilization will proceed primarily in the Russian Federation and Asia. Based on the extensive experience gained from proceeding and ongoing programmes, countries are focusing their efforts on improvements in safety features and fuel utilization. The latter is the primary focus of this report.

The economics of the fast reactor depend very strongly on attaining the maximum burnup of the high enriched fuel required to operate in fast reactor spectra. While there are some limitations that arise from increasing fission product accumulation, fuel restructuring and other factors, the lifetime of a fuel assembly is primarily determined by limitations associated with the structural alloys that contain the fuel and support the fuel assemblies. Some of these limitations are operational in nature, such as radiation induced deformation that impedes coolant flow, produces undesirable interaction between two components or causes unacceptable forces required to remove a component.

The most significant limitation, however, arises from failure of fuel containment that would allow release of fuel or fission products into the coolant. While such failure can arise from mechanisms associated with exposure to liquid metal coolant or from the high operating temperature, the primary cause of failures are the changes in either: physical properties, dimensions or shapes of structural alloys, which arise as a consequence of prolonged exposure to the very strenuous nuclear environment.

Structural components subject to radiation induced degradation can be divided into two major categories. First, there are long standing, largely non-replaceable structural components that surround and support the core. Second, there are the structural components that contain and support the fuel itself. These latter are exposed to the most strenuous nuclear environment and are designed to be replaceable when either the fuel has reached the target burnup or when failure is predicted to be imminent. Therefore one of the key issues in development of any advanced LMFR fuel cycle is how to develop fuel assemblies that could perform without failure to ≥ 20 at.% burnup, roughly twice the burnup currently attainable using austenitic stainless steels. High burnup can only be achieved if the performance of the structural components, including cladding and duct/wrapper materials, is satisfactory to very high exposure. Figure 1-2 shows a diagram of a representative LMFR fuel pin and fuel assembly [2]. The fuel pin usually contains mixed oxide pellets of enriched uranium and plutonium, the reference fuel for LMFRs and UO_2 blanket pellets outside the fuel zone. The two end plugs and the spiral spacer wire are the other major structural components of a fuel pin. The fuel assembly consists of a cluster of fuel pins inside a 'duct' tube which is also referred to as 'wrapper' or 'hex-can' in various national programmes. Other less critical structural components are: the handling head, core support structure and entrance nozzle of the assembly. For extended life, the cladding tubes and wrapper are the most critical components of the LMFR fuel assembly.

In addition to high temperatures (300–700℃) and sometimes high and varying stresses, the components of the subassembly will experience intensive radiation damage concurrent with liquid metal (e.g. sodium, lead) corrosion and chemical interaction with fuel and fission products, all influences accumulated over a 2–4 year residence time.
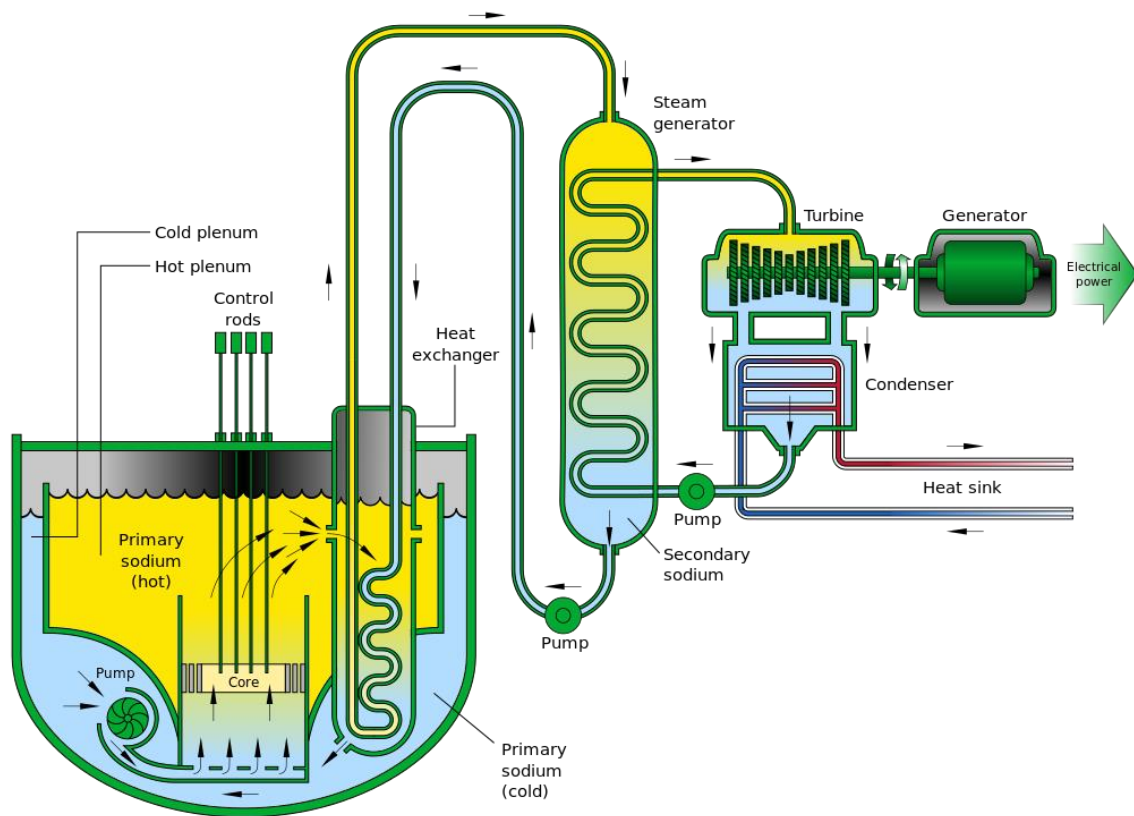
Figure 1-1. Schematic illustration of pool-type sodium-cooled fast reactor (SFR) [1].

Handling socket

Duct

Fuel rods

Nose Piece

Fuel Assembly

Upper end-plug

Wire-wrapper

Cladding

Fuel slug

Lower end-plug
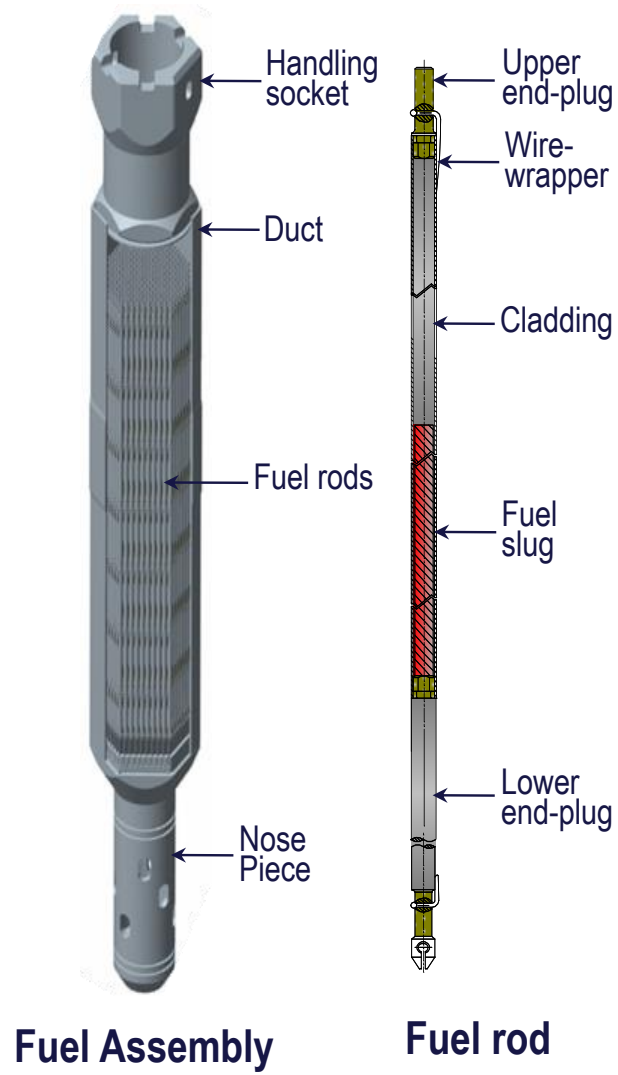
Fuel rod

Figure 1-2. Schematic illustration of the fuel assembly and fuel rod [2].

1. 2 Goal and approach

Since the cladding material in the core of sodium-cooled fast reactor is exposed a severe environment where high temperature sodium, dissolved oxygen and carbon, and fast neutrons are around the cladding. Depending on the concentration of dissolved oxygen and carbon in liquid sodium and high temperature sodium, selective dissolution of chromium from the cladding, surface, internal or intergranular oxidation, decarburization or carburization occurred at the cladding as shown in Figure 1-3.

In this thesis, the investigation at the outer surface of cladding is mainly discussed when it exposed to liquid sodium containing dissolved oxygen and carbon. Since dissolved oxygen and carbon affect corrosion behaviors and mechanical properties of the cladding, newly developed methods to measure them has been introduced in this thesis. The main goal of this thesis is to investigate the compatibility of Gr. 92 steel, one of advanced ferritic/martensitic steel, with 650℃ liquid sodium. This thesis includes three experimental sections (Chapter III, IV, and V) and one theoretical analysis section (Chapter VI) as below:

(1) Compatibility of Gr. 92 steel with liquid sodium
(2) Measurement of oxygen dissolved in liquid sodium
(3) Measurement of carbon dissolved in liquid sodium
(4) Corrosion modeling

Cladding   Coolant (Na)

Fuel pellet

F.P   F.P

n

n

Fission

Cr

Fe

2. Dissolution

n

O

1. Surface oxidation

Fission

n

n

5. Neutron absorption

F.P   F.P

3. Decarburization

C

4. Internal pressure

Original surface
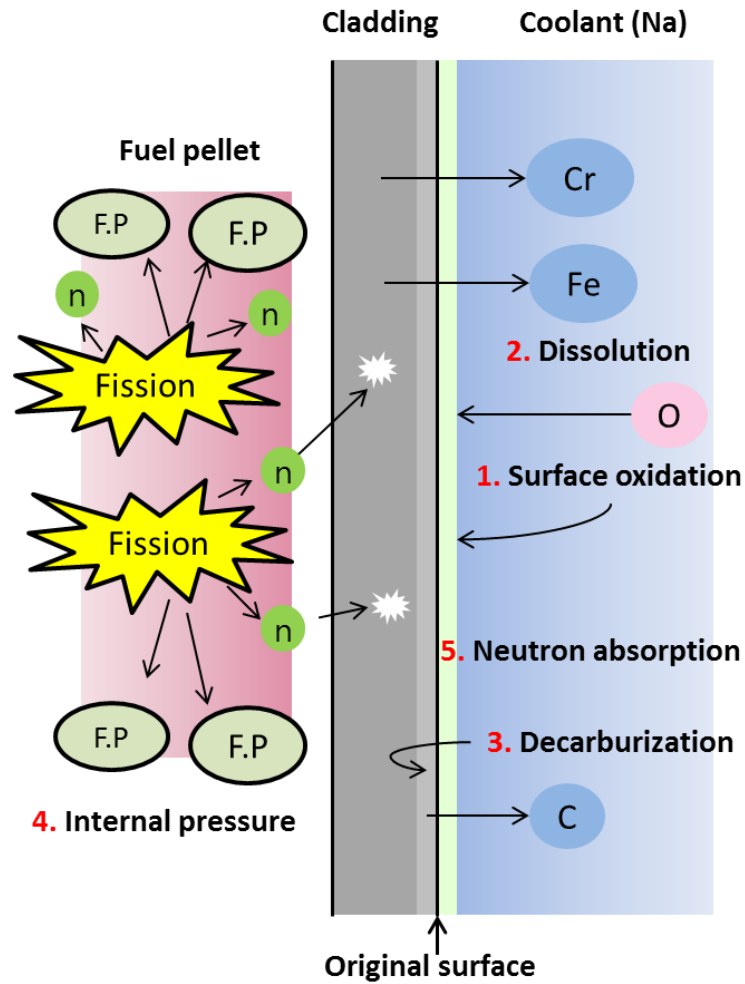
Figure 1-3. Schematic illustration of sodium-cooled fast reactor (SFR) environment around the fuel cladding.

1.3 Reference

1. http://en.wikipedia.org/wiki/Sodium-cooled_fast_reactor

2. Jun Hwan Kim, SFR Fuel Development Activities (invited seminar in UNIST, Ulsan, 2012).

II. LITERATURE REVIEW

2. 1 Development of high Cr ferritic/martensitic steels

Most of the information on ferritic/martensitic steels for nuclear applications comes from stidies on commercial Cr-Mo steels, primarily 9-12% Cr, 1-2% Mo, 0.1-0.2% C with small amounts of V, Nb, W, Ni etc. These were the ferritic steels considered first for fast breeder fission reactors in the early 1970s and then in the late 1970s for fusion applications. The steels became of interest because of their swelling resistance compared to austenitic stainless steels, which were the primary candidates for both applications up to that time [1, 2].

The development of 9-12% chromium steels is reported to have originated in 1912 with the manufacturer of a 12% Cr:2-5% Mo steel for steam turbine blades by Krupp and Mannenmann in Germany [3, 4]. In early 1910s Brearley in the U.K., while attempting to develop high-temperature steels for gun barrels, accidentally discovered that martensitic steels containing 13% Cr and 0.2% C did not rust [5]. The 9 and 12% Cr steels with lower carbon (0.1% max) contents and additions of Mo, W, V, Nb, N, and other elements, possessing higher creep-rupture strengths combined with good oxidation and corrosion resistance at elevated temperatures, have subsequently been developed. These steels have been used as considered for use in petro-chemical and chemical plants, gas turbine engineering, aircraft and aerospace industries, electrical power plants, and nuclear fission and fusion reactor components.

The 9Cr-1Mo (T9) type of steel [6], possessing fairly moderate creep-rupture strength, was initially developed in the 1930s for such petrochemical and chemical processing application. However, the procipal uses of the high-chromium martensitic steels are currently for components in gas turbines and it the boilers and turbines in steam power plants. The development and usage of the 7-12% Cr steels for core components in fast reactors and as potential first wall and breeder blanket structural materials in fusion reactor systems is reviewed in this chapter.

The development progress of newly developed higher-strength ferritic/martensitic steels is shown in Figure 2-1 [7]. It should be emphasized that there are considerable uncertainties in predicting the long-term creep-rupture strengths of the steels by extrapolation of short-term data usually obtained by testing in air.

The 12Cr (AISI 403) and wrought 9Cr-1Mo steels have been used for the pressure tube end fittings in the Canadian CANDU reactors [8] and in the evaporators and parts of the superheaters in the UK Advanced Gas-Cooled Reactors [9], respectively. The high-chromium martensitic steels have

found few other applications in thermal reactors, their main development having been directed towards fast breeder reactor usage.

Several prototype sodium-cooled fast breeder reactors have been constructed and operated as fuel element sub-assembly test facilities and also to establish the viability of commercial fast reactor core component designs under fully representative conditions without compromising the main objective of demonstrating that they could reliably generate electricity for the national grid. Thes reactors include the Dounreay Fast Reactor (DFR), RAPSODIE, PHENIX and super-PHENEX (France), KNK-2 (Germany), EBR-II and the Fast Flux Test Facility (FFTF) (USA), BN5 (10), BOR60, BN350 and BN600 (Russia), JOYO and MONJU (Japan) and FBTR (India); however, many of these reactors have now ceased operation.

The 9Cr-1Mo steel has heen utilized as internal sleeved for the rapair of leaks in the welds between the 2.25Cr-1MoNb steel steam tubes and 2.25Cr-1Mo steel tube plates in the evaporator units and also for the replacement superheater and reheater tube bundles in PFR [10]. However, the successful operation of fast reactors is also dependent on the performance of the materials used in the construction of the fuel and breeding blanket assemblies. Thus, the subassembly fuel pin cladding and wrappers (or ducts) in a commercial fast reactor have to endure prolonged service at elevated temperatures and a maximum displacement per atom (dpa) dose of 150 to 200 dpa if the fuel is to achieve an economic target burn-up of 15 to 20% of the heavy atoms.

The prototype fast breeder reactors usually commenced operation with conventional austenitic steels as the core component structural materials. However, these steels exhibited significant irradiation-induced void swelling and irradiation creep that could lead to dimensional instability and core distortion [11].

Many ferritic/martensitic steels have been employed or considered for application as wrappers (ducts) and cladding in the core fuel element subassemblies in sodium-cooled fast reactors in Europe, the USA, Russia, and Japan [12-16]. They include plain 12Cr (F1) in the U.K. and a fully ferritic, non-transformable 17Cr (F17) in France, 9Cr-1Mo (EM10) and duplex 9Cr-2Mo (EM12) in France, 12Cr-1MoV (FV607 and CRM12) in the U.K., 1.4923 in Germany and EP450 in Russia, 9Cr-1MoVNb (modified 9Cr-1Mo) in the USA and France, 12Cr-1MoVW (HT9) in the USA, and 12Cr-MovNvW (PNC-FMS) in Japan.

The heat treatments specified for the 9-12% Cr ferrtic/martensitic steels for non-nuclear conventional engineering application are aimed at maximizing the tensile proof and creep-rupture strengths. However, a high thermal creep strength has not been a primary requirement for the wrappers, as the operating temperatures are below ot at the lower end of the creep range for these mateialss and the components are not highly stressed during normal operation. A reduced creep

strength was therefore acceptable, provided that increases fracture toughness and good high-temperature ductility, coupled with adequate formability and weldability, could be acheibed. Consequently, entensive studies, involving modifications of the compositions and initial heat treatments, were carried out to develop optimum combination of properties for some of the steels intended for use as wrappers and claddings.

A major limitation of the high-chromium ferritic/martenstic steels, in common with other body-centered-cubic (bcc) steels, is that they exhibit a ductile-brittle transition temperature (DBTT) in which the energy of fracture increases with increasing temperature on passing through the transition, followed by an upper-shelf region of relatively constant or slightly decreasing high fracture energies.

Extensive data on the compability of the high-chromium martensitic steels with liquid sodium have been obtained in programs carried out in support of core component materials development for fast breeder reactors [17].

In the republic of korea, R&D activities on fuel for sodium cooled fast reactors were initiated in 2007 and focused on metallic fuel and ferritic/martensitic steel as fuel assembly structural mateials. A grade 92 alloy (9Cr-0.5Mo-1.8W-VNb) has been developed as the candidate material for fuel cladding. Experimental ingots of grade 92 alloy were prepared by vacuum induction melting, followed by hot-rolling at 200℃, normalizing at 1050℃ for one hour and tempering at 750℃ for two hours. The out of pile mechanical properties of these alloys were found to be satisfactory. Based on this experience, steel cladding tubes were manufactured by melting, hot forging, hot extrusion, cold pilgering and HT.

2.2 Compatibility of liquid sodium with materials

Evaluation of sodium environmental effects on mechanical strength is essential to assure structural integrity throughout the designed lifetime in sodium-cooled fast reactors. Fuel claddings are particularly affected by sodium, since the cladding is extremely thin and operating temperatures are very high [18]. Therefore, it is important to understand the compatibility of mateials with sodium at elevated temperatures. It is imperative that the liquid sodium coolant used has a strict control of chemistry, particularly with regard to elements responsible for liquid metal embrittlement and also of carbon and oxygen, which are primarily responsible for degradation of mechanical and corrosion properties. These effects are discussed in this section.

Austenitic stainless steels are in contact with high temperature liquid sodium in a fast reactor. In order to understand the carbon transport occurring between various regions of these materials through liquid sodium, an accurate knowledge of the carbon activity-concentration relationship in the

austenitic steels is essential. A new method involving equilibration of the steel sample with liquid sodium coupled with the measurement of carbon activity in sodium, employing an electrochemical carbon meter, is reported for the measurement of the cabon potential of the steel at different carbon concentrations in the temperature range of 860-960 K [19].

Liquid sodium, which is used as the coolant in fast reactors is quite compatible, int the pure state, with the ferritic/martensitic and austenitic steels [17]. However, traces of impurities play an important role in the corrosion, mass transport and other processes taking place in the heat transport loops of the reactor. Even parts per million levels of oxygen causes corrosion in the high temperature sections of the loop and the corrosion products get transported through the liquid sodium medium to cooler parts of the loop.

Some of the corrosion products as well as fission products which find their way into sodium oxygen impurity level, but also understand the tansport and deposition of radionuclides in the reactor. Thermochemistry of the ternary Na-M-O systems, where M stands for the components of the structural materials, figure prominently in any analysis of the corrosion of fuel cladding in flowing sodium.

In pure sodium containing low levels of oxygen (a few ppm or less), the corrosion rate is low and this proceeds by the selective leaching of alloying elements [20]. The presence of temperature gradients in the heat transport circuits enhances this process. For understanding this phenomenon, data on the solubility if the various alloying elements in sodium are required as a function of temperature. Because of their higher solubility, nickel and manganese are preferentially leached out from the steel under low oxygen conditions [21]. The loss of alloying elements make the γ-phase unstable and the depleted layer of the austenitic material transforms to ferrite [22] and chromium depleted layer of the ferritic materials. In fast flowing sodium the kinetics of selective leaching process are controlled by the diffusion of alloying elements in the steel matrix to the corroding surface.

In corrosion conditions in sodium at high temperatures, ferritic/martensitic and austenitic stainless steels show the typical mass transfer behavior caused by a temperature difference. The major alloy elements such as nickel, chromium, manganese and silicon are dissolved into sodium in the higher temperature section that induces weight loss, and these precipitates and deposit at the lower temperature section causing weight gain [17].

Under the normal operating conditions of a sodium loop, the ternalry compound that is observed is $NaCrO_2$. The threshold oxygen level above which this compound would form is an important parameter. This can be obtained by measuring the oxygen potential in Na-[Cr]-$NaCrO_2$ phase field or can deduced from the free carbides of chromium which are very stable and participate in the equilibrium leading to the formation of $NaCrO_2$ (s). The following observations are pertinent:

(1) only chromium carbide deposits are noticed in sodium loops when oxygen level is low [23];

(2) threshold oxygen levels for $NaCrO_2$ formation directly measured in sodium are higher than those computed by considering only the Na-Cr-O system.

The ternary coumpond $NaCrO_2$ is invariably formed in sodium systems constructed using one or more of the alloys such as Fe-9Cr-1Mo; Fe-2.25Cr-1Mo; AISI 304 SS, AISI 316 SSand D9 alloy. The cumulative loss of chromium from the material may be controlled by limiting the entry of oxygen into the sodium system. The leaching of chromium may also affect the equilibrium carbon potential of the sodium.

The experimental results have shown that up to a temperature of 623 K liquid sodium co-exists with Fe(s) and Na_2O(s). Oxygen potential measurements carried out in liquid sodium equilibrated with oxides of iron clearly indicated the appearance of a ternary oxide at temperature above 623 K [24]. Results of isopiestic equilibration experiments and solid state equilibrations have shown that Na_4FeO_3 coexists with metallic iron and liquid sodium at 923 K. Differential thermal analyses of liquid sodium samples equilibrated with iron oxides showed a reversible transition at 760 K.

Similar observations were made by Charles et al. during their studies in Na-Fe-O system [25]. This is attributed to the appearance of another ternary oxide phases in liquid sodium [26] and similar conclusions were made by Bhat et al. based on their oxygen potential measurements in sodium using a solid electrolyte technique [27]. With a view to identifying the nature of reactions leading to the formation of ternary oxides, differential scanning calorimetric measurements with varying ratios of oxides of iron and sodium as well as mixtures of Na_4FeO_3 and sodium were carried out. These results coupled with identifications of the products of solid-state reactions between Na_2O(s) and FeO(s) have shown that the reversible transition occurring at 760 K is the appearance of a liquid phase of Na_4FeO_3-Na_4FeO_3 co-exists with metallic iron and sodium above 623 K.

2.3 Sodium corrosion

Sodium is one of the elements that exhibit the characteristics demanded of coolants for fast breeder reactors (FBRs). The physical properties of sodium are shown in Table 2-1 with other coolants.

There are two known mechanisms of sodium corrosion. One is corrosion produced by the dissolution of alloy constituents to sodium, and the other is corrosion produced through chemical reaction with the impurities in sodium.

In case of corrosion produced by the dissolution of alloy constituents to sodium, corrosion is dependent on the solubility in sodium of the elemental composition in the material, temperature, and the rate of solution.

The solution rate R_c is given by the following formula:

$$R_c = K(C_s - C_i) \tag{2-1}$$

where K is the solution rate constant, C_s is the solubility limit in sodium, and C_i is the actual concentration in sodium. The solution rate constant K is contolled by diffusion. The solubility of the alloy elements of the steel is shown in Figure 2-2 [28-31]. The solubility of each of the elements in sodium at 823 K is less than a few parts per million. This means that the compatibility of the steels with sodium fundamentaly excellent.

In the isothermal sodium condition, the corrosion of the steels stops when the dissolved elements reach saturation concentration at the temperature of sodium. However, in the non-isothermal sodium condition, corrosion resulting from the difference in activity between sodium and the material aurface occurs continually. This corrosion behavior is called thermal gradient mass trnafer. In the cooling system, the elements in the materials in the high-temperature section dissolve as a result of the temperature dependency of the solubility of the elements in sodium, and the dissolved elements are deposited on the steel surface in the low-temperature section by the same mechanism.

Generally, selective corrosion occurs at the initial stage as a result of the dissolution of the elements in the steel, and then the behavior moves to general corrosion with the progress of time.

The most important elemet in the impurities in sodium is oxygen. Sodium is the reducing agent, and its affinity to oxygen is very strong. The solubility of oxygen in sodium is significantly higher than in water. However, the control of impurities in sodium can be achieved by using the cold trap technique [32] based on the theory of the deposit of dissolved impurities in sodium.

The introduction of oxygen into sodium may occur during nuclear plant construction, refueling, the supplementing of the reactor cover gas, the opening of the coolant boundary for maintenance operations, etc. These are the paths for contamination through oxides adhering to the components and the impurities in the gas.

In addition to oxygen, impurities in sodium include elements in the steel, hydrogen, and nitrogen. Hydrogen and nitrogen induce changed in the microstructure that lead to the potential degradation of mechanical properties.

Temperature dependency of the corrosion rate is the sodium of austenitic stainless steels is shown in Figure 2-3. In fact, it is understood that the corrosion of stainless steel is dominated by the dissolution process of the major elements (iron, chromium, and nickel) of the steel.

The dissolved oxygen in sodium influences the dissolution reaction. The effect of dissolved oxygen on the corrosion rate is described by the following formular because the corrosion process is dominated by the reaction process of oxide.

$$C_R \propto [O_2]^n \tag{2-2}$$

where C_R is the corrosion rate, $[O_2]$ is the oxygen concentration, and n is a constant. The constant, n, is reported by the researchers, is listed in Table 2-2. This result suggests the possibility that the control of dissolved oxygen may significantly influence the corrosion behavior.

In monometallic sodium loops, the difference of the carbon activity, which is the driving force of the carbon transfer of the material, increases as temperature increases. Therefore, decarburization occurs in the high-temperatures section and carburization occurs in the low-temperature section. On the other hand, in bimetallic sodium loops which consist of austenitic stainless steel and ferritic steel, it is easy for decarburization to occur in the ferritic steel, which has a high carbon activity due to the difference in carbon activity between different materials, whereas carburization in austenitic stainless steel, which has low carbon activity, easily occurs at elevated temperature.

Carbon is an important element in maintaining the superior mechanical strength of steel. Therefore, the carburizing/decarburizing behavior of the steels via sodium is important from the perspective of mechanical properties. Figure 2-4 shows the boundary between carburization and decarburization in monometallic sodium loops consisting of austenitic stainless steel (single alloy) [39]. At a carbon concentration of 0.2 ppm in sodium, the temperature boundary is 650℃, with decarburization occurring over that temperature and carburization occurring below that temperature. Although the boundary is influenced by the carbon concentration in sodium (carbon activity), it is necessary to take decarburization and carburization into consideration to apply austenitic stainless steel when the temperature is above 550℃, such as fuel cladding tube.

On the other hand, in bimetallic sodium loops that consist of ferritic steel and austenitic stainless steel (two alloys), decarburization and carburization also occur in the temperature range of the structural materials <550℃.
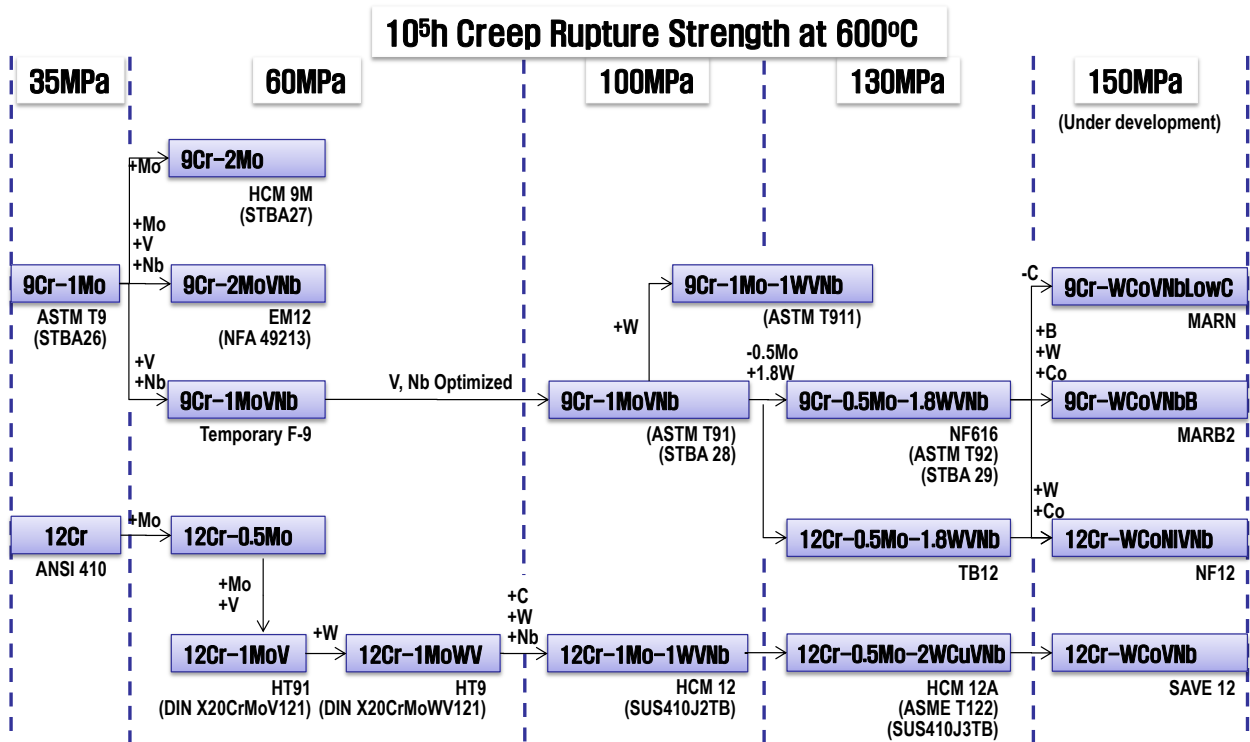
Figure 2-1. Development progress of ferritic/martensitic steels (FMS) containing 9-12%Cr [7].

Table 2-1. Comparisons of coolant for liquid metal fast reactor system

	Na	Pb	LBE
Atomic weight	**22.997**	207.21	208
Number of collisions needed to thermalize	**172**	1507	-
Melting point (˚C)	**97.72**	327.46	123.5
Boiling point (˚C)	**883**	1749	1670
Specific heat (J/kg-K)	**1300**	140	150
Density (kg/m^3)	**927**	11340	10474
Thermal conductivity (W/m-K)	**140**	35	7.98
Absorption cross section (Σ_a)	**0.01347**	0.005603	0.003034
Coefficient of linear thermal expansion (10^{-6}/K)	**71**	28.9	-

Table 2-2. Comparison of oxidation coefficient on corrosion rate [32, 34, 35, 39, 40]

Bibliography	**O_2 content (ppm)**	**Coefficient (n)**	**Reference**
Thorley	5-100	1.5	[32]
Zebroski	12, 50	1, 1.56	[34]
Roy	5-30	1.2	[40]
Kolster	1-8	0.91	[35]
	8-40	>1	
Maruyama	2.5-9	0.8	[39]
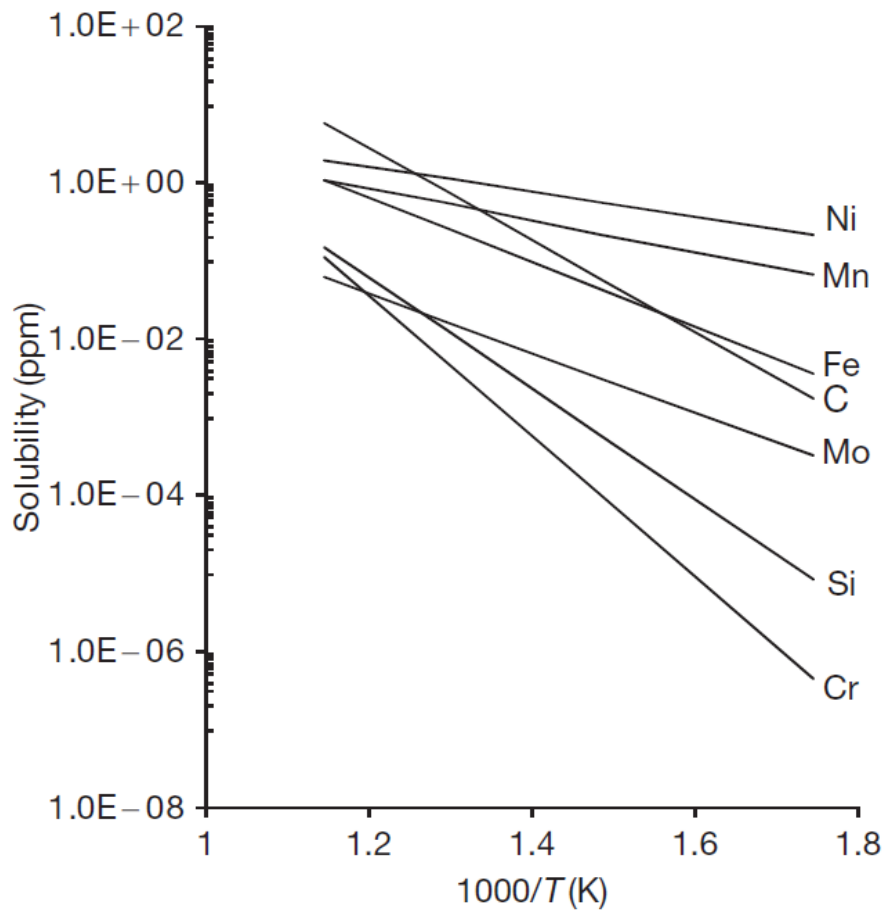
Figure 2-2. Solubility of alloy constituents in sodium [28-31].
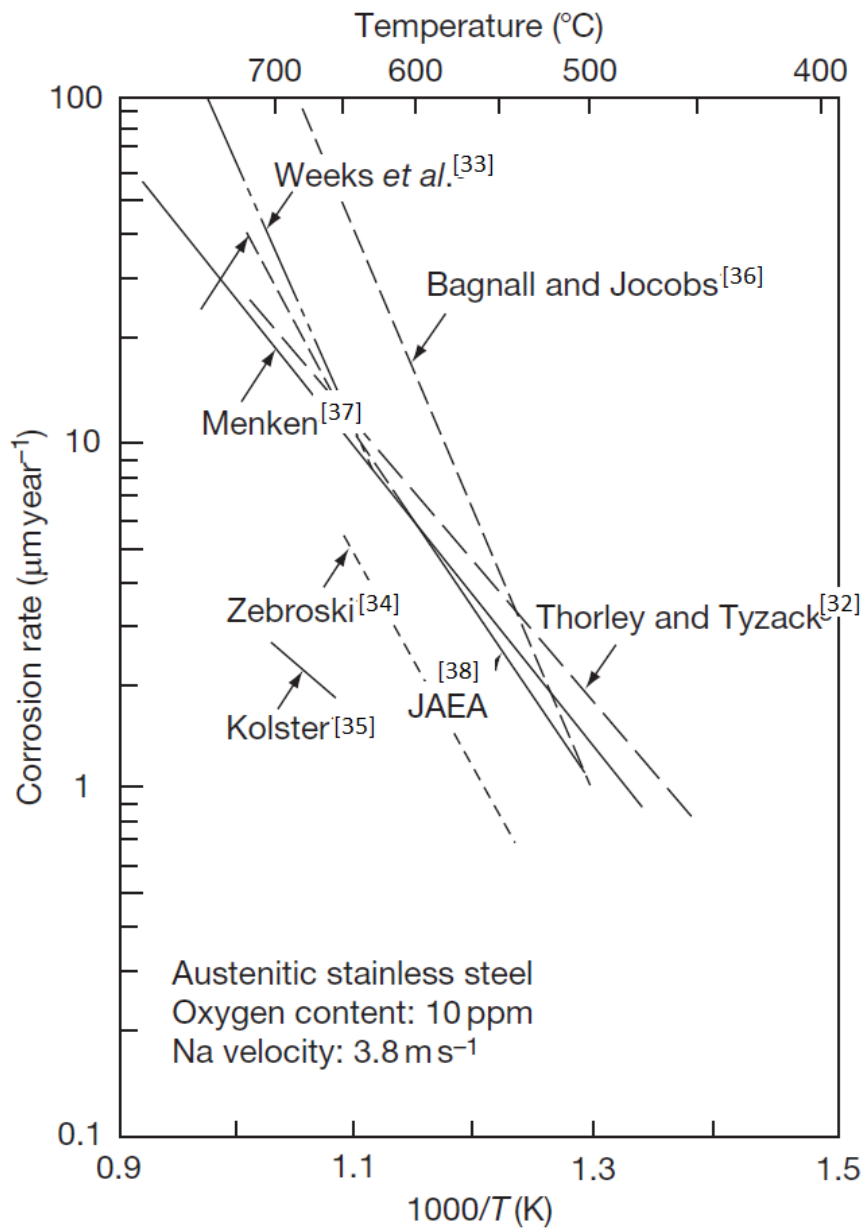
Figure 2-3. Corrosion rate of austenitic stainless steels in flowing sodium [32-38].
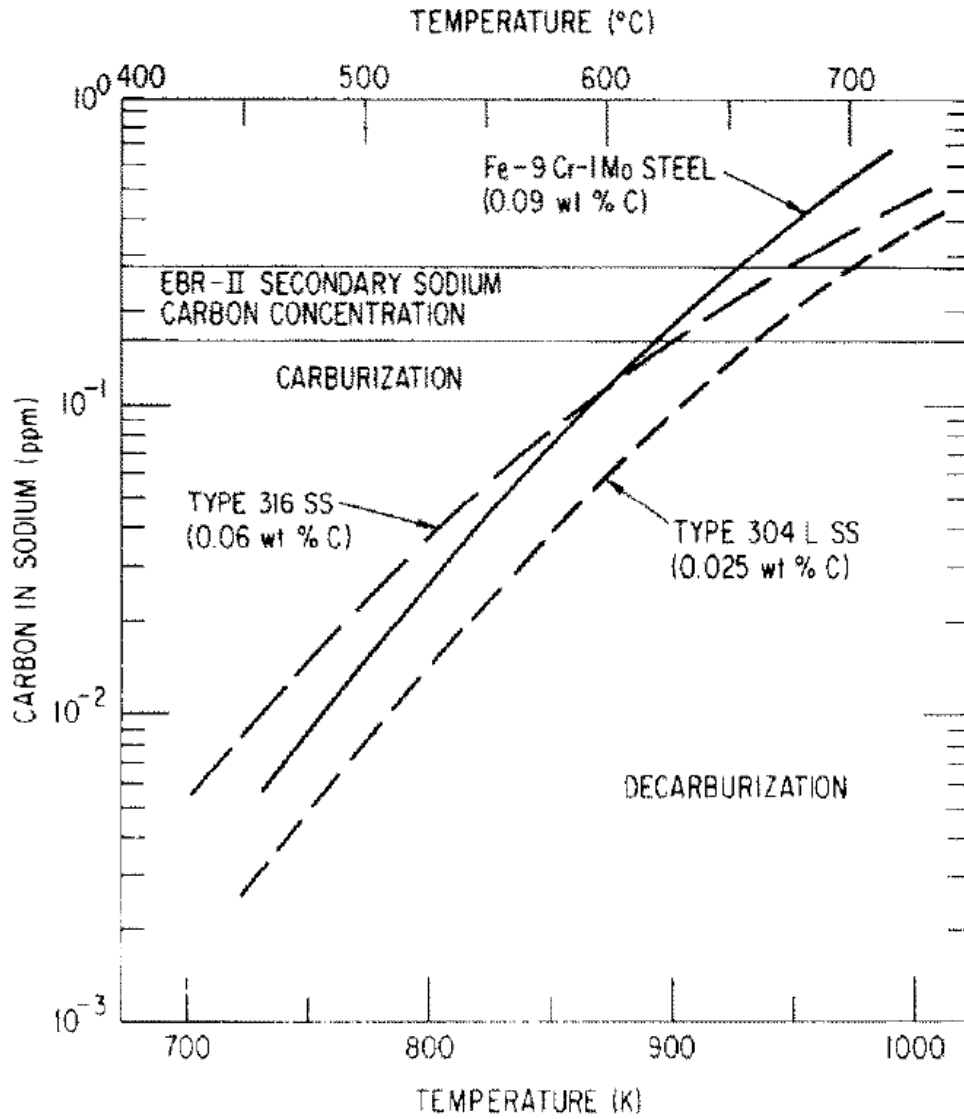
Figure 2-4. Carburization/decarburization regimes for Fe-9Cr-1Mo steel and AISI 316 and 304L stainless steels relative to the carbon concentration in sodium and temperature [39].

2.4 Reference

1. S. N. Rosenwasser, P. Miller, J.A. Dalessandro, J.M. Rawls, W.E. Toffolo, W. Chen, J. Nucl. Mater., 85-86 (1979) 177.

2. D.R. Harries, in: Proceedings of Topical Conference on Ferritic Steels for Use in Nuclear Energy Technologies, Eds. J.W. Davis and D.J. Michel (The Metallurgical Society of AIME, Warren-dale PA, 1984) 141.

3. Z. Briggs and T.D. Parker, The Super 12% Cr Steels (Climax Molybdenum Co., New York, 1965).

4. Anon, Super 12% Cr Steels-An Update (Climax Molybdenum Co., New York, 1983).

5. H. Brearly, Knotted String-Autobiography of a Steelmaker (Longmans, London, 1941).

6. L. Egnell, in: High Temperature Steels and Alloys for Gas Turbines (The iron and Steel Inst., London, Special Report No. 43, 1952) 46.

7. F. Masuyama, in: Advanced Heat Resistant Steels for Power Generation, Eds. R. Viswanathan and J. Nutting (The Inst. of Materials, London, Book 708, 1999) 33.

8. R.R. Hosbons, in: Topical Conference on Ferritic Alloys for Use in Nuclear Energy Technologies, Eds. J.W. Davis and D.J. Michel (Met. Soc. AIME, Warrendale, PA, 1984) 91.

9. T. Orr and S.J. Sanderson, in: Topical Conference on Ferritic Alloys for Use in Nuclear Energy Technologies, Eds. J.W. Davis and D.J. Michel (Met. Soc. AIME, Warrendale, PA, 1984) 261.

10. F. S. Dickinson, A.F. Taylor, P.W. Jackson, R.W. Smith, in: Topical Conference on Ferritic Alloys for Use in Nuclear Energy Technologies, Eds. J.W. Davis and D.J. Michel (Met. Soc. AIME, Warrendale, PA, 1984) 269.

11. J.F.W. Bishop, in: Dimensional Stability and Mechanical Behavior of Irradiated Metals and Alloys, Vol. 2 (British Nuclear Energy Society, London, 1984) 115.

12. C. Brown, R.J. Lilley, G.C. Crittenden, Nucl. Engineer, 35 (1994) 122.

13. A.J. Lovell, A.L. Fox, W.H. Sutherland, S.L. Hecht, in: Reliable Fuels for Liquid Metal Reactors (American Nuclear Society, LeGrange Park, IL, 1987) 3-25.

14. D.S. Gelles, in: EUROMAT 96: Materials and Nuclear Power, (The Inst. of Materials, London,

1996) 281.

15. K. Ehrlich, G. Muhling, in: Reliable Fuels for Liquid Metal Reactors (American Nuclear Society, 1987) 41.

16. E.A. Little, D.R. Harries, F.B. Pickering, S.R. Keown, Metals Tech. 4 (1977) 205.

17. H.U. Borgstedt and C.K. Mattewsm, Applied Chemistry of the Alkali Metals (Plenum Press, London, 1987)

18. Y. Kani, Y. Sagayama, in: Proceedings of a Symposium: Energy and the Environment – The Role of Nuclear Power, Eds. J.C. Lee (DEStech Publications, University of Michigan, 2002) 139.

19. S.R. Pillai, C.K. Mathews, J. Nucl. Mater. 150 (1987) 31.

20. A.W. Thorley, in: 3rd Int. Conference on Liquid Metal Engineering and Technology (BNES, Oxford, Vol. 3, 1984) 31.

21. C.W. Mathews, Pure & Appl. Chem., 67 (1995) 1011.

22. H.U. Borgstedt, Rev. Coating and Corros. 2 (1977) 121.

23. B.W. Kolster, J. Nucl. Mater. 55 (1975) 155.

24. R. Sridharan, K. Krishnanmurthy, C.K. Mathews, J. Nucl. Mater. 167 (1989) 265.

25. R.G. Charles, Trans. Am. Nucl. Soc. 19 (1974) 107.

26. R. Sridharan, T. Gnanasekaran, C.K. Mathews, J. Alloys and Comp. 191 (1973) 9.

27. N.P. Bhat, H.U. Borgstedt, J. Nucl. Mater. 158 (1988) 7.

28. W.P. Stanaway, R. Thompson, in: proceedings of the 2nd Int. Conf. on Liquid Metal Engineering and Technology (Harwell, Oxford, 1980) 1584.

29. T.D. Claar, Reactor Technol. 13 (1970) 124.

30. W.P. Stanaway, R, Thompson, Liquid Metal Systems (Plenun Press, New York, 1982) 421.

31. K. Lizawa, Nucl. Eng. 33 (1987) 62.

32. A.W. Thorley, in: 3rd Int. Conference on Liquid Metal Engineering and Technology (BNES, Oxford, Vol. 3, 1984) 31.

33. J.R. Weeks, C.J. Klamut, D.H. Gurinsky, Alkali Metal Coolants (H M Stationery Office, London, 1967) 3.

34. E.L. Zebroski, Liquid Alkali Metals (BNES, London, 1973) 195.

35. R.H. Kolster, in: Proceedings of the Int. Conf. on Liquid Metal Technology in Energy production (Champion, PA 1976) 368.

36. C. Bagnall, D.C. Jocobs, WARD-NA-3045-23 (1975)

37. G. Menken, in: Proceedings of 2nd Int. Conf. on Liquid Metal Technology in Energy Production (Richland, WA, 1980)

38. T. Furukawa, S. Kato, E. Yoshida, J. Nucl. Mater. 392 (2009) 249.

39. O.K. Chopra, K. Natesan, T.F. Kassner, J. Nucl. Mater. 96 (1981) 269.

III. COMPATIBILITY TEST OF GR. 92 WITH LIQUID SODIUM

3. 1 Introduction

Ferritic-martensitic steels (FMS), which contain 9-12% of chromium, are being considered as attractive candidate materials for fuel cladding in fast reactors due to their higher thermal conductivities, lower expansion coefficients, and better resistance to irradiation-induced void swelling in comparison to austenitic stainless steels [1-5]. When these steels are used as fuel cladding in sodium-cooled fast reactors, their peak temperatures are expected to approach 650℃, depending on design factors. In this situation, gaseous fission products become a source of internal stress on the cladding [6]. The cladding should thus have better mechanical properties such as a good tensile strength and creep resistance at high temperatures.

Fuel cladding, a seamless tube approximately 7mm in diameter, 0.6 mm in thickness, and 3 m in length, depending on reactor design, is the component containing the fuel materials and preventing radioactive species produced by fission from being released. Mechanical behavior such as tensile strain and creep of the cladding are easily affected by small changes of the material characteristics, including alloy chemical composition, grain structure, and precipitates. To ensure the integrity of the fuel cladding tube, it is necessary to observe changes in the cladding properties, such as microstructure and mechanical characteristics, when exposed to liquid sodium environment. Previous studies regarding compatibility between fuel cladding material and liquid sodium have mainly focused on the mechanical properties [7-9] and corrosion [10-12] of austenitic steel.

Gr. 92 steel (9Cr-0.5Mo-1.8W-VNb) is one of the advanced versions of chromium steels that was developed in the early 1990s. It has higher creep-rupture strength than its predecessors, 9Cr-1Mo steel and Gr. 91 steel (9Cr-1Mo-VNb) [13-15], and thus it is known to be used at 620℃ [16] making it for high temperature applications in advanced reactors. Gr. 92 steel has tempered martensitic lath structure with precipitates such as $M_{23}C_6$ (where M is mostly Cr) and MX (M: Nb or V; X: C and N) [17-20] after normalizing and tempering heat treatment process.

The mechanical properties of FMS are mainly determined by factors including the alloying elements, prior-austenite grain size, subgrain size, lath width, dislocation density, and precipitates. Various mechanisms such as coarsening of precipitates, generation of subgrains, and softening of the lath structure take place during aging, and the mechanical strength of the material decreases [21]. Corrosion related issues such as liquid metal embrittlement, dissolution of constituents and chemical reaction of FMS with impurities (such as dissolved oxygen) in liquid sodium environment was also

discussed [12, 22-26]. At present, research regarding how liquid sodium affects the precipitate amount, type, size, morphology, stability, and distribution is scarce for cladding tubes.

The objective of this study is to investigate the near surface behavior of Gr. 92 steel when exposed to liquid sodium, especially microstructural changes in the steel such as oxidation, decarburization, and chromium depletion which affect the microstructural evolution of the Gr. 92 steel.

3. 2 Experimental

The test material in this study is ASTM A182 Gr.92 steel, which contains approximately 9 wt% of chromium and 2 wt% of tungsten. Chemical composition of this material is shown in Table 3-1. Gr.92 tubes were manufactured by hot extrusion and multiple passes of cold drawing. Subsequently, the tubes were normalized at 1080℃ for 6 min and tempered at 800℃ for 6 min so as to develop a tempered martensite structure [27].

A liquid-sodium material-compatibility facility was manufactured and is shown in Figure 3-1 (a) and (b); liquid sodium flows under natural circulation, driven by thermal convection. The facility is containing a sodium storage tank, a compatibility test loop, a sodium expansion tank, an electromagnetic flow meter, and a glove box. The test loop is made of 316L stainless steel and heated by seven independent heater systems. 1.5 liter of sodium can be filled in the vacancy loop and the temperature of sodium is independently controlled at each zone with immersed k-type thermocouples. The velocity of sodium is between 0.17 m/s and 0.25 m/s, when difference in sodium temperatures at the hot side and cold side is between 50℃ and 100℃, respectively. Details of the facility have been published elsewhere [28]. Gr. 92 cladding tubes were exposed to 650℃ liquid sodium for up to 3095 h. For the first 1512 h of test time, the oxygen-content in sodium was measured as 20 ppm using a vanadium wire equivalent technique; following that, additional tube was inserted and sodium exposure continued for another 1583 h. While insertion of the second cladding, some leaks inadvertently happened so that the dissolved oxygen level at that time reached the saturated level. The exposure schedule is shown in Figure 3-1(c). As control comparisons for the sodium effect, other Gr. 92 cladding tubes were encapsulated in 99.999% purity of an argon environment and kept in a 650℃ muffle furnace for 1601 h and 2973 h.

After exposure to a sodium or argon environment, specimen cross-sections were polished with 0.04 μm alumina particles. Cross-section images were taken using a scanning electron microscope (SEM), and an energy-dispersive of electron-probe microanalysis (EMPA) used for qualitative analysis of light elements such as Na, C, and O at the specimen surfaces.

(a)

3 7

(b)

(c)
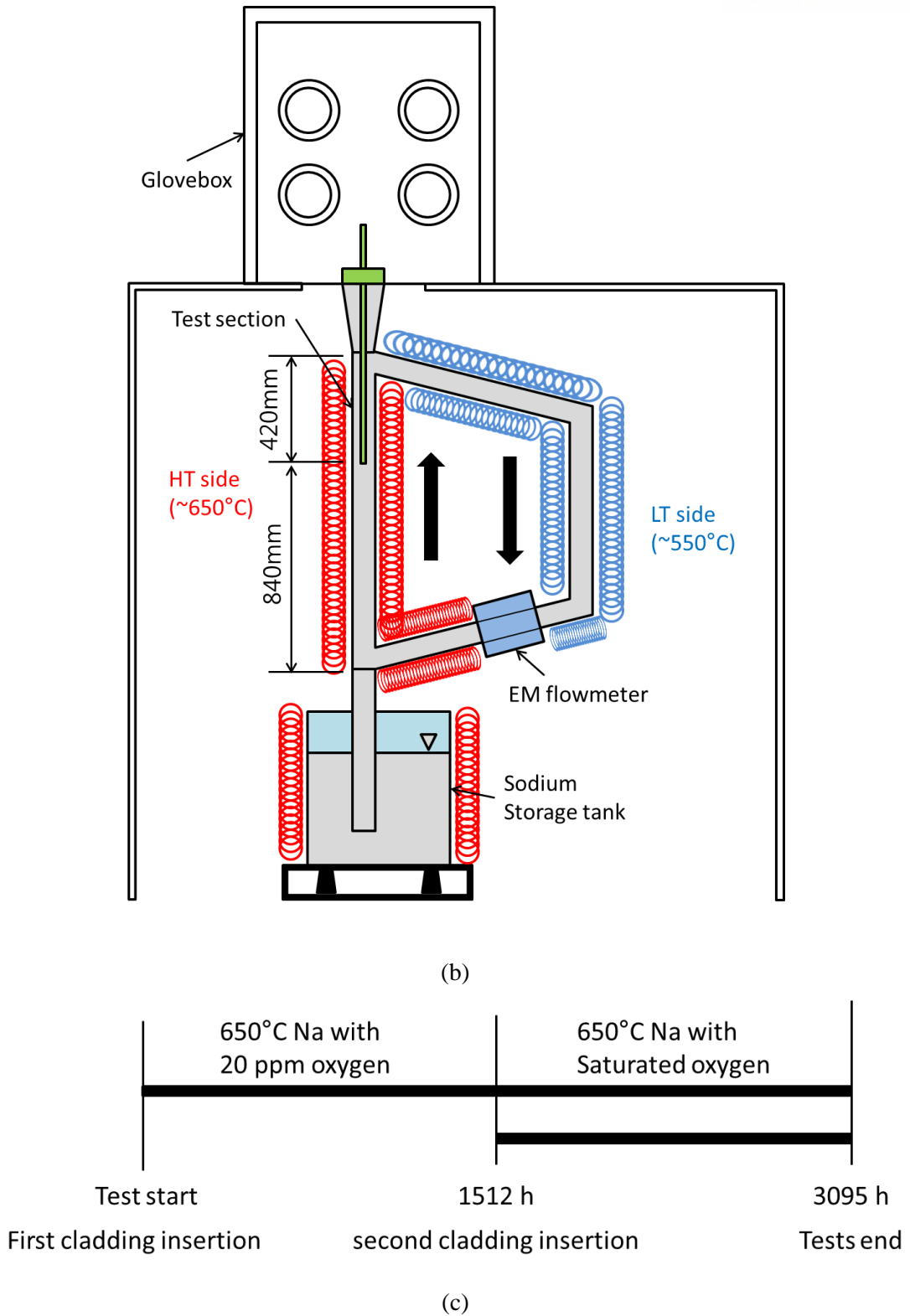
Figure 3-1. Image of (a) the sodium-material compatibility facility at KAERI (korean atomic energy research institute), (b) its schematic illustration and (c) the experimental conditions.
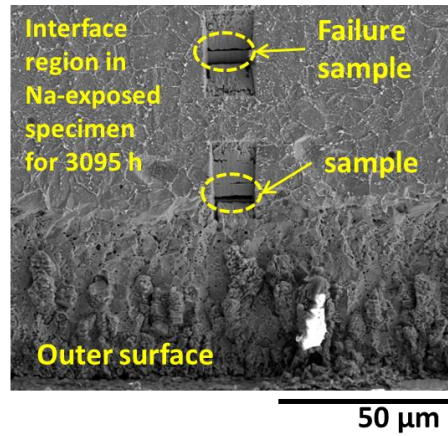
(a)
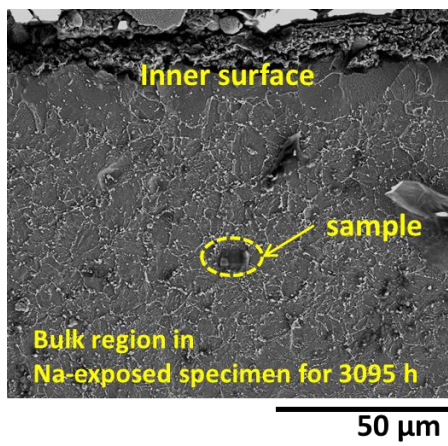
(b)
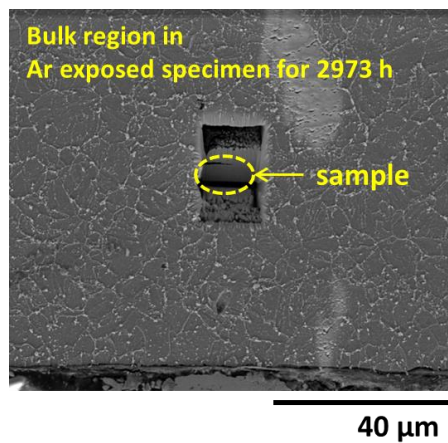
(c)

Figure 3-2. Position of the FIB samples prepared from (a) interface region in sodium-exposed specimen after 3095 h at 650°C, (b) bulk region in the same specimen of (a), and (c) argon-exposed specimen after 2973 h at 650°C.

The positions on the cross-sections of samples prepared by focused ion beam (FIB) are shown in Figure 3-2. Two FIB samples were cut from the sodium-exposed specimen for 3095 h at the interface between bulk steel and the chromium-depleted zone as shown in Figure 3-2 (a) and at the bulk steel near outer surface of the sample as shown in Figure 3-2 (b). In Figure 3-2 (a), there are two positions for FIB sample preparation, however, above one was failure during the preparation and not used in this study. Another FIB sample was also cut from the in an argon-exposed specimen at bulk steel as shown in Figure 3-2 (c).

The carbon-extracted replica was prepared at the polished steel surface, which represented the bulk side at the interface between bulk steel and the chromium-depleted zone. In detail: FIB samples were prepared using a Quanta 3D FEG dual beam focused ion beam (FIB); carbon extraction replicas were prepared by mechanical polishing at the depth of the chromium depleted region, etching with a mixed acid solution (93 vol.% water, 5 vol.% nitric acid and 2 vol.% fluoric acid), carbon coating, and removing the replicas by electrochemical etching with a second mixed solution (90 vol.% methanol and 10 vol.% hydrochloric acid).

The precipitates in both sample preparation methods were examined using a JEM-2100F high resolution transmission electron microscope (HR-TEM) with an energy dispersive spectroscope (EDS). Size distribution of precipitates was measured with an image analyzer.

3. 3 Results and Discussion

Secondary electron SEM images of specimens after liquid sodium and argon exposure at 650℃ are shown in Figure 3-3. Figure 3-3 (a) and (b) show the cross-sections of specimens after exposure to 650℃ sodium for 1583 h and 3095 h, respectively. Not only a precipitation-free zone but also islands of a newly formed phase under the surface of specimens were observed in both specimens. Figure 3-3 (c) and (d) show cross-sections of specimens after exposure to a 650℃ argon environment for 1601 h and 2973 h, respectively. The precipitation-free zone and the islands were not observed in either specimen.

To investigate the near-surface zone in specimens that were exposed to liquid sodium, EPMA X-ray mapping was also used. In Figure 3-4 and Figure 3-5, the backscattered electron images (BSE) show two zones in the specimens (excluding the left margin, which is mounting resin containing O and C). First, the dark islands in the steel matrix represent $NaCrO_2$ from Na, Cr, and O peaks. Second, there is a chromium depletion zone. In the image from the Cr X-ray peak, Cr was depleted by the liquid Na or was diffused to form the oxides.

Table 3-1. Chemical composition of Gr.92 specimen (in wt%).

	C	Si	Mn	Cr	Ni	Mo	W	V	Nb	Cu	N	B	P	S
Gr.92	0.087	0.21	0.41	8.69	0.13	0.38	1.62	0.18	0.07	0.10	0.046	0.0022	0.012	0.0018

(a)

(b)

4 2
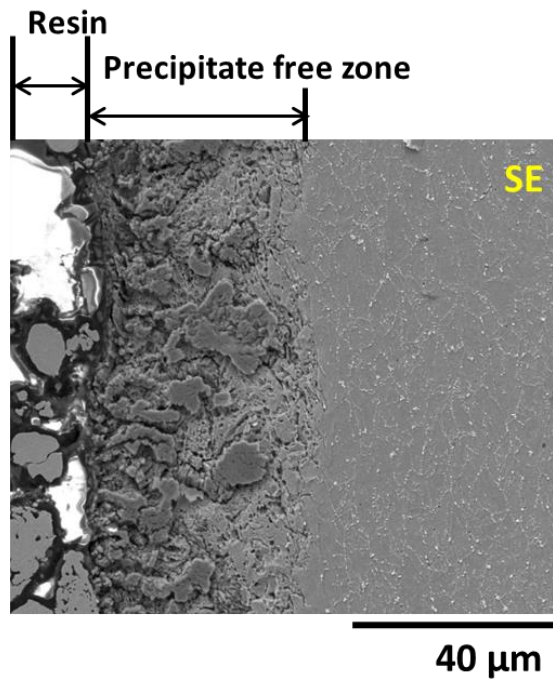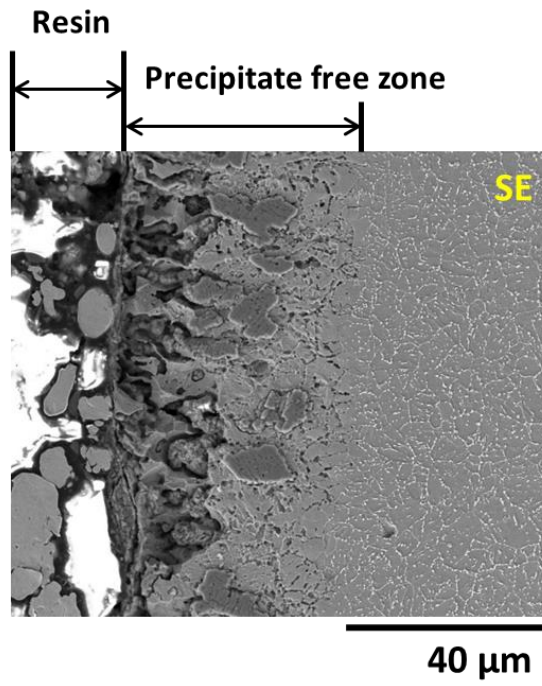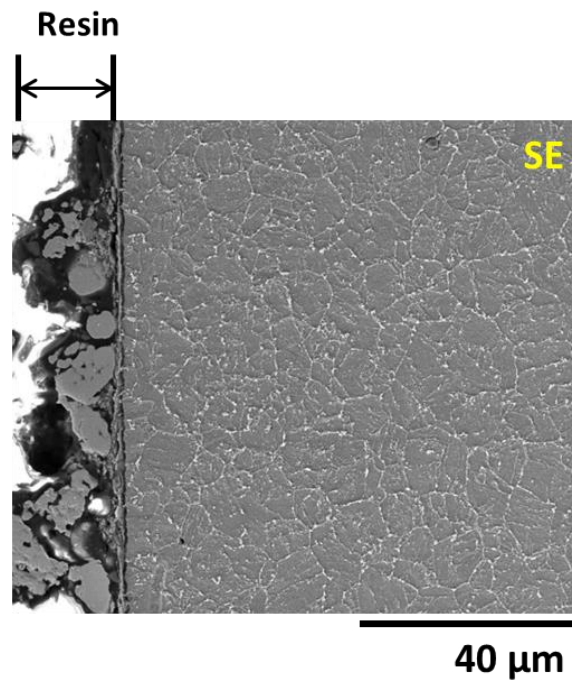
(c)
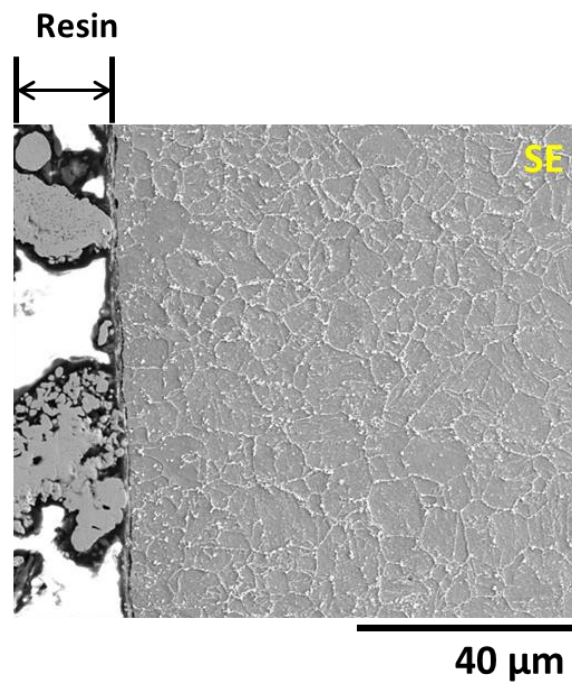
(d)

Figure 3-3. SEM images of cross-sections of specimens after exposure to (a) 650°C sodium for 1583 h, (b) 650°C sodium for 3095 h, (c) 650°C Ar gas for 1601 h, and (d) 650°C Ar gas for 2973 h.
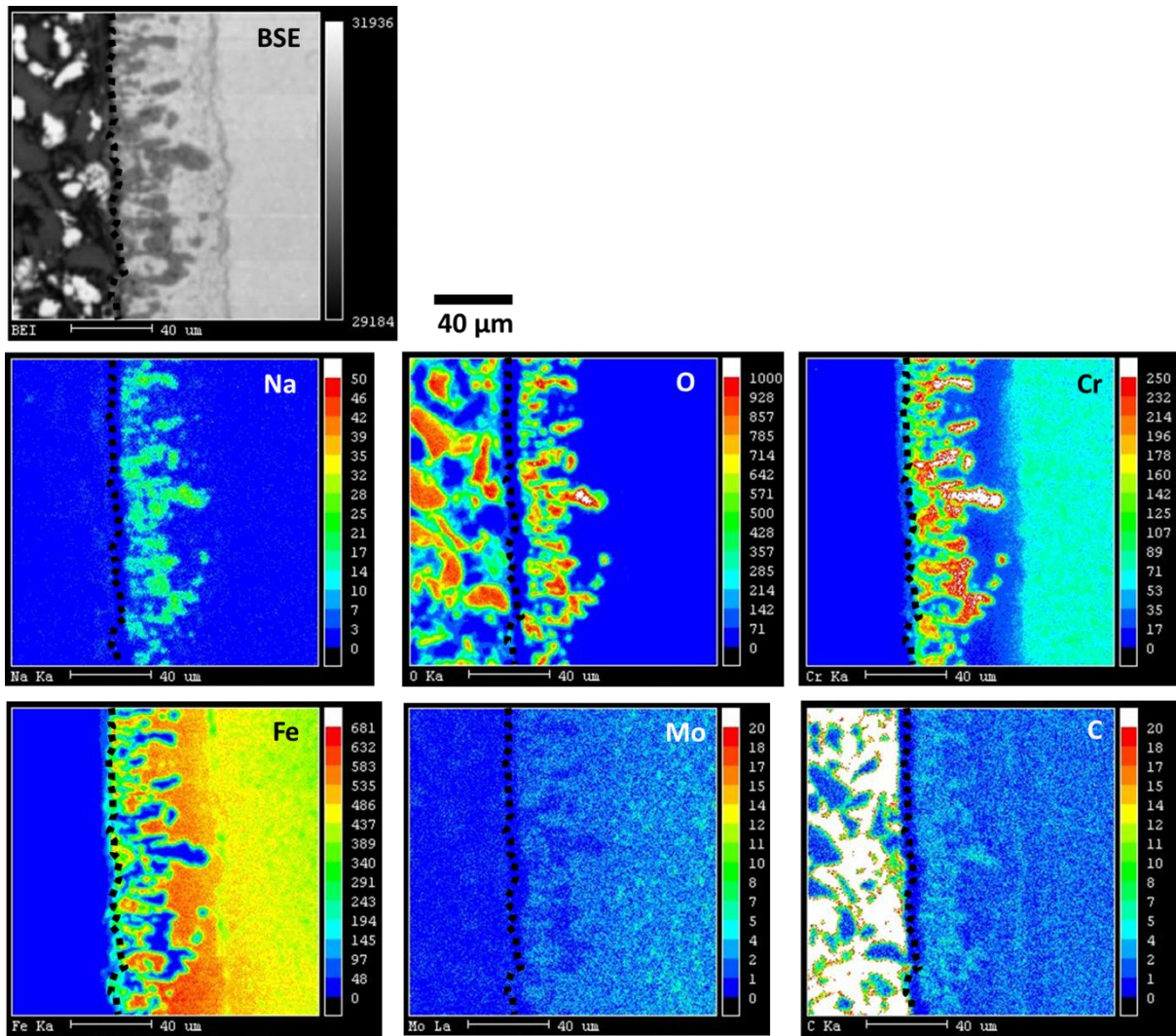
Figure 3-4. EPMA X-ray mapping of Gr. 92 specimen which was exposed to Na for 1583 h at 650 °C.
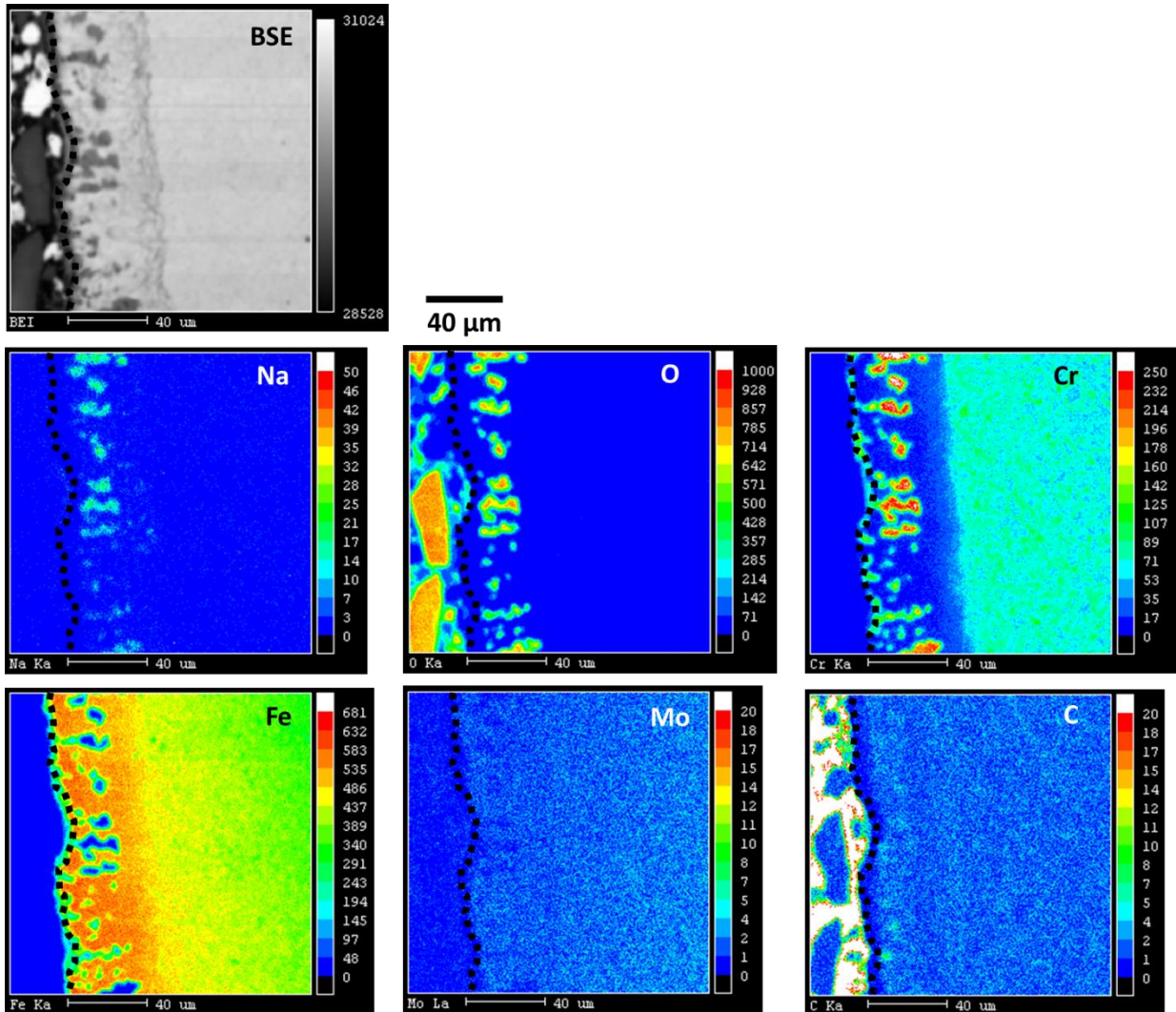
Figure 3-5. EPMA X-ray mapping of Gr. 92 specimen which was exposed to Na for 3095 h at 650 °C.

The apparently Na, O, and C free zones beneath the dotted lines should probably indicate the steel surface. The C overlaps with the Cr, O, and Na images. This may indicate there is sufficient Cr in the oxide to form carbide, since Cr is a strong carbide former. Mo and Fe were not used to form an oxide in this study and the Mo peak was overlapped with Fe peak.

Due to oxygen saturation in the sodium after 1512 h (see Figure 3-1. (c)), sodium chromite (NaCrO$_2$) was formed under the surface of the specimens, as seen in Figure 3-4 and Figure 3-5. FMS appear sensitive to the increase of the oxygen concentration. At 20-30 wppm of dissolved oxygen in sodium, NaCrO$_2$ layer formed at the surface of the steels and internal oxidation of the steels occurs. For higher oxygen concentration ($<$ 30 wppm), intergranular corrosion can occur with possible grain removal [22].This type of oxide was also observed on T91, 15-15Ti and 316L(N) steel in a 550℃ sodium environment with 1-10 wppm of controlled oxygen [29, 30]. In a recent study, after 48 h of exposure in 450℃ liquid sodium with low oxygen concentration, a 0.2 μm thickness NaCrO$_2$ on the surface of a T91 specimen was observed, and with longer exposure time, one observed the formation of a thicker NaCrO$_2$ oxide on the surface [31]. This points out that intergranular oxidation occurred on the Gr. 92 specimens in oxygen saturated sodium at 650℃ as shown in Figure 3-4 and Figure 3-5.

It is assumed that the interface between bulk steel and the intergranular oxide operated as a carbon sink, not allowing carbon to escape through an intergranular oxide. Assuming that carbon solubility in NaCrO$_2$ is negligible, as with Cr$_2$O$_3$ [32], solid-state diffusion of carbon through the oxide is not a possible mechanism. So the EPMA image from the carbon X-ray peak in Figure 3-4 and Figure 3-5 is seen to overlap with the oxide image (Na, Cr, and O X-ray peaks). Such a decarburization process can originate from the difference in dissolved carbon levels between the specimen material and the liquid sodium, which is governed mainly by the dissolved carbon content of the loop piping material [33]. While the maximum carbon content inside the liquid sodium is assumed to be 0.02 wt% (since the carbon content of the piping material was 0.02 wt%), the carbon content of the material (0.087 wt% in Gr. 92) was higher than the sodium, acting as a driving force for dissolved carbon at the specimen surface to diffuse into the liquid sodium. Such a decarburization process results from not only the difference in carbon content, but also the temperature of the test section, 650℃, which is higher than the cold section by 550℃ to increase the local carbon content of the liquid sodium [27].

Figure 3-6 shows a schematic illustration of the specimen's surface change after exposure to liquid sodium containing dissolved oxygen. At the surface, integranular oxidation, Cr-depletion, and decarburization occur. The Cr depletion behavior is complex: Cr is used to form the oxide and some diffuses into the bulk liquid Na. Material near the surface is affected by liquid Na and bulk steel is affected by the high temperature environment.
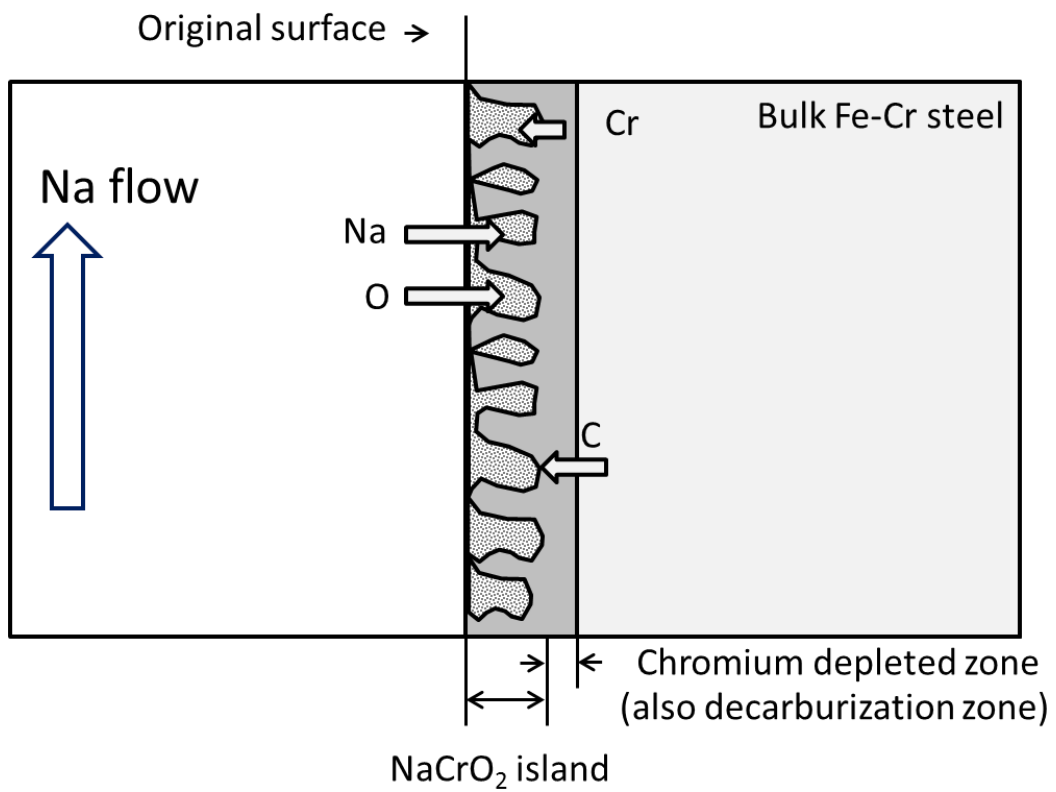
Original surface →

Na flow

Na

O

Cr

Bulk Fe-Cr steel

C

→ ← Chromium depleted zone
(also decarburization zone)

NaCrO$_2$ island

Figure 3-6. Schematic illustration of the surface of steel which was exposed to liquid sodium.

The effect of liquid sodium on the surface of Gr.92 steel was shown in Figure 3-4 and Figure 3-5 as changes including surface oxidation, decarburization, and chromium depletion, which may affect the precipitation behavior of steel.

In this study, carbon extraction replica samples were obtained from the FIB polished surface of specimens; the depth below the original surface is about 40 μm to 60 μm in the Cr-depleted zone. Precipitates obtained from the carbon extraction replica represent the effect of either liquid sodium or thermal aging. TEM images of the extraction replicas for the precipitates, and the representative composition of precipitates in the specimens, before and after exposure to sodium or argon at 650℃, are shown in Figure 3-7 and summarized in Table 3-2. In the as-received specimen, nano-sized precipitates were observed. Their representative composition to the metallic fraction was determined to be (in at%) 12.22Cr-69.84V-0.43Mo-17.51Nb (R1) indicating V-rich MX-type (M = Nb, V, Cr, W and X = C, N) carbonitride, and 31.50Fe-59.16Cr-1.24V-1.46Mo-6.64W (R2) indicating a complex compound of $(Cr, Fe, W, Mo)_{23}C_6$. The $M_{23}C_6$ carbides were detected mainly in the prior-austenitic grain boundaries, but occasionally in the subgrains and lath boundaries. The MX precipitates were usually found in the lath and lath boundaries. The average size of precipitates in this figure is 47 nm and the total count is 263. In microstructural investigations of normalized-and-tempered 9-12%Cr steels containing V, Nb, Mo, and W, $M_{23}C_6$ carbides precipitated on lath boundaries (typically 50-150 nm) and finely dispersed MX (20-50 nm) precipitates were observed [34]. The same types of precipitates are observed in the as-received specimen in this study. TEM images of the extraction replicas for precipitates in the sodium-exposed specimens are shown in Figure 2-7 (b); the compositions are summarized in Table 3-2 (b). Their representative composition to the metallic fraction was determined to be (in at%) 20.85Fe-71.09Cr-0.48V-1.95Mo-5.63W (R8) and 21.67Fe-70.74Cr-0.45V-1.65Mo-5.5W (R11), indicating a complex compound of $(Cr, Fe, W, Mo)_{23}C_6$. The $M_{23}C_6$ carbides were observed mainly in the interface region in sodium exposed specimen to the sodium environment. The average size and total count of precipitates is 113 nm and 140 for 1583 h in the sodium environment, and 218 nm and 104 for 3095 h. Another study of precipitates and carbides from steel after exposure to flowing sodium at 600℃ (with 0.016 wppm of dissolved carbon, for durations of 4,684 to 5,220 h) in Mod. 9Cr-1Mo identified $M_{23}C_6$, VC, NbC, M_6C, and Fe_2Mo; in 9Cr-2Mo steels, $M_{23}C_6$, M_6C, and Fe_2Mo [35]. The increase of chromium from 9 to 12 % accelerates the coarsening rate of Laves phase particles [36]. Since there is limited study regarding the effect of surface oxidation, decarburization, and chromium depletion on precipitate behavior in ferritic-martensitic steel in the literature, it is assumed that precipitation of the Laves phase in sodium-exposed specimens does not occur due to chromium depletion. Figure 3-7 (c) shows TEM images of extraction replicas for the specimens exposed to an argon environment.
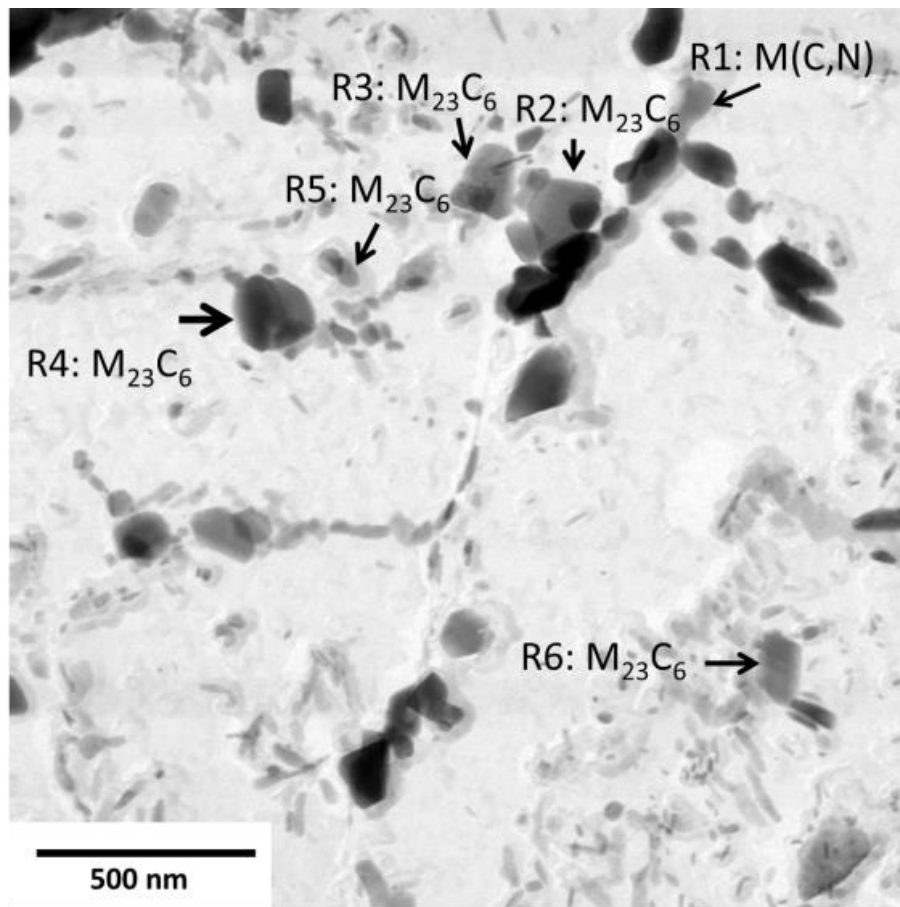
(a)
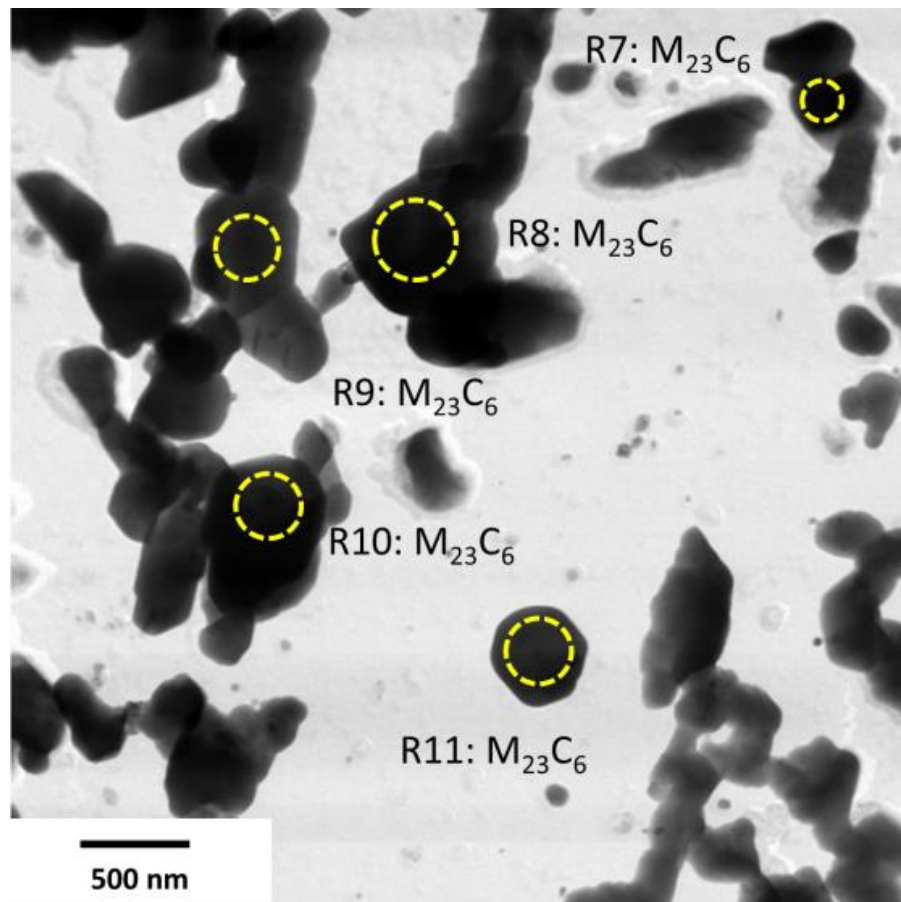
(b)
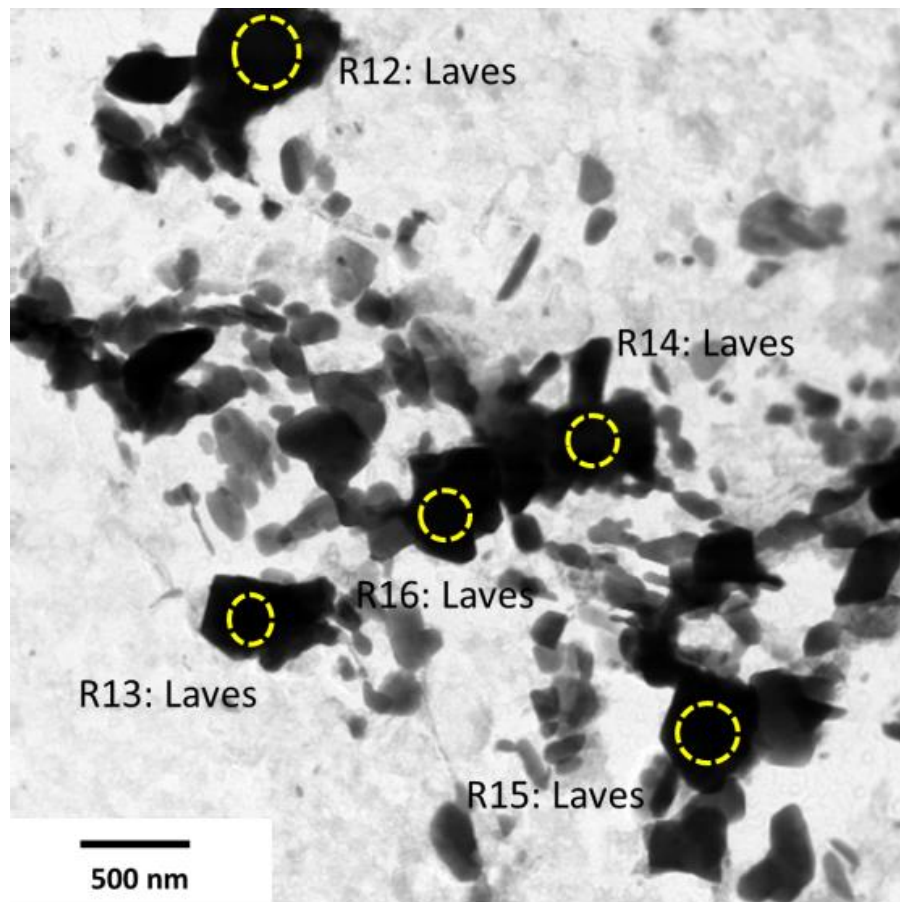
(c)

Figure 3-7. TEM image of extraction replicas for precipitates in the specimens (a) as-received, (b) 650°C sodium-exposed for 3095 h, and (c) 650°C argon-exposed for 2973 h.

Table 3-2. Representative compositions of the precipitates in the Gr. 92 specimen after exposed to sodium as well as to argon at 650°C (in at%).

(a)

Precipitates		Fe	Cr	V	Mo	Nb	W
As-received	R1	-	12.22	69.84	0.43	17.51	-
	R2	31.50	59.16	1.24	1.46	-	6.64
	R3	23.83	51.15	14.21	1.39	2.76	6.66
	R4	31.87	57.26	0.90	1.46	0.49	6.60
	R5	3.49	78.97	4.47	3.25	0.55	9.29
	R6	29.19	61.24	-	1.89	-	7.67

(b)

Precipitates		Fe	Cr	V	Mo	Nb	W
Na-exposed for 3095h	R7	22.54	69.55	-	2.10	-	5.81
	R8	20.85	71.09	0.48	1.95	-	5.63
	R9	23.77	68.23	0.71	2.18	-	5.12
	R10	22.23	68.92	1.81	1.69	-	5.33
	R11	21.67	70.74	0.45	1.65	-	5.50

(c)

Precipitates		Fe	Cr	V	Mo	Nb	W
Ar-aged for 2973h	R12	51.87	10.19	-	9.75	-	28.18
	R13	48.16	16.04	-	8.32	-	27.48
	R14	37.31	36.39	-	6.22	-	17.55
	R15	45.29	19.23	-	9.72	-	25.77
	R16	49.80	10.50	-	8.96	-	30.73

(a)

(b)

(c)

(d)

5 4
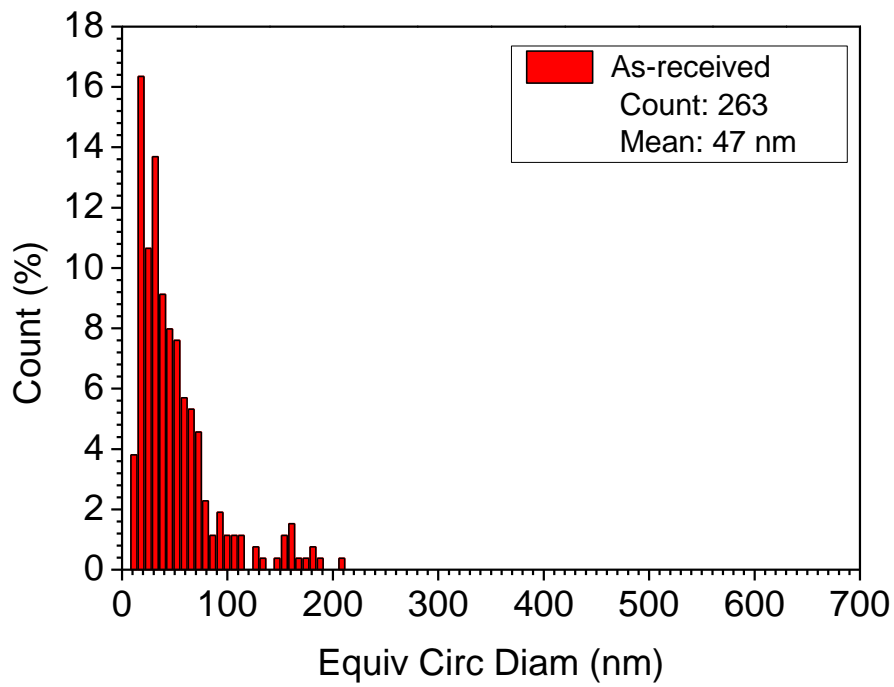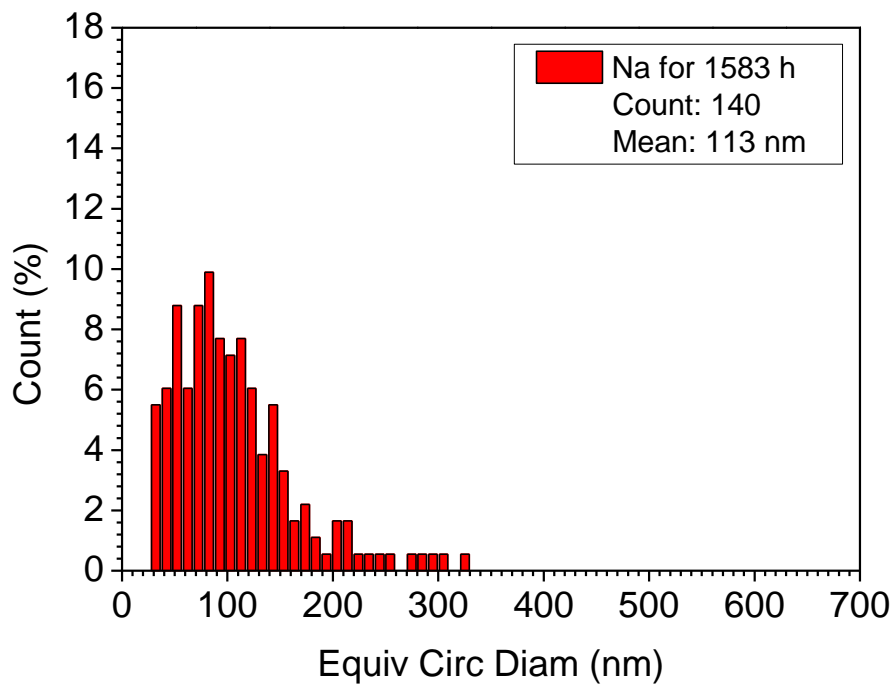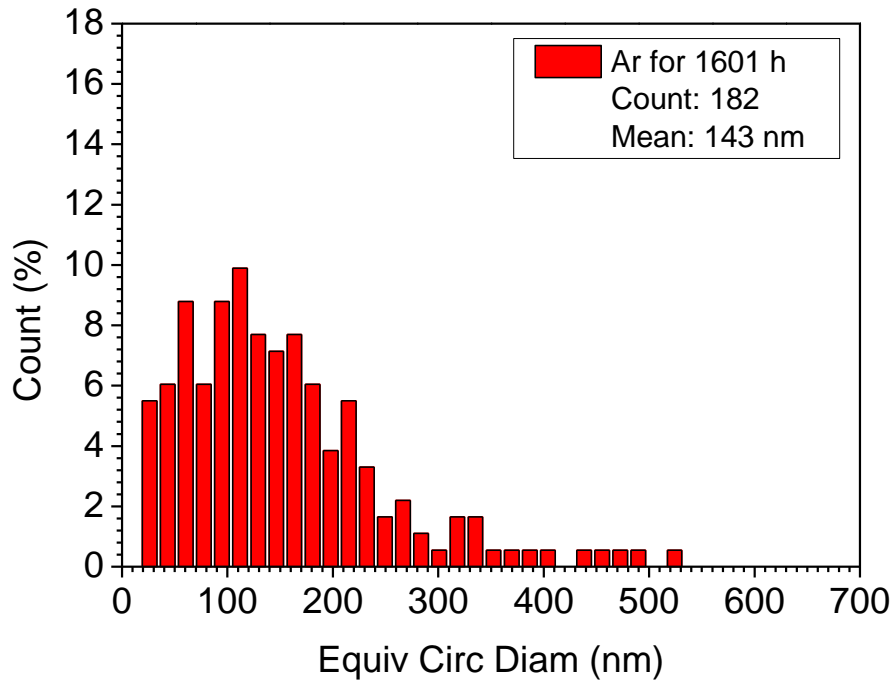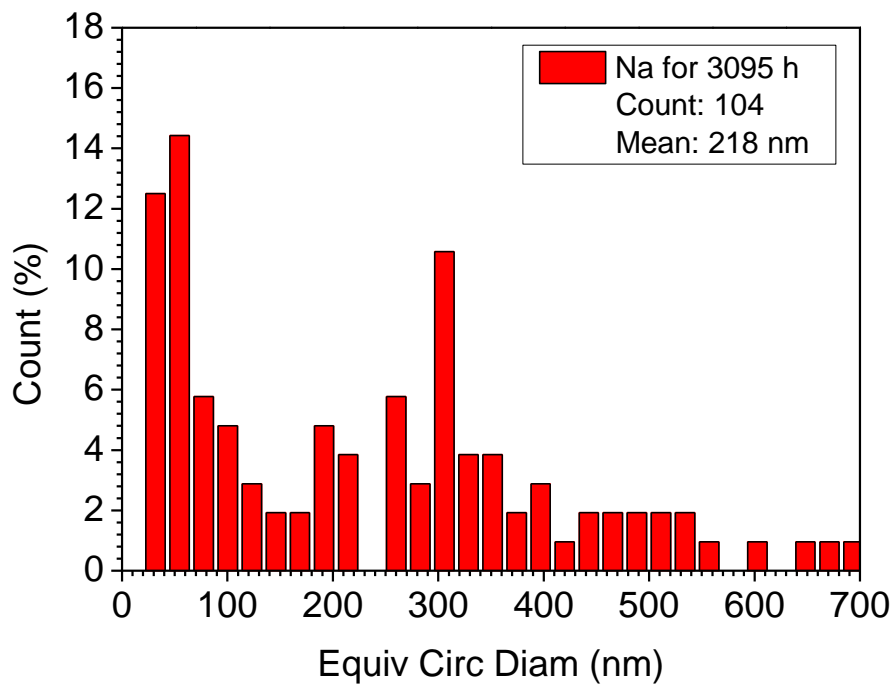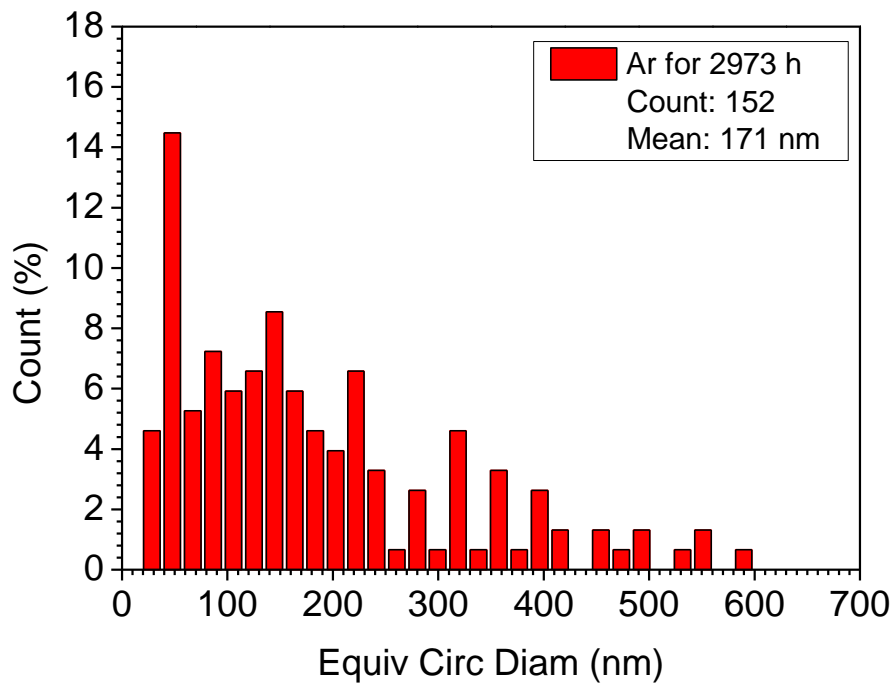
(e)

Figure 3-8. The graphs of the equivalent circle diameter (nm) of precipitates in the specimens showing percent of total count for (a) as-received specimen, (b) Na-exposed specimen after 1583 h, (c) Ar-exposed specimen after 1601 h, (d) Na-exposed specimen after 3095 h, (e) Ar-exposed specimen after 1601 h.

In case of the argon-exposed specimens, the carbon extraction region is near the surface. Representative compositions of the precipitates are given in Table 3-2 (c). Their representative composition to the metallic fraction was determined to be (in at%) 51.87Fe-10.19Cr-9.75Mo-28.18W (R12) and 49.80Fe-10.5Cr-8.96Mo-30.73W (R16) in Figure 3-7 (c). The Fe2(W,Mo) precipitates (Laves phase) were detected mainly in specimens exposed to argon. The average size and the total count of the precipitates is 143 nm and 182 for 1601 h and 171 nm and 152 for 2973 h with argon. With 9-12Cr-MoWVNb steels, after normalizing and tempering treatments, typically 50-150 nm of $M_{23}C_6$ on lath boundaries and no Laves phase were observed; when aged for 10,000-30,000 h, medium and large sized Laves phases were observed [35]. It is well known that the Laves phase is usually formed after long-duration aging at around 600℃, regardless of applied stress [37, 38]. In some 9-12% Cr and 1-2% Mo dual-phase steels with delta ferrite-martensite microstructure, Laves phase precipitation has been observed in delta ferrite in an early stage of aging [39, 40] for the nose temperature of the TTP diagram between 823 and 923 K [41]. Since Gr. 92 steel contains 1.64 wt% of tungsten and 0.38 wt% of molybdenum, higher than other FMS such as T91 and mod. T91, the propensity for Laves phase formation is increased [42]. Also, the TTP diagram of NF616 steel which has the almost same chemical composition with Gr. 92 steel, shows that the precipitation time of Laves phase at 923K aging environment is approximately 200 h [43]. Based on the literature mentioned above, the precipitation time of Laves phase at 650 ℃ in whole region of Ar-aged specimen and bulk steel (not near Cr-depleted zone) in Na-aged specimens is reasonable in this study.

In terms of size, the equivalent circle diameter (nm) of precipitates is shown in Figures 3-8 (a) to 3-8 (e) as a function of percent of total count and aging environment. These figures show that the equivalent circle diameter of precipitates in the as-received specimen is lowest, and precipitates observed with sodium exposure for 1583 h as well as argon for 1601 h had similar distributions. However, the equivalent circle diameter of the precipitates with sodium exposure for 3095 h shows a different distribution from argon exposure for 2973 h. Quantitative analysis of the precipitates shows that for the same environment, average size tends to increase with exposure time, while total count is decreased. The average sizes of $M_{23}C_6$ precipitates observed in S9 steel (9Cr-1.87W) aged at 650℃ for 2000 h and 10000 h are about 70 nm and 80 nm, respectively [36]. The coarsening of precipitates results in a decrease of the number of precipitates. The loss of W from solid solution in the steel actually contributes to the increased coarsening stability of $M_{23}C_6$ carbides, which is controlled mainly by the ferrite matrix content of substitutional elements, which have a high concentration in the carbide [44]. The growth rate of Laves phase is relatively high in the first 10^4 h [45]. Since the equivalent circle diameter of precipitates for sodium-exposed specimen for 3095 h shows higher percent of total count than that of the argon exposed specimen for 2973 h, the growth rate of $M_{23}C_6$

observed at the interface between Cr-depleted zone and bulk steel in the sodium-exposed specimens is higher than that of Laves phase in argon-exposed specimens.

To compare the carbon extraction replica results, precipitates were analysed at the FIB sample locations by HR-TEM. High-angle annular dark field scanning TEM (HADDF-STEM) was used to determine the precipitates. For sodium-exposed specimens, the first sample was fabricated at the interface between the Cr-depleted zone and the steel matrix and the second sample was fabricated at the bulk steel matrix at about 60-70 μm distance below the inner surface (opposite side to the Na-exposed surface). For Ar-exposed specimen, the sample was fabricated at 40-45 μm distance below the outer surface. The HAADF-STEM image of FIB sample-1 (at the interface between the Cr-depleted zone and the bulk steel matrix in specimen Na-exposed for 3095 h) is shown in Figure 3-9 (a); the types of precipitates are indicated and are mainly $M_{23}C_6$ carbide. The HAADF-STEM image of FIB sample-2 (at the bulk steel matrix near inner surface in specimen Na-exposed for 3095 h) is shown in Figure 3-9 (b); precipitates observed are mainly $Fe_2(W,Mo)$ (Laves phase). The HAADF-STEM image of FIB sample-3 (Ar-exposed for 2973 h) is shown in Figure 3-9 (c); most precipitates observed are $Fe_2(W,Mo)$ (Laves phase) as the same observed in Figure 3-9 (b). The same precipitates were observed in FIB sample-2 and FIB-sample-3 due to the fact that FIB-sample-2 was affected by only aging effect (not affected by Na). From both the TEM and HADDF-STEM analyses in Figure 3-7 (b), Figure 3-7 (c) and Figure 3-9, we conclude that the precipitates in Na affected zone in Na-exposed specimens were mainly $M_{23}C_6$ and the precipitates in bulk steel matrix in Na-exposed specimen and Ar-exposed specimens were mainly $Fe_2(W,Mo)$ (Laves phase).

On the basis of the chemical composition of Gr.92 steel, as shown in Table 3-1, the phases as a function of temperature calculated by using a computational thermodynamic program (JMatPro 8.0) are plotted in Figure 3-10. This steel can contain 4 types of precipitates at 650℃; $M_{23}C_6$, Laves, Z-phase and M(C,N). The $M_{23}C_6$ carbides are found to be sTable at temperatures up to 850℃. According to Figure 3-10, precipitation of Laves phase may occur at temperatures lower than its solution temperature, 725.1℃, and the volume fraction of Laves phase increases with decreasing temperature below 725.1℃. The equilibrium volume fraction of Laves phase at 650℃ is 1.55 wt%.

Noting that the $M_{23}C_6$ carbides observed at the interface between Cr-depleted zone and the bulk steel matrix in the sodium-exposed specimen result from mainly the chromium depletion and presumably the decarburization , the sensitivity of precipitate formation as functions of Cr-content and C-content was calculated using a computational thermodynamic program (JMatPro 8.0) and is shown in Figure 3-11. On the basis of the chemical composition of Gr.92 (original Cr-content 8.69 wt%), the first case is valid for early exposure times, with 7 wt% of Cr (1.69 wt% of Cr has been spent to form an oxide or depleted to liquid sodium).
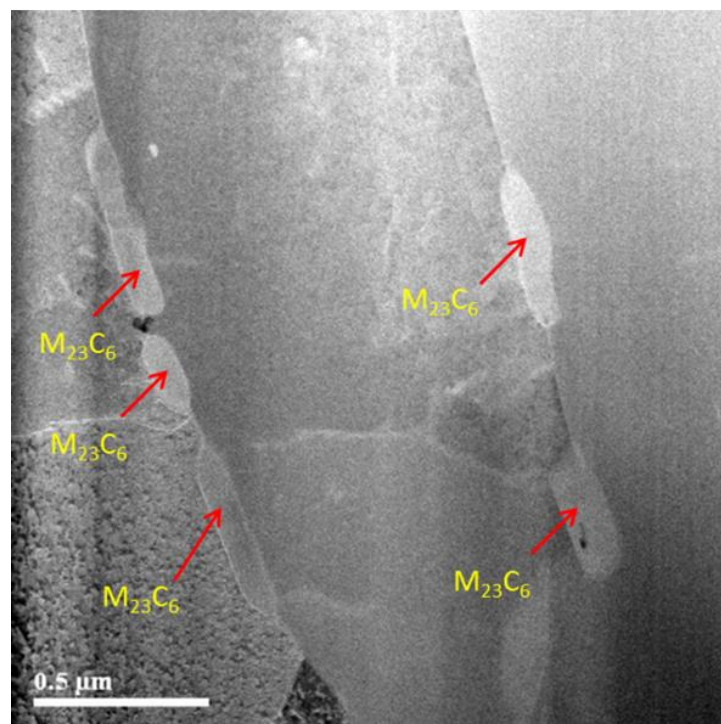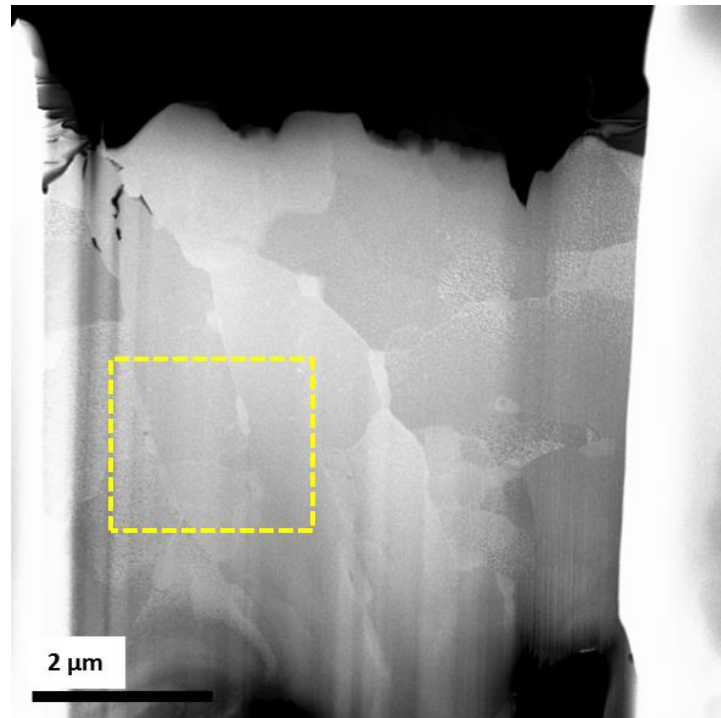
(a)
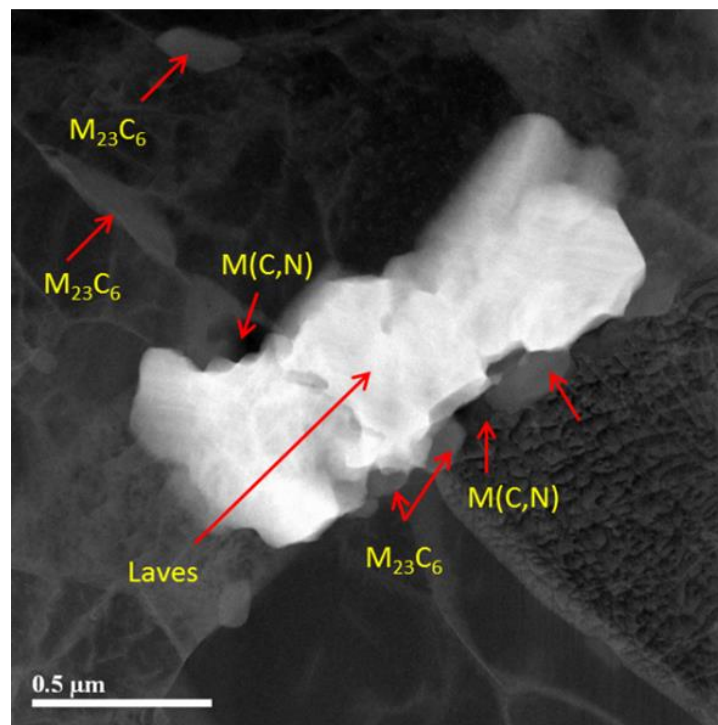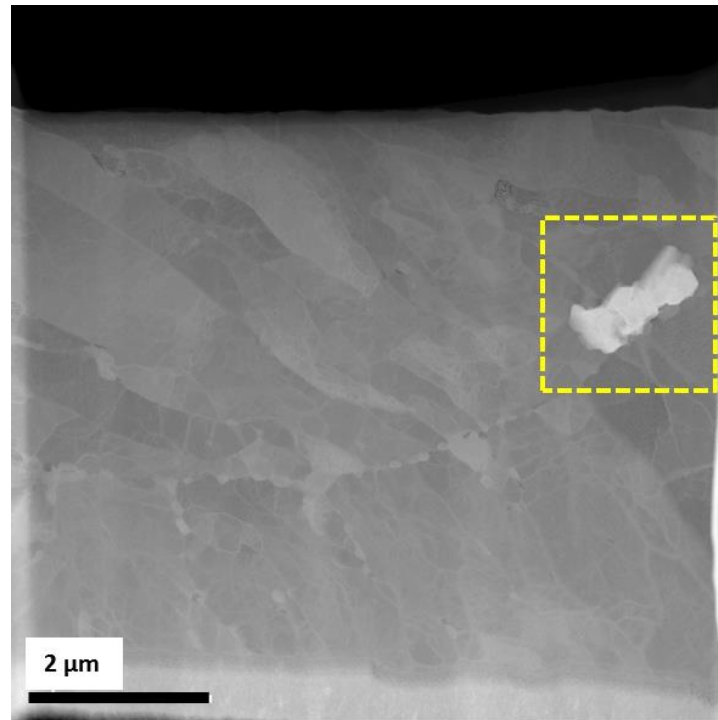
(b)
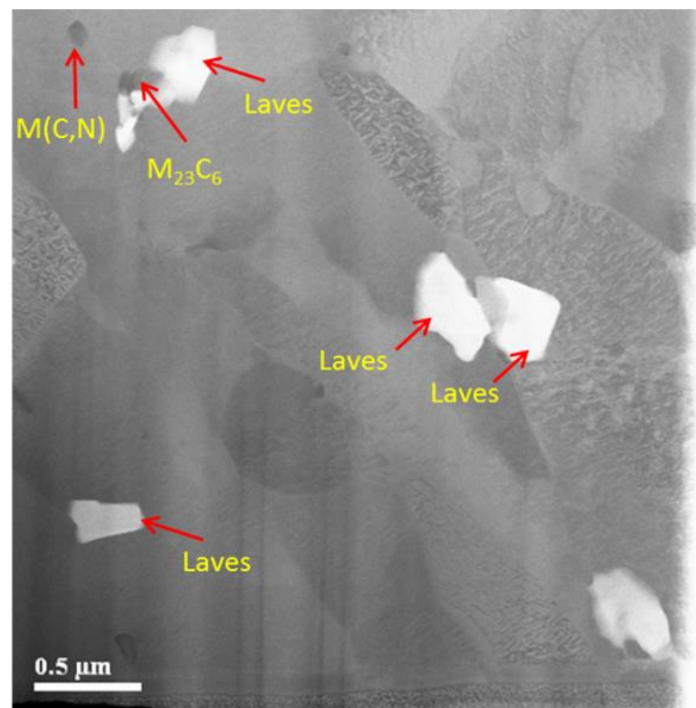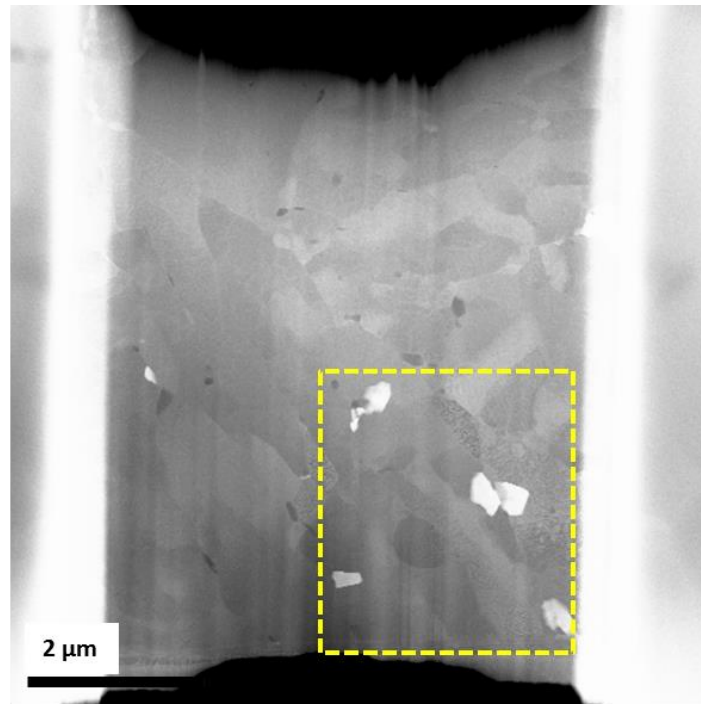
(c)

Figure 3-9. The HAADF-STEM images from samples fabricated by focused ion beam (FIB): (a) at the interface between the Cr-depleted zone and the bulk steel matrix in Na-exposed for 3095h, (b) at the bulk steel matrix near inner surface in Na-exposed for 3095h and (c) Ar-exposed for 2973h. (*Additional TEM analysises are in Appendix A.)
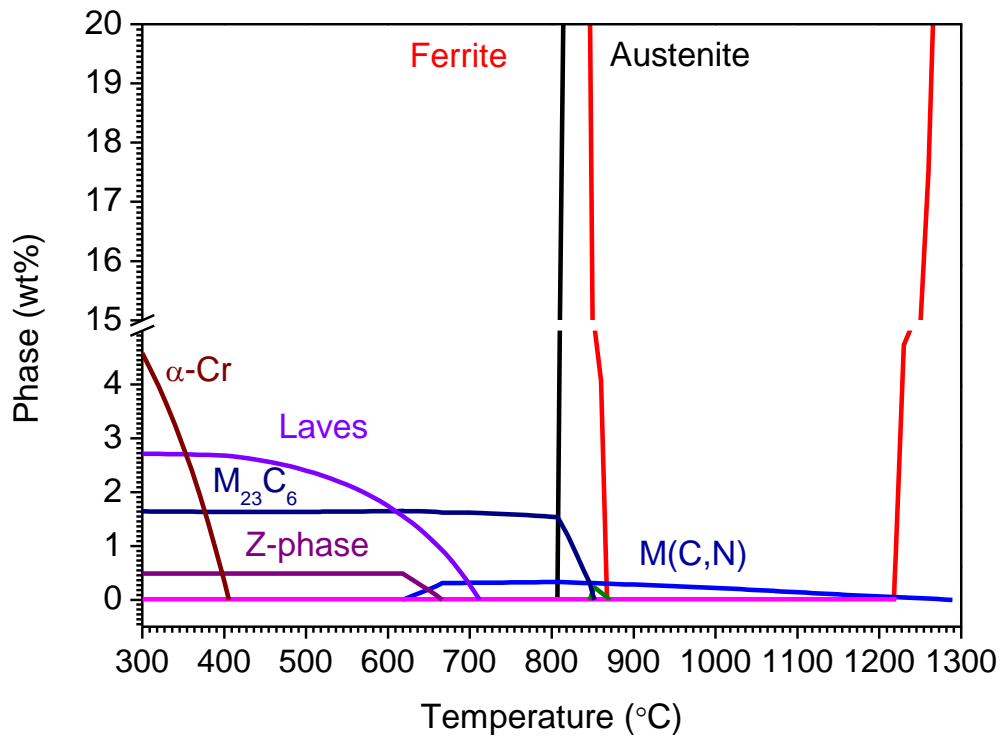
Figure 3-10. Phases in Gr.92 steel as a function of temperature (JMatPro 8.0).
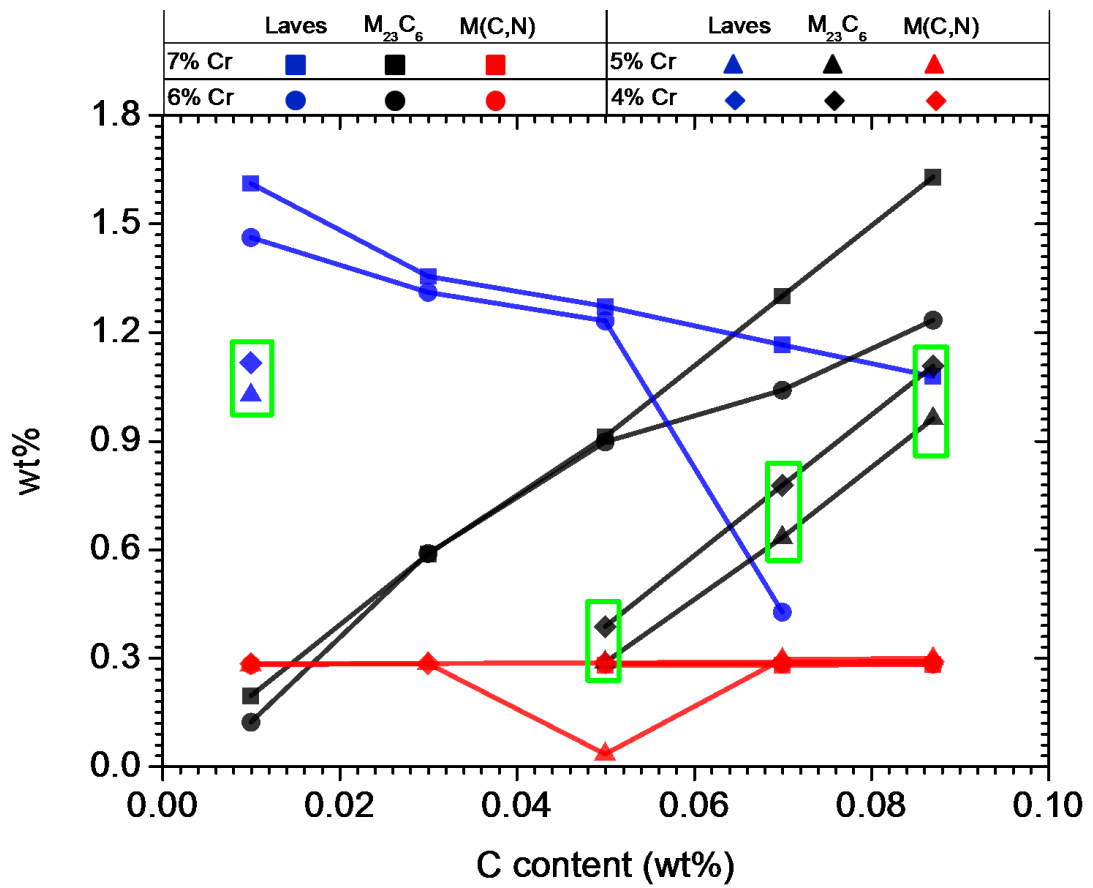
Figure 3-11. Sensitivity of the precipitates (M23C6, Laves, M(C,N)) as function of C-content as calculated by the computational thermodynamics program (JMatPro 8.0).

As C-content decreases, the amount of $M_{23}C_6$ also decreases while the amount of Laves phase increases. The general tendency of the second case (Cr-content 6 wt%), where 2.69 wt% of Cr has been spent to form an oxide or depleted to sodium, is similar to the first case. In the third and last cases, where 3.69 wt% and 4.69 wt% of Cr have been spent or depleted, simulating longer exposure time, thermodynamics predicts that Laves phase is not formed for most values of C content, except for 0.01 wt%. In these cases, $M_{23}C_6$ precipitate also exists between 0.087 wt% and 0.05 wt%. During HR-TEM analysis on FIB samples, a few points in the steel matrix (not precipitates) were analyzed by EDS. In the matrix, Cr-content varies from 4.09 at% to 5.3 at% (corresponding to 4.87 wt% and 6.24 wt%, respectively) in the FIB sample-1, and from 6.46 at% to 7.74 at% (corresponding to 5.9 wt% to 7.74 wt%, respectively) in the argon-exposed sample. In the FIB sample-1, precipitates represent mainly $M_{23}C_6$ carbide. Laves phase observed in the FIB sample-2 from the bulk steel matrix in Na-exposed specimen and in the FIB sample-3 from the Ar-exposed specimen, in where Cr depletion did not occur, is thermodynamically sTable, corresponding to the blue squares in Figure 3-11. So, there is presumably threshold Cr level to precipitate the Laves phase between 5 wt% and 6 wt% of Cr in the steel matrix at the temperature. Since Cr concentration at the interface between Cr depleted zone and the bulk steel matrix in Na-exposed specimen is almost lower than 6 wt%, Laves phase is not precipitated.

Since the carbon extraction replica and FIB samples show similar observations, it is concluded that the precipitate behavior in the near surface in Na-exposed specimen is affected by mainly intergranular oxidation ($NaCrO_2$) and chromium depletion into liquid sodium or into the oxide, and presumably decarburization.

3. 4 Conclusions

In order to investigate the effect of liquid sodium containing dissolved oxygen on precipitates in Gr. 92 steel, specimens were exposed to liquid sodium or to an argon environment at 650℃ for certain times up to 3095 h.

1. Intergranular oxidation ($NaCrO_2$) and a chromium depletion zone were observed at the surface for sodium-exposed specimens, but not observed in argon-exposed specimens.

2. V-rich MX-type carbonitride and $M_{23}C_6$ were found in the as-received specimen.

3. At the interface between Cr-depleted zone and the bulk steel matrix in specimens exposed to sodium, the main precipitate observed was $M_{23}C_6$, while Laves phase was the main observed precipitate in specimen at the bulk steel matrix in specimen exposed to sodium and in specimen exposed to the argon environment.

4. The equivalent circle diameter of precipitates in the as-received specimen is the lowest, while sodium-exposed (1583 h) and argon-exposed (1601 h) specimens have similar distributions. For longer exposure times, the equivalent circle diameter of precipitates for sodium-exposed specimens (3095 h) showed higher % than that in argon-exposed specimens (2973 h).

5. In a thermodynamic simulation of long sodium exposure time (depletion to 4 wt% and 5 wt% Cr in the matrix), Laves phase was not formed for most values of C-content (except 0.01 wt%).

3. 5 Reference

1. F.A. Garner, M.B. Tgoloczko, B.H. Sencer, J. Nucl. Mater. 276 (2000) 123-142.

2. D.S. Gelles, J. Nucl. Mater. 108 & 109 (1982) 515-526.

3. Y. Dai, B. Long, Z.F. Tong, J. Nucl. Mater. 377 (2008) 115-121.

4. S.H. Kim, B.J. Song, W.S. Ryu, J.H. Hong, J. Nucl. Mater. 329-333 (2004) 299-303.

5. T.K. Kim, J.H. Baek, C.H. Han, S.H. Kim, C.B. Lee, J. Nucl. Mater. 389 (2009) 359-364.

6. H. Tanigawa, H. Sakasegawa, N. Hashimoto, R.L. Klueh, M. Ando, M.A. Sokolov, J. Nucl. Mater. 367-370 (2007) 42-47.

7. J.S. Lee, H.G. Armaki, K. Maruyama, T. Muraki, H. Asahi, Mater. Sci. Eng. A 428 (2006) 270-275.

8. M. Taneike, F. Abe, K. Sawada, Nature 424 (2003) 294-296.

9. S. He ́mery, T. Auger, J.L. Courouau, F. Balbaud-Ce ́le ́rier, Corros. Sci. 83 (2014) 1-5.

10. R.L. Klueh, N. Hashimoto, P.J. Maziasz, J. Nucl. Mater. 367–370 (2007) 48-53.

11. F. Abe, Mater. Sci. Eng. A 387–389 (2004) 565-569.

12. T. Furukawa, S. Kato, E. Yoshida, J. Nucl. Mater. 392 (2009) 249-254.

13. K. Natesan, Metall. Mater. Trans. A. 6A. (1975) 1143-1153.

14. K. Natesan, M. Li, O.K. Chopra, S. Majumdar, J. Nucl. Mater. 392 (2009) 243-248.

15. V. Ganesan, V. Ganesan, J. Nucl. Mater. 256 (1998) 69-77.

16. J.C. Vaillant, B. Vandenberghe, B. Hahn, H. Heuser, C. Jochum, Int. J. Pres. Ves. Pip. 85 (2008) 38-46.

17. T. Suzuki, I. Mutoh, J. Nucl. Mater. 140 (1986) 56-62.

18. C.S. Jeong, S.Y. Bae, D.H. Ki, K. Watanabe, B.S. Lim, Mater. Sci. Eng. A 449–451 (2007) 155-158.

19. H. Tanigawa, H. Sakasegawa, N. Hashimoto, R.L. Klueh, M. Ando, M.A. Sokolov, J. Nucl. Mater. 367–370 (2007) 42-47.

20. F. Abe, T. Horiuchi, M. Taneike, K. Sawada, Mater. Sci. Eng. A 378 (2004) 299-303.

21. R.L. Klueh, D.R. Harries, High-Chromium Ferritic and Martensitic Steels for Nuclear Application, American Society for Testing and Materials, 2001. p. 33.

22. P. Skeldon, J.P. Hilditch, J.R. Hurley, D.R. Tice, Corros. Sci. 36 (1994) 593-610.

23.   J.P. Hildritch, J.R. Hurley, P. Skeldon, D.R. Tice, Corros. Sci. 37 (1995) 445-454.

24.   P.L.F. Rademakers, B.H. Kolster, J. Nucl. Mater. 97 (1981) 309-318.

25.   R.L. Dillon, I.S. Levy, BNWL-1901 (Rev.1) (1975).

26.   I. Proriol-Serre, O. Hamdane, J.B. Vogt, J.L. Courouau, in: Proceedings of International Congress on Advances in Nuclear Power Plants (ICAPP) 2011, Nice, France, May 2-5 (2011) 2403-2410.

27.   J.H. Kim, S.H. Kim, J. Nucl. Mater. 433 (2013) 112-119.

28.   J.H. Kim, J.M. Kim, J.E. Cha, S.H. Kim, C.B. Lee, Korean J. Met. Mater. 48 (5) (2010) 410-416.

29.   F.B. Ce´le´rier, J.L. Courouau, C. Desgranges, L. Martinelli, F. Rouillard, in: Proceedings of International Congress on Advances in Nuclear Power Plants (ICAPP) 2011, Nice, France, May 2-5 (2011) 2392-2402.

30.   J-L. Courouau, F.B. Ce´le´rier, V. Lorentz, T. Dufrenoy, in: Proceedings of International Congress on Advances in Nuclear Power Plants (ICAPP) 2011, Nice, France, May 2-5 (2011) 2439-2449.

31.   S. He´mery, T. Auger, J.L. Courouau, F. Balbaud-Ce´le´rier, Corros. Sci. 76 (2013) 441-452.

32.   I. Wolf, H.J. Grabke, Solid State Commun. 54 (1985) 5-10.

33.   K. Natesan, O.K. Chopra, T.F. Kassner, Nucl. Technol. 28 (1976) 441-451.

34.   H. Cerjak, V. Foldyna, P. Hofer, and B. Schaffernak, in: Microstructural development and stability in high chromium ferritic power plant steels, Eds. A. Strang and D.J. Gooch, (The Inst. of Materials, London, Book) 667 (1997) 53.

35.   T. Ito, S. Kato, M. Aoki, E. Yoshida, T. Kobayashi, Y. Wada, J. Nucl. Sci. Technol. 29 (1992) 367-377.

36.   H.G. Armaki, R.P. Chen, S. Kano, K. Maruyama, M. Igarashi, J. Phys. Conf. Ser. 240 (2010) 012085.

37.   M. Hattestrand, H.O. Andren, Acta. Mater. 49 (2001) 2123-2128.

38.   L. Korcakova, J. Hald, M.A.J. Somers, Mater. Charact. 47 (2001) 111-117.

39.   Y. Hosoi, N. Wade, S. Kunimitsu, T. Urita, J. Nucl. Mater. 141-143 (1986) 461-467.

40.   T. Fujita, K. Asakura, T. Sawada, T. Takamatsu, Y. Otoguro, Met. Trans. 12A (1981) 1071-1079.

41.   M. Tamura, H. Hayakawa, A. Yoshitake, A. Hishinuma, T. Kondo, J. Nucl. Mater. 155-157 (1988) 620-625.

42.   P.J. Ennis, A. Czyrska-Filemonowicz, Sādhanā. 28 (2003) 709–730.

43. H. Mimura, M. Ohgami, H. Naoi, T. Fujita, in: Materials for Advanced Power Engineering Part-1, Eds. D. Coutsouradis, Kluwer Academic Publish (1994) 361-372.

44. J. Hald, Int. J. Press. Vessels Pip. 85 (2008) 30-37.

45. C.G. Panait, W. Bendick, A. Fuchsmann, A.F. Gourgues-Lorenzon, J. Besson, Int. J. Press. Vessels Pip. 87 (2010) 326-335.

IV. OXYGEN MEASUREMENT

4. 1 Introduction

Liquid sodium is used as a primary coolant for sodium-cooled fast reactor (SFR). The demanding application for oxygen monitoring is the detection of background concentration changes caused by the initiation of leaks in the heat exchanger and by the refueling period of sodium-cooled fast reactor [1]. The rate of corrosion of stainless steel as cladding materials in liquid sodium environment is found to increase with the concentration of dissolved oxygen in the sodium, given that dissolved oxygen may accelerate one of the steps in the corrosion process [2]. The effect can be either thermodynamic or kinetic. It is, in practice, impossible to prevent the formation of sodium oxides, such as Na_2O and $NaCrO_2$, in the structural materials in sodium-cooled fast reactor. However, the total amount of chromium leached out of the material by the formation of Na_2O and $NaCrO_2$ depends on the amount of oxygen that gains entry into the system [3-6].

Liquid sodium could dissolve many of products such as oxides, hybrids, etc., but when it cooled, the solubility of these products decreases and they would be able to settle on the accessible materials. This physical principle enabled the sodium to be purified by means of cold-trap [7]. For the cold-trap calibration in sodium system, the cold-trap temperature and the oxygen concentration were correlated by measuring the oxygen levels in the sodium at various cold-trap temperatures [8-10]. However, the solubility of oxygen in liquid sodium at lower than 300 ℃ shows different behavior compared to those above 300 ℃ [11]. At low temperature, oxygen solubility in liquid sodium was measured by method of amalgamation with mercury [12-15], vacuum distillation [16], and extrapolated from high temperature measurement. Due to the limitation of the use of solid electrolytes at lower temperature, other methods such as amalgamation with mercury and vacuum distillation were used to determine oxygen solubility in liquid sodium at low temperature.

Oxygen-ion-conducting solid oxide electrolytes are well known, and their properties have been comprehensively reviewed [17-20]. The most common commercially available solid electrolyte materials are those based on zirconia (ZrO_2) and thoria (ThO_2) because of their recognized thermochemical stability in liquid metal systems. Doping these materials with metal oxides having di- or trivalent cations, such as Y_2O_3, Gd_2O_3, and Sm_2O_3, generates oxygen ion vacancies in the anion sublattice. The consequent increase in the oxygen ion conductivity may lead to a situation where the electrical conductivity in the solid is essentially ionic within certain ranges of temperatures and oxygen partial pressure [17]. Among the various cells, the zirconia-based potentiometric cell is widely used and is recognized to be stable in liquid metals such as lead or lead alloys [18]. Zirconia-based

electrolytes reportedly exhibit good long-term stability in sodium with an upper temperature limit for compatibility with sodium at 350 ℃ [19]; in certain cases, temperature limits in the range of 350 ℃– 500 ℃ have been reported [20-22].

Herein, as a step in the development of an on-line oxygen-concentration measurement system for application in the liquid sodium environment, a ceria-based solid electrolyte is introduced for lower temperature application (~200 ℃) with the cold-trap calibration. Ceria-based electrolytes exhibit high ionic conductivity compared to zirconia- and thoria-based electrolytes and thus has been actively researched [23-25]. The high electrical conductivity, and thermal and sintering properties of ceria-based solid electrolytes, which are widely utilized in solid oxide fuel cells (SOFCs) at moderate temperature, have been reviewed [26-28].

In this study, thermochemical stability test and conductivity measurements tests for both GDC-10A and GDC-10B solid electrolytes in liquid sodium at 200 ℃ are reported herein to evaluate the use of these electrolytes in liquid sodium environment. And electromotive force (emf) measurement of gadolinia doped ceria (GDC) solid electrolyte based potentiometric cell with In/In_2O_3 reference electrodes in oxygen saturated sodium has been performed to measure oxygen solubility in sodium at low temperature in where it has been used for the SFR application.

In the primary and secondary heat transport system in sodium-cooled reactors, nonmetallic elements, such as carbon, oxygen, and nitrogen, in sodium have a large effect on corrosion rates and the mechanical behavior of materials.

4. 2 Experimental

Solid electrolyte tubes with one end closed were manufactured for the development of a potentiometric cell based on GDC-10. Solid electrolyte was produced by Read-Ox Consultancy via the slip cast technique; gadolinia-doped ceria, GDC-10A and GDC-10B, $(Ce_{0.90}Gd_{0.10})O_{1.95}$ (surface area: 30–40 m^2/gram for GDC-10A and 5-8 m^2/gram for GDC-10B) powders were obtained from Fuel Cell Materials (FCM). The GDC-10A and GDC-10B powders were sintered in air at 1400 ℃ for 1 h and at 1650 ℃ for 2 h, respectively. Table 4-1 summarizes some of the morphological properties of these powders and the sintered tubes used for the solid electrolytes.

For GDC-10A sample, at the open end of the tube, the dimensions were as follows: outer diameter (OD): 6.0 mm, inner diameter (ID): 3.3 mm, and at the lower closed end: OD: 5.7 mm and ID: 3.0 mm. For GDC-10B sample, at the open end of the tube, the dimensions were as follows: outer

diameter (OD): 8.2 mm, inner diameter (ID): 4.0 mm, and at the lower closed end: OD: 7.5 mm and ID: 3.7 mm. The length of the tube was 100 mm for all samples.

The thermochemical stability of the sintered ceramics in oxygen-saturated sodium was studied using the manufactured tubes of the GDC-10A and GDC-10B that were exposed to sodium at 200 ℃ for 1 h. The sodium used in this study was 99.8% pure and was oxygen saturated.

Scanning electron microscopy (SEM) and energy dispersive spectrometry (EDS) were used to evaluate the microstructure of the as-sintered and post-exposed ceramics. X-ray diffraction (XRD) was used to determine the crystal-phase composition of the sintered GDC samples.

After exposure to liquid sodium at 200 ℃, the crystal-phase composition of the GDC samples and the microstructure of the surface that had been in contact with sodium were investigated by means of SEM, EDS, and XRD. The ceramic samples were ultrasonically cleaned in ethanol for 1 h and then in deionized water for 1 h, to remove the sodium before SEM and XRD analyses. For all characterization studies that are discussed in the subsequent sections of this paper, subsamples were cut from these sintered solid electrolyte tubes using a low speed saw with a diamond saw blade.

Electrical conductivity measurements were performed by means of a standard four-probe technique using a BioLogic Potentiostat, in the temperature range between 200 ℃ and 700 ℃, with rectangular samples (10 mm × 3.5 mm × 1.5 mm) of the sintered ceramics. Samples for conductivity measurements were prepared from sintered pellets (rectangular bars with Pt wire winding across the surface of the samples), and Ag paste was used as a contact adhesive. Platinum current leads were attached to the sample end surfaces, which were coated with Ag paste, and platinum voltage leads were wound around the sample in two circumferential grooves (of 0.3 mm width and 0.2 mm depth) at a distance of 2 mm from the end surfaces. A constant current of 100 mA was applied over the sample. The voltage difference over the voltage leads was measured using a BioLogic Potentiostat.

Table 4-1. Nomenclature, composition, and properties of the starting powders and manufacturing/sintering conditions, and density of sintered samples of the ceramics evaluated in this study.

Sample nomenclature	Composition	Specific surface area of powder (m^2/g)	Grain size of powder, d_{50} (μm)	Manufacturing process	Sintering conditions	Density of as-sintered samples (%theoretical)
GDC-10A	$(Ce_{0.9}Gd_{0.1})O_{1.95}$	30–40[a]	0.1–0.4[a]	Slip casting[b]	1 h in air at 1400 ℃	98
GDC-10B	$(Ce_{0.9}Gd_{0.1})O_{1.95}$	5–8[a]	0.1–0.4[a]	Slip casting[b]	2 h in air at 1650 ℃	98

[a] Reported on the analysis certificate supplied by Fuel Cell Materials (USA).

[b] At ReadOx & Consultancy b.v. (Valkenswaard, The Netherlands).

(a)
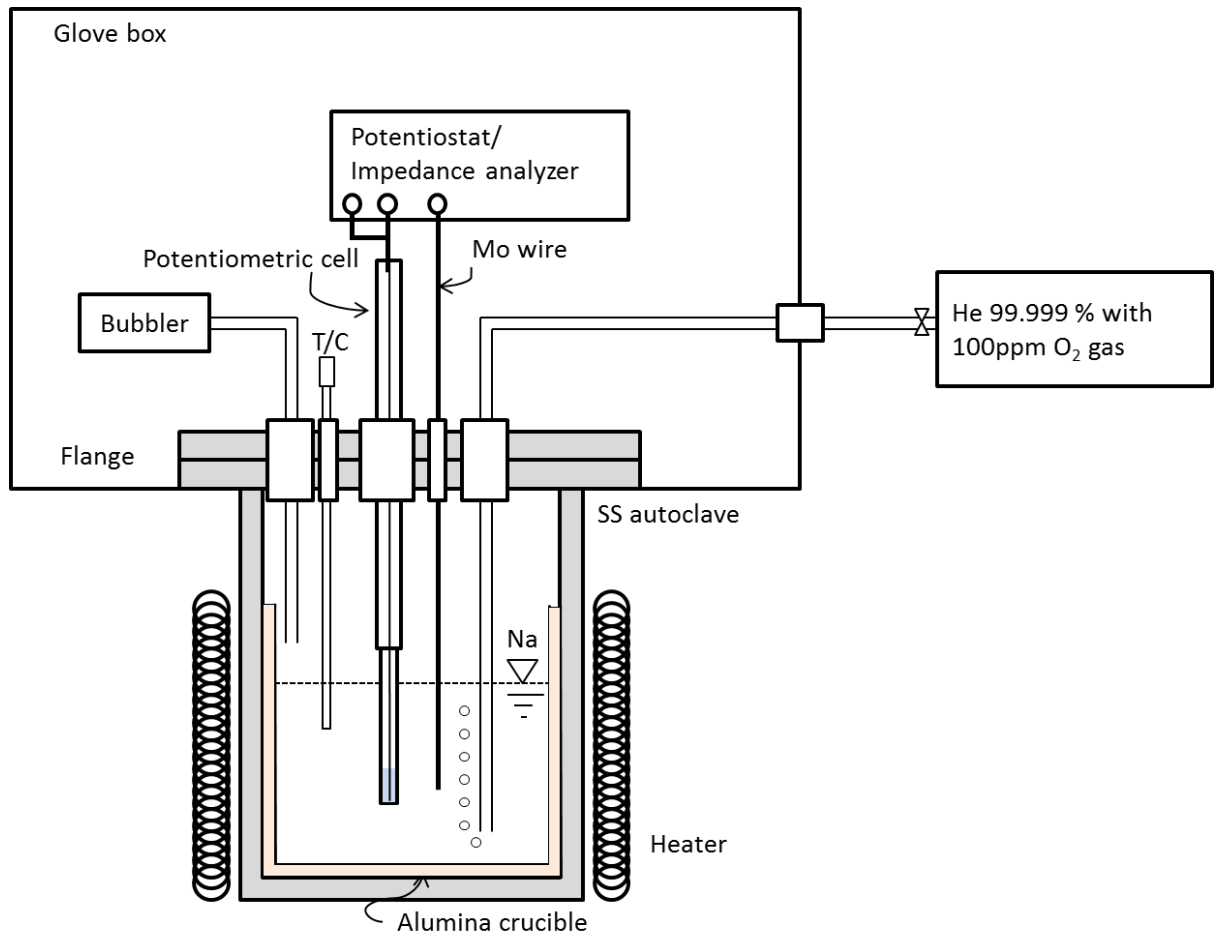
(b)

Figure 4-1. Image of potentiometric cell (a) and schematic of the experimental system (thermocouple, potentiometric cell, molybdenum wire in the alumina cell) (b).
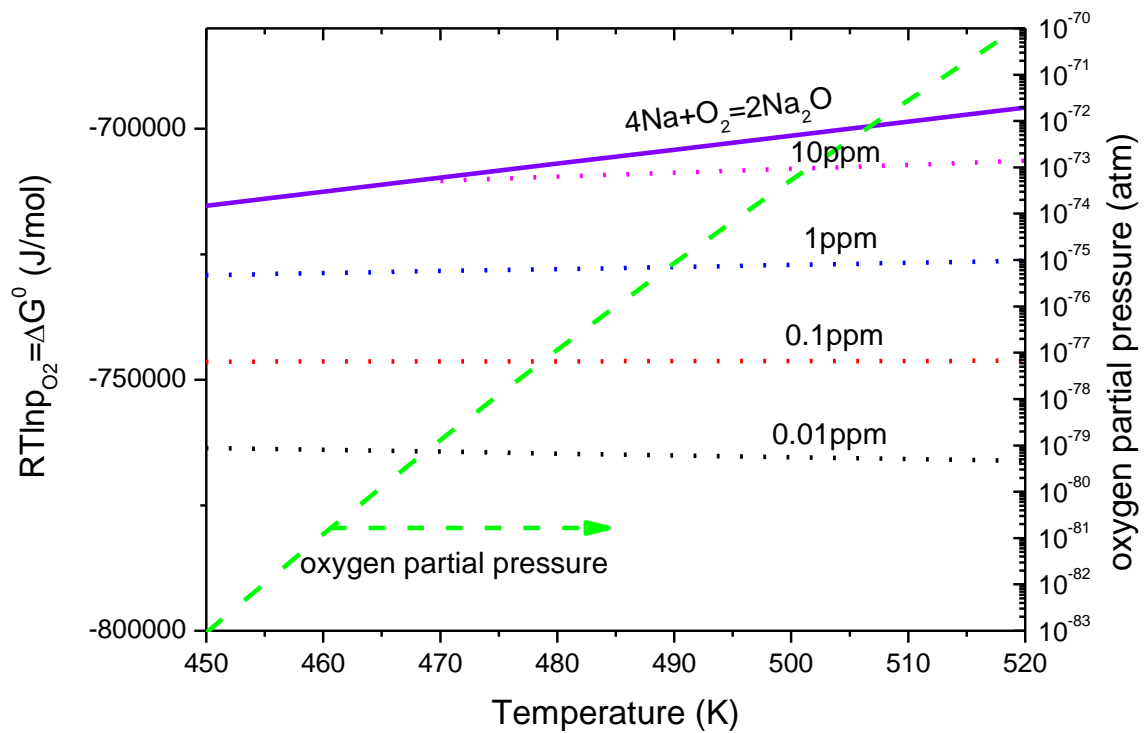
Figure 4-2. Na-O thermodynamic system with dissolved oxygen content (ppm) and oxygen partial pressure (atm) corresponding to 4Na+O₂=2Na₂O reaction.

The potentiometric cells used in this study were fabricated with $(Gd_{0.10}Ce_{0.90})O_{1.95}$ powder as a solid electrolyte. As a reference electrode, a mixture of indium powder (99.998%, Alfa Aesar) and In_2O_3 powder (99.997%, Alfa Aesar), which can develop equilibrium oxygen partial pressure at given temperature, was loaded into both GDC-10A and GDC-10B tubes under argon gas environment. As a lead wire for the reference side, molybdenum wire (99.95%, 0.5mm dia, Alfa Aesar) was connected with a ceramic feedthrough (CeramTec). For the sealing of the cell, cement joining which has similar the coefficient of thermal expansion with Fe-Ni alloy was introduced between Fe-Ni alloy and both GDC tubes. In order to achieve helium leak late lower than 10^{-9} mbar l/s at room temperature, the method was introduced in this study (Appendix B).

Emf signal measurements of GDC based potentiometric cells was performed by using open circuit potential technique with Solatron potentiostat 273A in oxygen saturated sodium at 450-520K. Galvanic cell used in this study can be represented as below:

$$Mo, Na, Na_2O | GDC | In, In_2O_3, Mo$$

Schematic of the experimental system is shown in Figure 4-1. An alumina crucible was used as sodium container. About 500 ml of sodium was introduced in the alumina crucible. Molybdenum wire was used as an electrical lead wire for the side of the working electrode. The covers of cell were filled with 99.999 % helium bubbling with 100 ppm O_2 for 10 h for the oxygen saturation in liquid sodium. The emf was measured while keeping the sodium temperature at 450–520 K. K-type thermocouple was inserted into the liquid sodium. The immersion depth of cell in sodium was about 40mm.

The Na-O thermodynamic system used in this study is shown in Figure 4-2. Oxygen contents in the test cell for this study are put on the oxygen limit such as oxygen solubility in the graph. In oxygen saturated condition, dissolved oxygen exists as the form of Na_2O. In the temperature range, 450-520K, the range of oxygen partial pressure in liquid sodium is between 10^{-83} atm and 10^{-70} atm.

4. 3 Methodology

The difference between the oxygen partial pressure at the reference electrode and that at the working electrode generate emf (E) according to Nernst Eq.:

$$E = \frac{RT}{4F} \ln(\frac{p_{O_2,ref}}{p_{O_2,Na}}),$$

(4-1)

where $p_{O_2,ref}$ is oxygen partial pressure at reference electrode, $p_{O_2,Na}$ is oxygen partial pressure at liquid sodium, R is the gas constant (8.314 $JK^{-1}mol^{-1}$), T is the absolute temperature (K), F is the

Faraday constant (96485.35 C mol^{-1}). By introducing a reference electrode with known oxygen partial pressure, the oxygen partial pressure at working electrode can be calculated from measured emf.

$$\ln p_{O_2,ref} = \frac{2\Delta_f G^0_{In_2O_3}}{3RT},$$

(4-2)

where $\Delta_f G^0_{In_2O_3}$ is the standard molar Gibbs free energy of formation of In$_2$O$_3$.

Assuming that the dissolved oxygen in Na obeys Henry's law up to the solubility limit, the activity of dissolved oxygen in Na can be derived as follow:

$$\ln p_{O_2,Na} = \frac{2\Delta_f G^0_{Na_2O}}{RT} + 2\ln(\frac{c_O}{c_{O,S}}),$$

(4-3)

where $\Delta_f G^0_{Na_2O}$ is the standard molar Gibbs free energy of formation of Na$_2$O and $c_{O,S}$ is solubility of oxygen in sodium. By combining Eq. 3-1, Eq.3- 2, and Eq. 3-3 become as follow:

$$E = \frac{RT}{4F}(\frac{2\Delta_f G^0_{In_2O_3}}{3RT} - \frac{2\Delta_f G^0_{Na_2O}}{RT} - 2\ln\frac{c_O}{c_{O,S}}),$$

(4-4)

where the Gibbs free energy of the formation of the oxide and oxygen solubility in liquid sodium is as follow [29, 30]:

$$\Delta_f G^0_{In_2O_3}(J/mol) = -925021 + 320.05T$$

(4-5)

$$\Delta_f G^0_{Na_2O}(J/mol) = -421008 + 145.362T$$

(4-6)

$$\log c_{O,S}(wt.\%) = 0.65 - \frac{1766}{T}(T < 488K)$$

(4-7)

Inserting the thermodynamic data into Eq. 3-4, the theoretical emf as a function of the dissolved oxygen concentration in liquid sodium is given by the following Eq.:

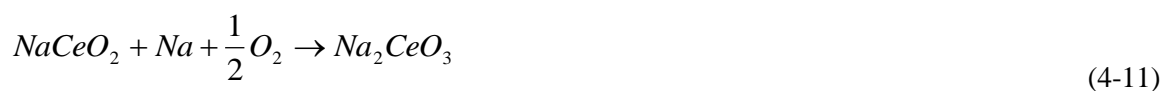$$E = 0.40863 - 1.3593 \times 10^{-4} T - 9.922 \times 10^{-5} T \log c_O,$$
(4-8)

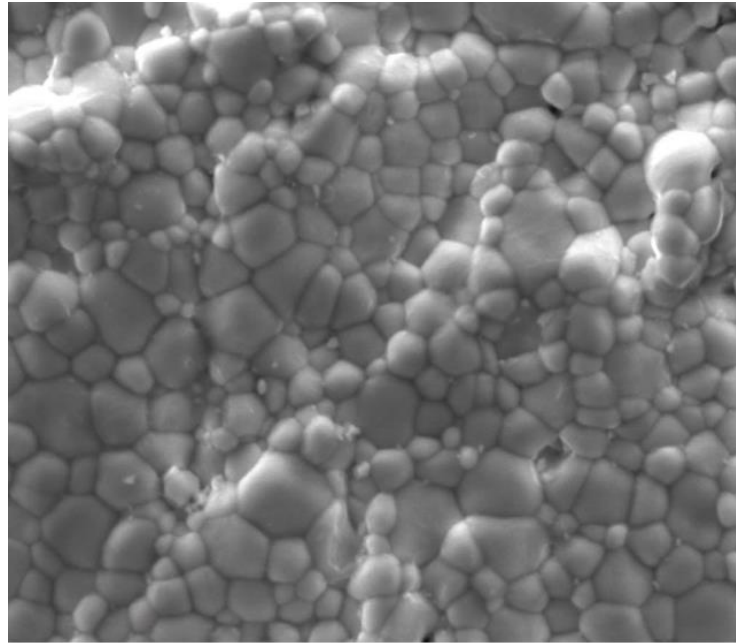where E is in V and is c_O in wt%.

4. 3 Results and Discussion

Figure 4-3 (a) shows the scanning electron micrographs (SEM) of the surfaces of the GDC-10A sample sintered in air at 1400 ℃ for 1 h. The average grain sizes of the as-sintered GDC-10A sample were determined from the SEM image and were about 0.5 μm. There are no open pores on the surface, but closed pores comprising 1–2% were observed on the surface. Figure 4-3 (b) shows the energy dispersive spectroscopy (EDS) peaks. Cerium, gadolinium, and oxygen peaks were clearly observed in these analyses. Figure 4-3 (c) shows the SEM image of the surfaces of the GDC-10B sample sintered in air at 1650 ℃ for 2 h. The average grain sizes of the as-sintered GDC-10B sample were determined from the SEM image and were about 4 μm. The EDS peaks of this sample were shown in Figure 4-3 (d).

After exposure to oxygen-saturated sodium at 200 ℃, defected microstructures were observed in the SEM images of the GDC-10A and GDC-10B samples as shown in Figure 4-4. However, EDS analysis (Figures 4-4 (b) and 4-4 (d)) showed the absence of sodium peaks.
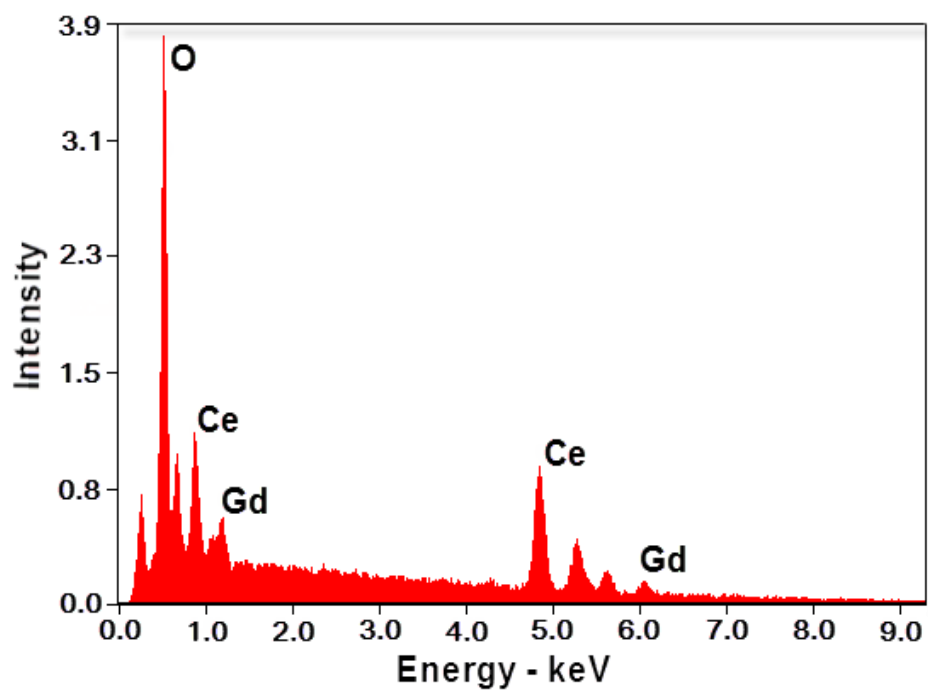
It is reported that cerium oxides (CeO_2 and Ce_2O_3) easily react with sodium oxides (Na_2O and Na_2O_2) to form compound products ($NaCeO_2$ and Na_2CeO_3, respectively) at high temperature sodium. The oxygen concentration thresholds for these two compounds ($NaCeO_2$ and Na_2CeO_3) at 700 K are 11.7 wppm, 7.3 wppm, and 4.9 wppm for $NaCeO_2$ and 10.9 wppm, 7.1 wppm, and 4.6 wppm for Na_2CeO_3, respectively, depending on oxygen solubility values [31, 32]. The chemical reactions of the ternary compounds are as follows:
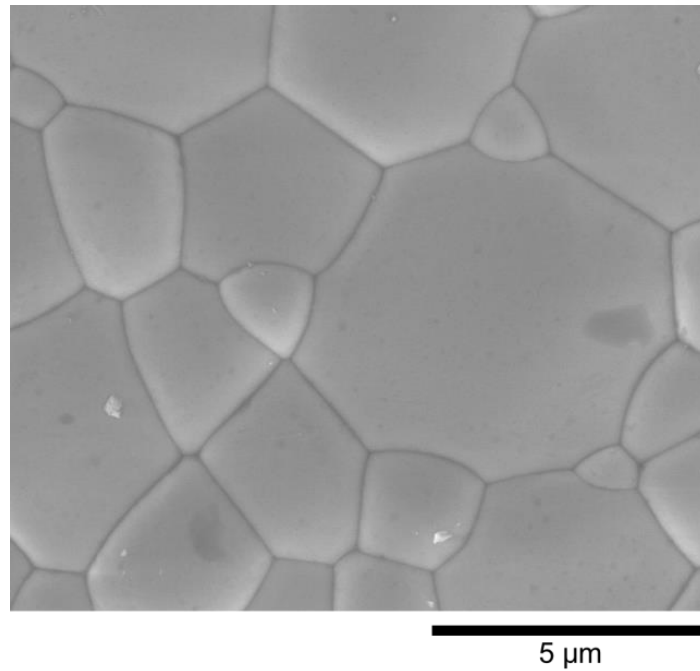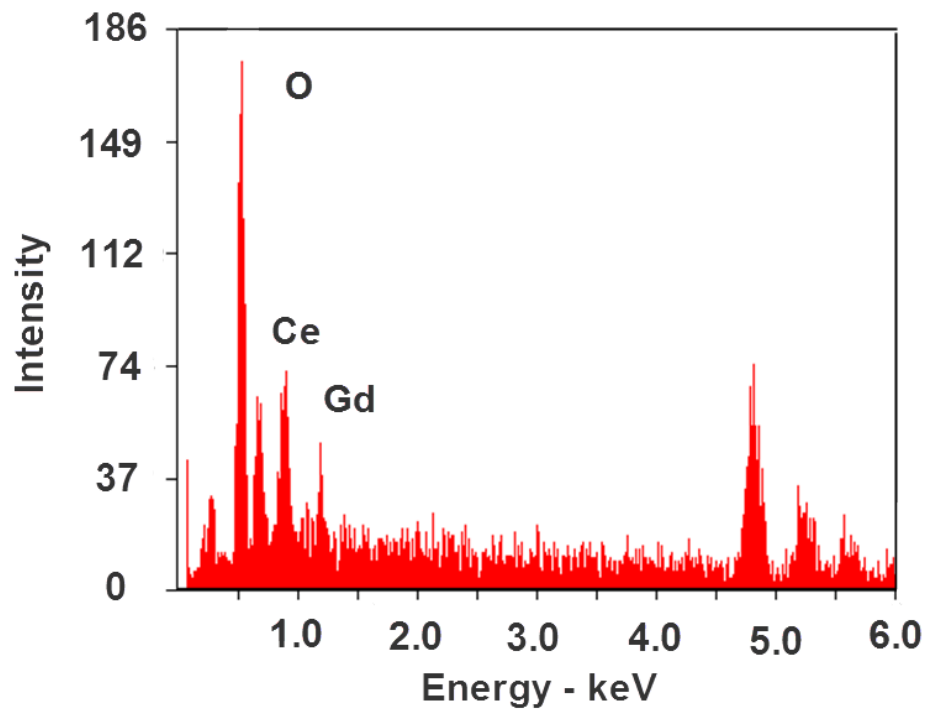
$$Na + CeO_2 \rightarrow NaCeO_2$$
(4-9)

$$CeO_2 + Na_2O \rightarrow Na_2CeO_3$$
(4-10)

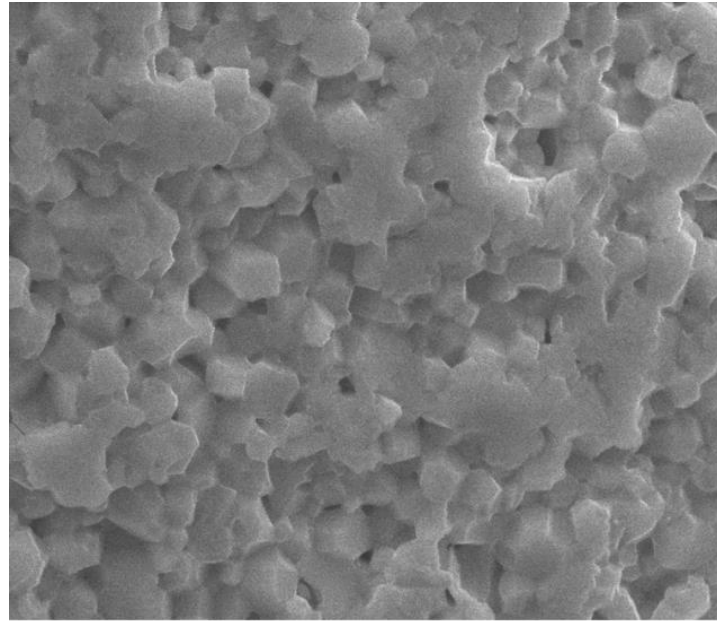$$NaCeO_2 + Na + \frac{1}{2}O_2 \rightarrow Na_2CeO_3$$
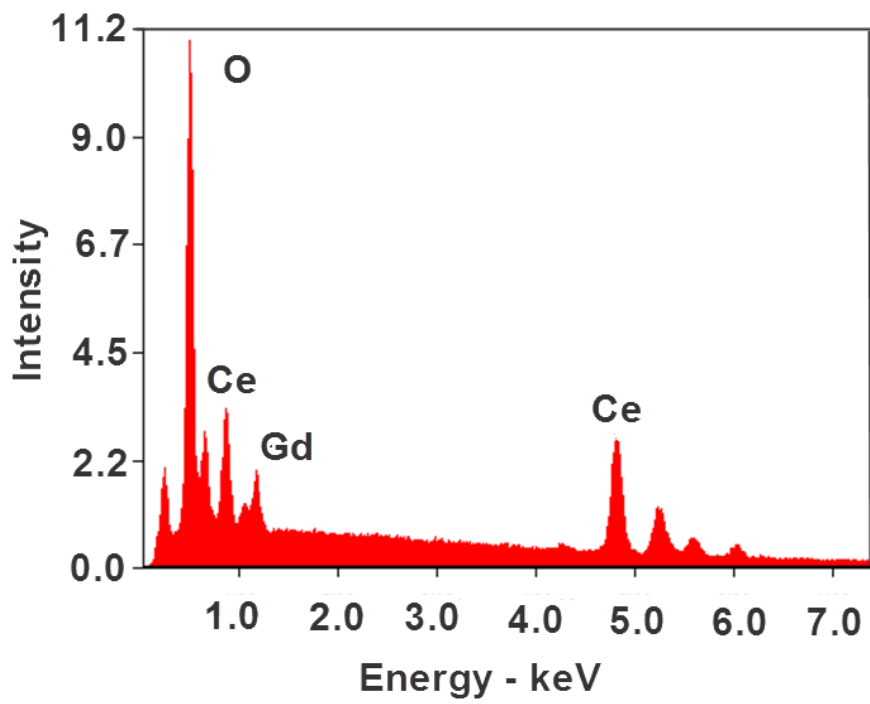(4-11)

(a)

(b)

7 7

5 μm

(c)

(d)

Figure 4-3. Microstructure of the as-sintered gadolinia doped ceria (GDC-10A) (SEM image, ×20,000 magnification) (a); EDS peaks of GDC-10A (b); gadolinia doped ceria (GDC-10B) (SEM image, ×20,000 magnification) (c); EDS peaks of GDC-10B (d).

7 8

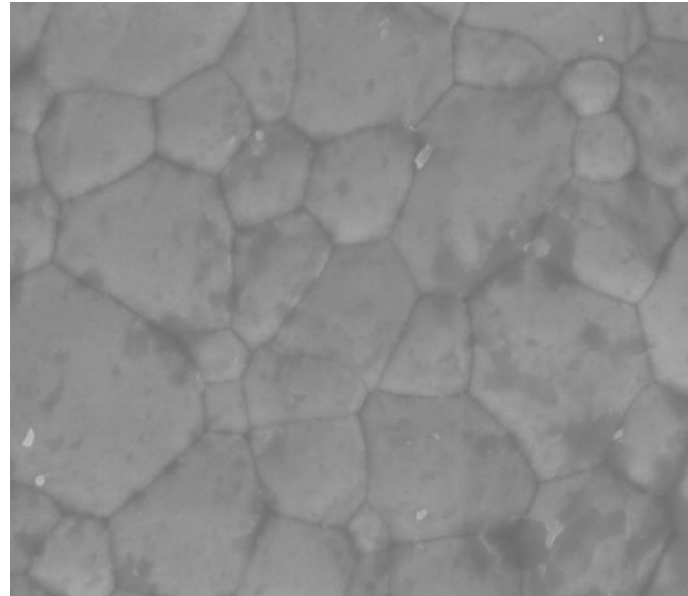(a)

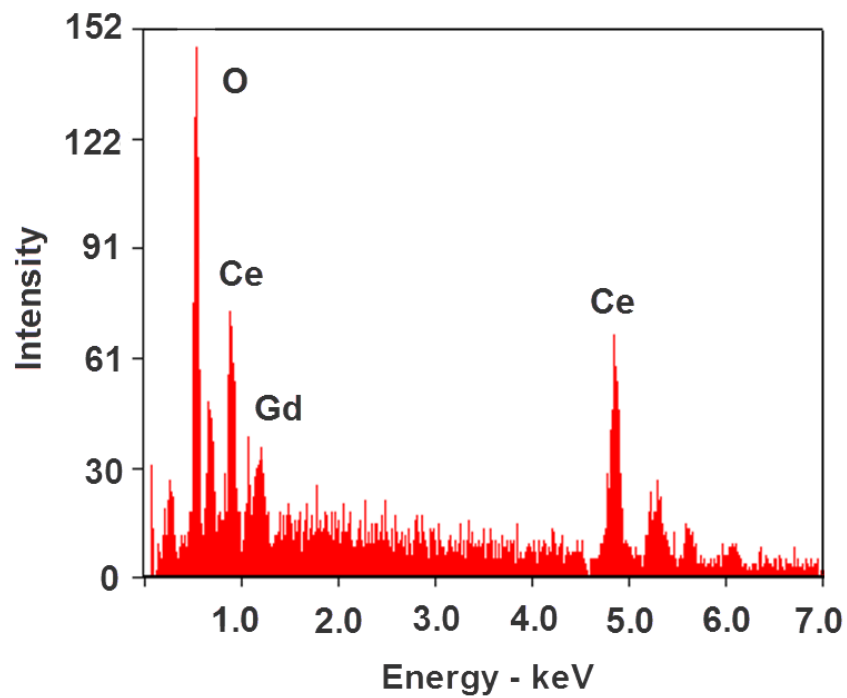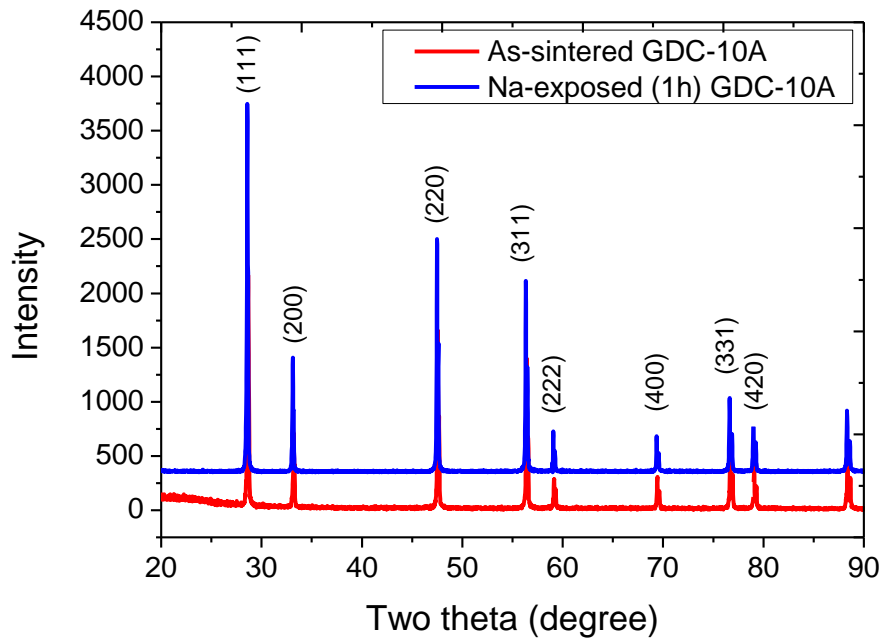

(b)

(c)
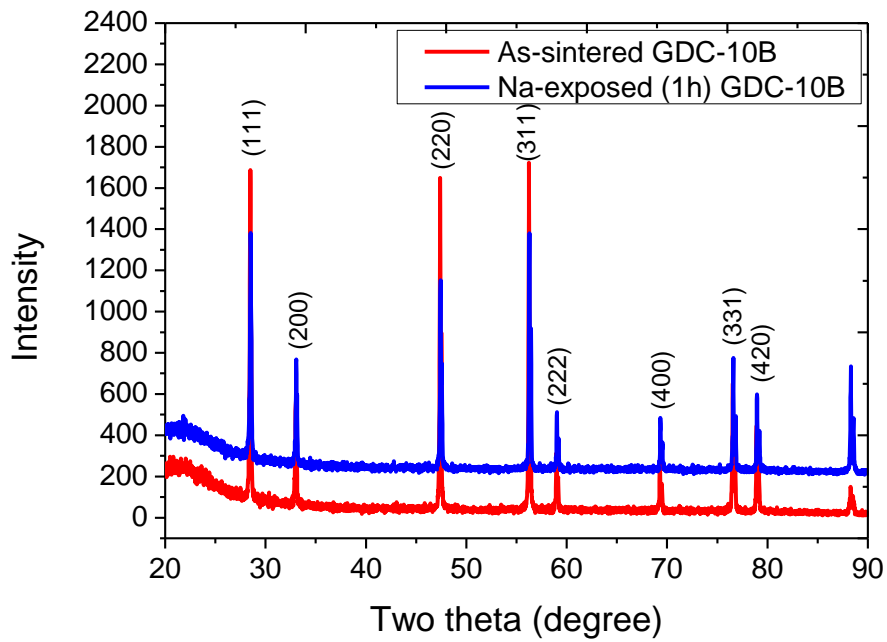

(d)

Figure 4-4. Microstructure of gadolinia-doped ceria (GDC-10A) (SEM image, ×20,000 magnification) after exposure to sodium at 200 °C for 1 h (a); EDS peaks of GDC-10A (b); gadolinia-doped ceria (GDC-10B) (SEM image, ×20,000 magnification) after exposure to sodium at 200 °C for 1 h (c); EDS peaks of GDC-10B (d).

(a)

(b)

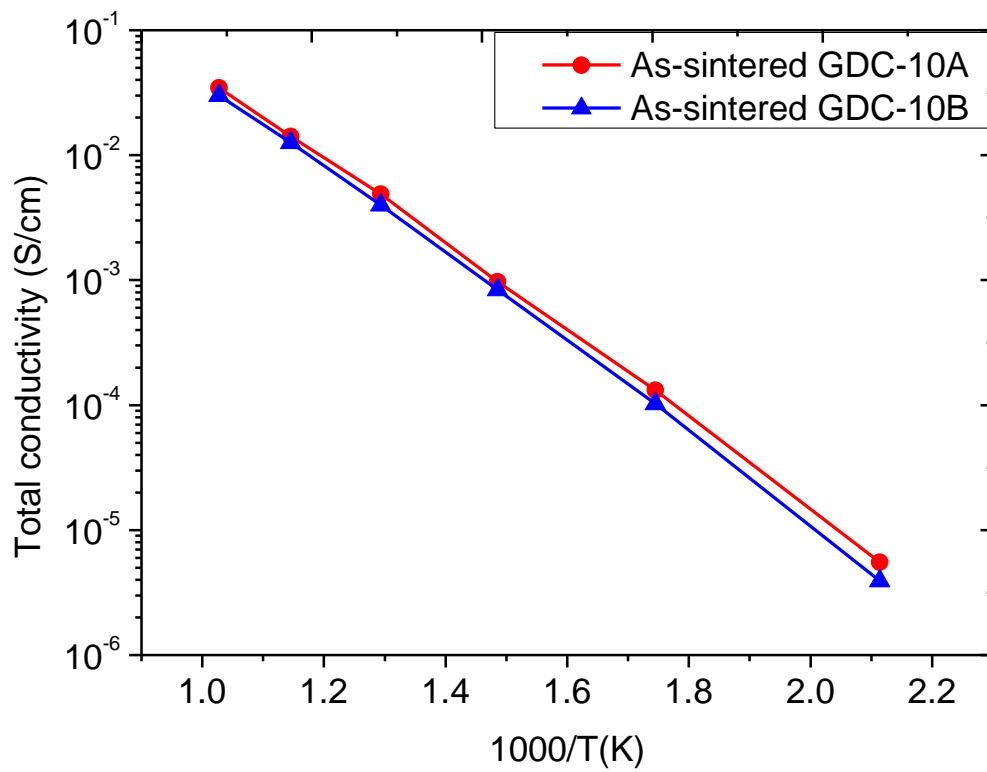**Figure 4-5. XRD spectrum of as-sintered and Na-exposed GDC-10A (a) and as-sintered and Na-exposed GDC-10B (b).**

Figure 4-6. Total electrical conductivity of as-sintered GDC-10A and GDC-B in air atmosphere (p_{O_2} = 21.278 kPa) as a function of temperature.

The presence of $(Ce_{0.9}Gd_{0.1})O_{1.95}$ peaks and the absence of Na-Ce-O compounds such as $NaCeO_2$ and Na_2CeO_3 in the crystals were also confirmed by XRD analysis as shown in Figures 4-5 (a) and 4-5 (b). It is assumed that the ternary compounds were formed and it is not deposited to the surface of the cells.

The total electrical conductivity of as-sintered GDC-10A and GDC-10B was measured in air ($P_{O_2} = 21.278$ kPa) using a four-probe technique. Figure 4-6 shows the variation of the total electrical conductivity as a function of temperature. All samples showed an increase in electrical conductivity with increasing temperature, and the conductivity of the as-sintered GDC-10A sample were slightly higher than that of the as-sintered and GDC-10B sample. At 700 ℃, the total conductivities of the GDC-10A and GDC-10B samples were 0.03465 S/cm and 0.02994 S/cm, respectively, with corresponding values of 5.5136×10^{-6} S/cm and 3.924×10^{-6} S/cm at 200 ℃.

The observed temperature dependence of the total conductivity is in agreement with the theory of conduction in solid electrolytes. Indeed, the electrical transport behavior of fluorite oxide electrolyte is usually represented by the Eq.:

$$\sigma_T = A \exp(\frac{-E_a}{\kappa T})$$

(4-12)

where σ_T is the total conductivity (S/cm), T is the absolute temperature (K), A is a pre-exponential constant (GDC-10 cases: 1.09×10^{-5} at > 400 K and 1.00×10^{-6} at < 400K), k is the Boltzmann constant (8.6173×10^{-5} eV/K), and E_a is the activation energy (eV). The activation energy represents the energy required for the migration of oxygen vacancies, which are the charge carries for oxygen ion transport in this type of electrolyte [21]. Table 4-2 shows the values of the activation energy that were calculated from the slopes in Figure 3-6. Furthermore, similar values for the activation energy were reported by Steele for GDC-10 [23].

The electrical conductivity of polycrystalline materials is significantly influenced by their microstructure, i.e., the grain and grain boundary properties. In many polycrystalline materials, the grain boundaries provide a region of relatively rapid mass transport as compared to the bulk of the crystallites [33]. However, the total conductivity of both GDC-10A and GDC-10B, which have different size of grains, showed almost the same conductivity above 500 ℃. Steele reported that for GDC-10, an intrinsic grain boundary contribution cannot be detected above approximately 500 ℃ [23].

Table 4-2. Activation energy data (E_a) from four-probe d.c. conductivity measurements.

Sample	Temperature range	E_a (eV)
GDC-10A	200-700℃	0.2706
GDC-10B	200-700℃	0.2756

The general reported trends for the effect of grain size on the electrical conductivity for the GDC-10B specimen are as follows. When the grain size exceeds 0.43–0.91 μm, the conductivity decreases with decreasing grain size; this phenomenon can be explained in terms of the space charge model.[34] However, the average grain size of GDC-10A is approximately 0.4 μm, smaller than the range of 0.43–0.91 μm for GDC-10B. In this study, even though the grain size of the GDC-10B specimen is larger than that of the GDC-10A specimen, the total conductivity of the latter is higher.

In oxygen saturated sodium environment at the temperature range of 450-550K, the oxygen partial pressure as shown in Figure 4-2, is 10^{-73} to 10^{-80} atm, corresponding to 1.01396×10^{-65} to 1.01396×10^{-72} kPa, respectively. The total conductivity measurement in this study does not represent the tendency of the electrolytes in liquid sodium environment, however, conductivity at low temperature and grain boundary effect at low temperature are explained.

The potentiometric cells operate at the low temperature for the GDC electrolytes. The emf was measured as a function of temperature with 6 cells (3 cells for GDC-10A and the other for GDC-10B). The variation of emf measured in oxygen saturated sodium with temperature are shown in Figure 4-7. The least-squares fitted expressions for the emf data from each cell as function of temperature are as follow:

$$emf_{theory}(V) = 0.5839 - 2.0044 \times 10^{-4} T (450 - 520K)$$

(4-13a)

$$emf_{GDC-10A} \pm 0.006(V) = 0.71568 - 5.4101 \times 10^{-4} T (450 - 520K)$$

(4-13b)

$$emf_{GDC-10B} \pm 0.005(V) = 0.70548 - 5.301 \times 10^{-4} T (450 - 520K)$$

(4-13c)

where the error quote is the standard deviation of the data from the fitted line.

This test was performed in oxygen saturated sodium. The results show the temperature dependence on emf signal. Since this measurement is conducted in oxygen saturated sodium, emf signal may imply the oxygen saturation condition.

The oxygen concentration in sodium saturated with oxygen (i.e. oxygen solubility in sodium) can be calculated by inserting the measured emf data in oxygen saturated sodium (Eqs. 3-13a and 3-13b) into Eq. 3-8. The correlation of oxygen solubility in sodium as a function of temperature derived from the measured emf data in this study is given by the following expression:

$$\log c_{O,S}(wt.\%)_{theory} = 0.6457 - \frac{1766.5}{T} \quad (450-520K)$$

(4-14a)

$$\log c_{O,S}(wt.\%)_{GDC-10A} = 4.083 - \frac{3094.8}{T} \quad (450-520K)$$

(4-14b)

$$\log c_{O,S}(wt.\%)_{GDC-10B} = 3.973 - \frac{2991.8}{T} \quad (450-520K)$$

(4-14c)

Comparisons of emf signal which is carried out in this study with literature data has been shown in Figure 4-7.

Walters reported the solubility of oxygen in sodium as following expression [35]:

$$\log c_{O,S}(wt.\%) = 0.12 - \frac{1280}{T} \quad (<573K)$$

(4-15)

Bogard and Williams reported the solubility of oxygen in sodium as following expression [36]:

$$\log c_{O,S}(wt.\%) = -0.39 - \frac{890}{T} \quad (<573K)$$

(4-16)

Noden and Bagley reported the solubility of oxygen in sodium as following expression [37]:

$$\log c_{O,S}(wt.\%) = -0.22 - \frac{1043}{T} \quad (<573K)$$

(4-17)

Thorley reported the solubility of oxygen in sodium as following expression [11]:

$$\log c_{O,S}(wt.\%) = 1.12 - \frac{1788}{T} \quad (<573K)$$

(4-18)

Walters, Bogard and Williams reported the solubility of oxygen in sodium as following expression [11]:

$$\log c_{O,S}(wt.\%) = 0.30 - \frac{1290}{T} \quad (<573K)$$
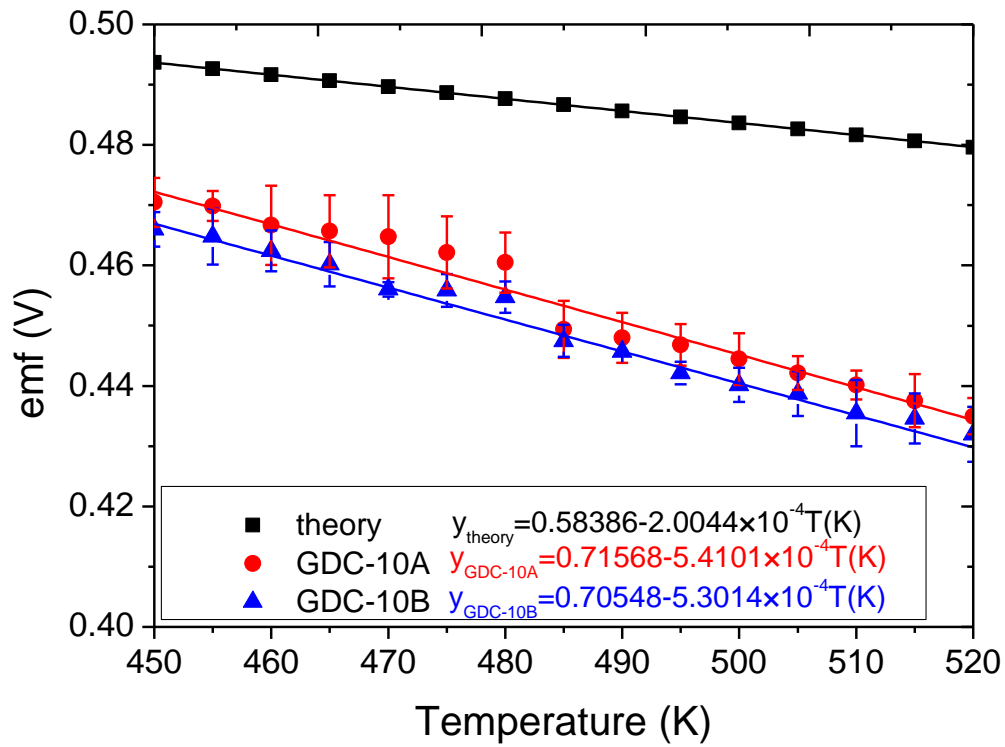
(4-19)

Figure 4-7. The emf signal of theory, GDC-10A and GDC-10B based potentiometric cell as function of temperature.
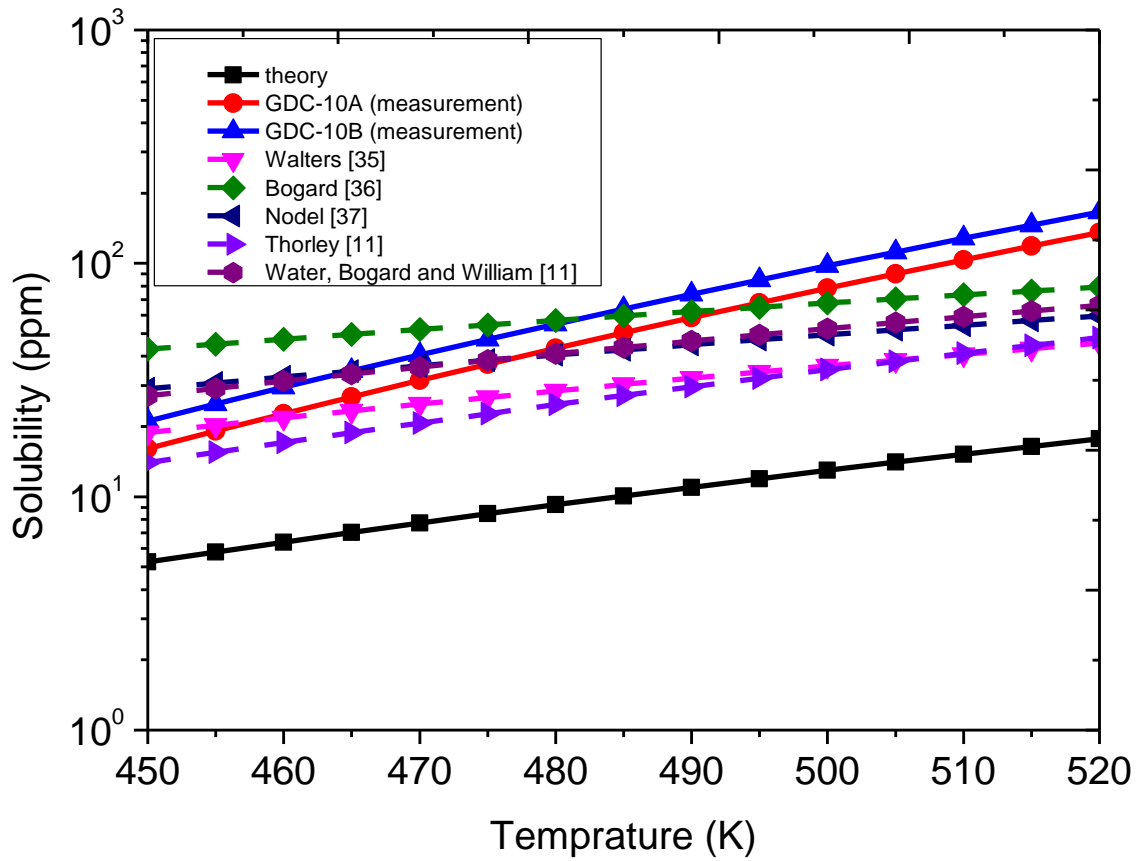
Figure 4-8. Solubility of oxygen in liquid sodium measured by GDC-10A and GDC-10B based potentiometric cells at low temperature.

Solubility graph with the measured data in this study can be fitted as shown in Figure 4-8.

As shown in Figure 4-8, the measurement oxygen solubility in sodium has been compared to other solubility data. It shows that the measured solubility is rapidly increased as temperature increasing. It is believed that the main reason in rapidly increasing solubility as a function of temperature is the mixed ionic-electronic conductivity of solid electrolyte and the mixed ionic-electronic conductivity of GDC solid electrolyte is widely studied [23, 26]. Since the potentiometric cells operate at the low temperature and low oxygen partial pressure such as liquid sodium environment in this study, it requires high oxygen ion conductivity and p-and n-type conductivities as low as possible [38]. Electrical conduction of the electrolyte by only one ion and negligible electronic conductivity (far lower than 1%), equilibrium at both reference and working electrodes and chemical stability of the solid electrolyte are required as potentiometric cell [39]. For the use of GDC in low temperature (450-520K) liquid sodium environment, electrolyte domain should be defined at the oxygen partial pressure between 10^{-73} and 10^{-80} atm, however, limited ranges of the electrolyte domain of GDC were researched [40].

Oxygen ion conductivity can lead to a situation where the electrical conductivity in the solid is essentially ionic within certain range of temperature and oxygen partial pressure. Under these circumstances the ionic transference number, t_i, which represents the ionic contribution to the total conductivity, is unity [3, 41].

The ionic transference number defined as follow:

$$t_i = \frac{emf_{measurement}}{emf_{theory}},$$

(4-20)

where t_i is the ionic transference number, $emf_{measurement}$ is the emf measured from the experiment, and emf_{theory} is the theoretical emf from thermodynamics.

The choice of GDC electrolyte for oxygen measurement in sodium is determined by the boundaries in the candidate materials where contributions from electronic conduction (n or p type) become sufficiently larger than that t_i becomes less then unity.

In this study, GDC solid electrolyte shows n-type electrical properties in oxygen saturated sodium environment since the electrolytes were in reducing condition in sodium environment with the formation of ternary compounds ($NaCeO_2$ and Na_2CeO_3) and the lower oxygen partial pressure   limit is caused by reduction of the electrolyte material, generating n-conductivity [42].

For use of the GDC based potentiometric cell in the SFR application, it should be set at oxygen controlled Na by cold-trap where dissolved oxygen is lower than the oxygen concentration threshold for the compounds ($NaCeO_2$ and Na_2CeO_3) at temperatures.

4. 4 Conclusions

In order to use an potentiometric cell that is functional in liquid sodium at low temperature, the oxide-based electrolytes, gadolinia-doped ceria (GDC-10A and GDC-B), were evaluated as candidate materials due to their known oxygen ion conductivity. Thermochemical stability, conductivity measurements, and emf measurement tests were conducted for these solid electrolytes. The thermochemical stability tests for the GDC-10 (A and B) demonstrated defected surface following exposure to liquid sodium at 200 ℃ for a certain period of time. While exposure to Na, ceria is easily react with sodium or sodium oxide to form ternary oxides such as $NaCeO_2$ and Na_2CeO_3. It is assumed that the ternary compounds were formed and it is not deposited to the surface of the cells. Conductivity measurements as a function of temperature demonstrated the slightly higher conductivity of the GDC-10 A specimens relative to the GDC-10B. The calculated solubility at 450–520K data show higher gradient at the test temperature and it is believed that the behavior is caused by n-type electrical properties in oxygen saturated sodium environment since the electrolytes were in reducing condition in sodium environment with the formation of ternary compounds ($NaCeO_2$ and Na_2CeO_3) and the lower oxygen partial pressure limit.

4. 5 Reference

1. M.R. Hodbell and C.A. Smith, J. Nucl. Mater., 110 (1982) 125.

2. T. Furukawa, S. Kato and E. Yoshida, J. Nucl. Mater., 392 (2009) 249.V. Ganesan and V. Ganesan, J. Nucl. Mater., 256 (1998) 69.

3. V. Ganesan and V. Ganesan, J. Nucl. Mater., 392 (2009) 249.

4. S.R. Pillai, H.S. Khatak and J.B. Gnanamoorthy, J. Nucl. Mater., 224 (1995) 17.

5. T. Gnanasekaran and C.K. Mathews, J. Nucl. Mater., 140 (1986) 202.

6. D.R. Olander, Fundamental Aspects of Nuclear Reactor Fuel Elements, US Dept. of Energy (1976).

7. J. Guidez, in: J. Guidez (Ed.), Phenix: The Experience Feedback, EDP Science, CEA (2013).

8. R.G. Taylor and R. Thompson, J. Nucl. Mater., 115 (1983) 25.

9. E. Yoshida and S. Kato, J. Nucl. Mater., 329-333 (2004) 1393.

10. D.W. Sandusky, J.S. Armijo and W.J. Wagner, J. Nucl. Mater., 46 (1973) 225.

11. K.T. Claxton, J. Nucl. Energy. Parts. A/B., 19 (1965) 849.

12. L.P. Pepkowitz and W.C. Judd, Analyst. Chem., 22 (1950) 1283.

13. D.D. Williams and R.R. Miller, Analyst. Chem., 23 (1951) 1865.

14. L.P. Pepkowitz, W.C. Judd and R.J. Downer, Analyst. Chem., 26 (1954) 246.

15. H. Beisswenger and S. Dorner, J. Nucl. Mater., 28 (1968) 297.

16. J.R. Humphreys, Amer. Inst. Chem. Engrs. Nucl. Engng. Sci., 53 (1957) 7.

17. T.H. Estell and S.N. Flengas, Chem. Rev., 70 (1970) 339.

18. J. Konys, H. Muscher, Z. Vo and O. Wedemeyer, J. Nucl. Mater., 296 (2001) 289.

19. H.U. Borgstedt and C.K. Mathews, Applied Chemistry of Alkali Metals, Plenum Press, New York (1987), ISBN 0-306-42326-X.

20. J. Konys, H. Muscher, Z. Vo and O. Wedemeyer, J. Nucl. Mater., 335 (2004) 249.

21. C. Schroer, J. Konys, A. Verdaguer, J. Abella`, A. Gessi, A. Kobzova, S. Babayan and J.-L. Courouau, J. Nucl. Mater., 415 (2011) 338.

22. A. Mariën, J. Lim, K. Rosseel, W. Vandermeulen, J. Van den Bosch, J. Nucl. Mater., 427 (2012) 39.

23. B.C.H. Steele, Solid State Ionics, 129 (2000) 98.

24. J.E. Bauerle, J. Chem. Phys., 45 (1966) 4162.

25. X.J. Chen, K.A. Khor, S.H. Chan and L.G. Yu, Mater. Sci. Eng. A-Struct., 335 (2002) 246.

26. H. Inaba and H. Tagawa, Solid State Ionics, 83 (1996) 1.

27. R.V. Mangalaraja, S. Ananthakumar, M. Paulraj, K. Uma, M. Lopez, C.P. Camurri and R.E. Avila, Process. Appl. Ceram., 3 (2009) 137.

28. K. Yasuda, K. Uemura and T. Shiota, J. Phys.: Conf. Ser., 339 (2012) 012006.

29. K. Natesan, J. Nucl. Mater., 115 (1983) 251.

30. K.T. Claxton, J. Nucl. Energ., 21 (1967) 351.

31. M.G. Baker, S.A. Frankham, P.G. Gadd. J. Nucl. Mater., 218 (1995) 256.

32. M.A. Mignanelli, P.E. Potter and M.G. Barker, J. Nucl. Mater., 97 (1981) 213.

33. S. Hui, J. Roller, S. Yick, X. Zhang, C. Deces-Petit, Y. Xie, R. Maric and D. Ghosh, J. Power Source, 172 (2007) 493.

34. A. Tschope, Solid State Ionics, 139 (2001) 267.

35. S.L. Walters, Report NP.1955 (MSA-TR-VI) (1955).

36. A.D. Bogard and D.D. Williams, Report NRL-3865 (1951).

37. J.D. Noden and K.Q. Bagley, UKAEA Report R & DB(C)-TN-80 (1954).

38. H. Ullmann and K. Teske, Sensor. Actuat. B., 4 (1991) 417.

39. J. Fouletier and V. Ghetta, Materials Issues for Generation IV System, Springer Science, NATO, (2008).

40. T. Kudo and H. Obayashi, J. Electrochem. Soc., 123 (1976) 415.

41. F.A. Kozlov, E.K. Kuznetsov, T.A. Vorob'eva, Kh. Ul'mann, T. Reetts and V. Rikhter, Soviet Atomic Energy, 51 (1981) 516.

42. H. Ullmann and K. Teske, Sensor. Actuat. B., 4 (1991) 417.

V. CARBON MEASUREMENT

5. 1 Introduction

In the primary and secondary heat transport system in sodium-cooled reactors, nonmetallic elements, such as carbon, oxygen, and nitrogen, in sodium have a large effect on corrosion rates and the mechanical behavior of materials. In the Natesan's work [1], the general requirements of a material for this application were reviewed and α-iron meets the requirement. Moreover, the equilibrium method using austenitic steels such as Fe-8wt% Ni, Fe-16wt%Ni, and Fe-18wt%Cr-8wt%Ni were used in flowing sodium at 750℃ due to long equilibration time in lower sodium temperature. To accurately measure carbon activity in liquid sodium, many authors have contributed their work [1-3] using austenitic steel. Depending on the SFR design, the peak cladding temperature is around 550-650℃ in which the temperature is lower than that in previous equilibration study. In this study, α-iron foil equilibrium method for the accurate measurement of carbon activities in static liquid sodium at 550℃ is presented.

5.2 Experimental

The chemical composition of the austenitic 304 stainless steel and α-iron foils are listed in Table I. Austenitic 304 stainless steel (SS) and α-iron foils were supplied from R.O.Foil (99.5% purity, 0.01mm thick) and Alfa Aesar (99.5% purity, 0.0254mm thick), respectively. The equilibration time for the 0.01mm thick of austenitic 304 SS and 0.025mm thick of α-iron foils in static liquid sodium at 550℃ was extrapolated from Natesan's work [1]. The calculated equilibration time for the foils is listed in Table II in where t is the equilibration time (h) and T is the temperature (K). The equilibration test of each foil is carried out for 300 h in 316L stainless steel cell containing 0.5kg of liquid sodium at 550℃ in which is shown in Figure 5-1. Liquid sodium is static and contact with 316L stainless steel cell. The sodium temperature is controlled by using K-type thermocouple for temperature feedback with heater controller. The foil samples are hanged on the specimen holder made of also 316L SS. Since the carbon activity calculation using the correlations based on the iron-chromium-nickel alloy in the literatures [1-3] is well developed, it is used as a reference sample in our study. So carbon concentration in the sodium is not controlled in this study. Depending on the SFR design, the peak cladding temperature is around 550-650℃ in which the temperature is lower than that in previous equilibration study [1]. In this study, α-iron foil equilibrium method for the accurate measurement of carbon activities in static liquid sodium at 550℃ is presented.

Table 5-1. Chemical composition of austenitic 304 stainless steel and α-iron foils (wt%).

Foil type	C	Si	Mn	P	S	Ni	Cr	Mo	Fe
304 SS	0.041	0.37	1.66	0.023	0.003	9.2	18.23	-	Bal.
α-iron	< 0.08	< 0.1	< 0.3	< 0.04	< 0.05	-	-	-	Bal.

Table 5-2. Equilibration time at 550°C for carbon in foil samples of austenitic 304 stainless steel and α-iron extrapolated data from Natesan's work [1].

Foil type	304 SS	α-iron
Thickness	0.0254mm	0.0508mm
Equation for extrapolation (h)	$t = 2 \times 10^{-6} \exp \dfrac{15971}{T(K)}$	$t = 2 \times 10^{-8} \exp \dfrac{17998}{T(K)}$
Calculated equilibration time	~ 535 h	~ 32 h
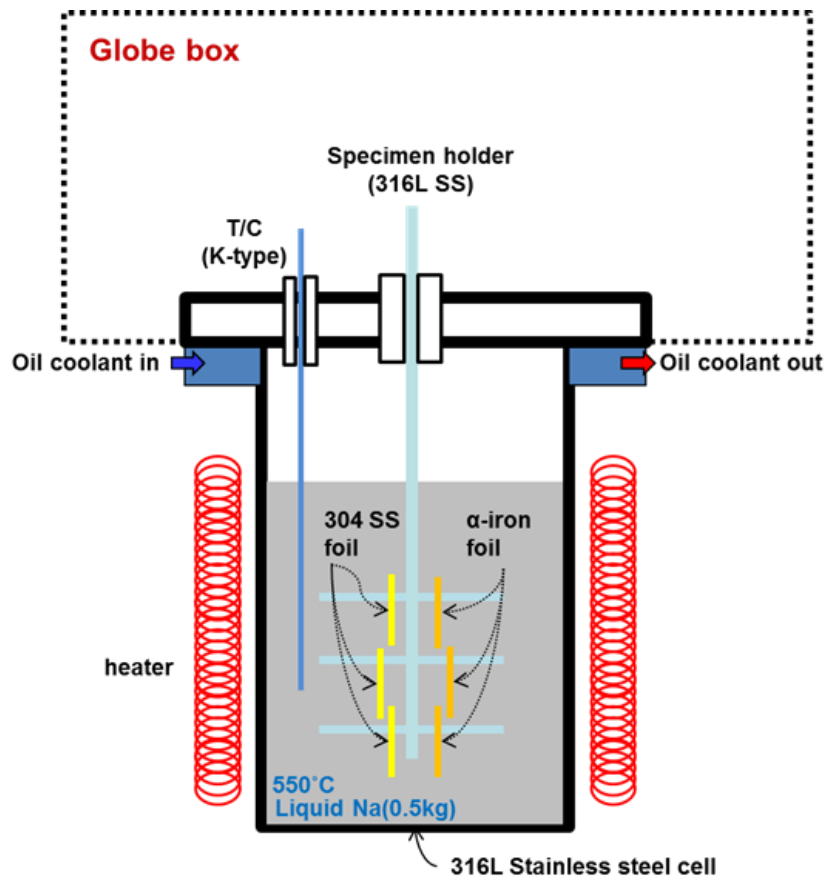
Figure 5-1. Schematic illustration of experimental system.

After equilibration in liquid sodium, the foil samples are removed from the cell, the foil samples are cleaned in ethanol for 1 hour and ultrasonically washed in DI-water for 1 hour to remove adherents at the surface. Then, the foil samples were analyzed for carbon using a LECO carbon combustion analyzer (CS 600) that had two different levels of sensitivity for 304 SS and α-iron. Also using focused ion beam (FIB), foil samples are fabricated for transmission electron microscopy (TEM) analysis on precipitates.

5.3 Methodology

When both types of foil samples and liquid sodium are allowed to reach equilibrium with respect to carbon transfer, the chemical potentials of carbon become equal [1]. The carbon potentials of sodium and the foil samples are given as follows:

$$\mu_C^{Na} = \mu_C^0 + RT \ln \alpha_C^{Na},$$
(5-1)

$$\mu_C^{foil} = \mu_C^0 + RT \ln \alpha_C^{foil},$$
(5-2)

where μ_C^{Na} and μ_C^{foil} is the chemical potential of carbon in sodium and the foil, respectively, α_C^{Na} and α_C^{foil} is the activities of carbon in sodium and the foil, respectively, μ_C^0 is the chemical potential of carbon in the chosen standard state, R and T is the gas constant and the absolute temperature.

Under the conditions of equilibrium,

$$\mu_C^{Na} = \mu_C^{foil}.$$
(5-3)

Graphite is normally chosen as the standard state and assigned a carbon potential value of zero at all temperatures. Hence, at equilibrium,

$$\alpha_C^{Na} = \alpha_C^{foil}.$$
(5-4)

The equilibration time for 304 SS and α-iron foil samples stated in Table 5-2 is 535 h and 32 h when their thickness is 0.0254 mm and 0.0508 mm, respectively. In this study, the thickness of each

foil is 0.01mm and 0.0254mm which are thinner than that listed in Table 5-2, so the equilibration time at 550℃ must be shorter than that 535h and 32h, respectively.

The results for the solubility of carbon in 304 SS and α-iron at temperatures are listed in Table 5-4. Solubility data of carbon in each material at 550℃ is listed.

The carbon activity as a function of carbon concentration for 304 SS is more complicated than that for α-iron. In the literatures [1-3], the correlations for the carbon activity in equilibrated austenitic iron-chromium-nickel alloy foil sample were well developed as follow:

$$
\begin{aligned}
\ln \alpha_C &= \ln((0.048)\% C) + (0.525 - \frac{300}{T})\% C \\
&- 1.845 + \frac{5100}{T} - (0.021 + \frac{72.4}{T})\% Ni \\
&+ (0.248 - \frac{404}{T})\% Cr \\
&- (0.0102 - \frac{9.422}{T})\% Cr^2,
\end{aligned}
$$

(5-5)

$$
\begin{aligned}
\log \alpha_C &= \frac{2105}{T} - 0.6735 - (-3.0 + \frac{8700}{T}) N_{Cr} \\
&+ (0.565 + \frac{1520}{T}) N_{Ni} + \log N_C,
\end{aligned}
$$

(5-6)

$$
\begin{aligned}
\ln \alpha_C &= \ln((0.048)\% C) + (0.525 - \frac{300}{T})\% C \\
&- 1.845 + \frac{5100}{T} \\
&- (0.021 - \frac{72.4}{T})\% (Ni + Mn) \\
&+ (0.248 - \frac{404}{T})\% Cr \\
&+ (0.0102 - \frac{9.422}{T})\% Cr^2 + 0.033\% Cr,
\end{aligned}
$$

(5-7)

where T is the absolute temperature. N_{Cr}, N_{Ni}, and N_C, in Eq. 5-6 are the atom fractions of chromium, nickel, and carbon in the sample.

Eq. 5-7 is based on the Eq. 5-5 which is developed by Natesan's previous work [7], to more accuracy measurement of carbon activity by considering additional terms.

For the carbon activity measurement as a function of carbon concentration for α-iron, the new correlation based on Fe-C binary system at 550℃.

Table 5-3. Result of carbon concentration measurement in foil samples after equilibration in static liquid sodium at 550°C.

Foil type	Mass of foil samples (g)	C content on foil sample (wt%)	C atomic fraction
304 SS	0.4161	0.243	0.01106
	0.3738	0.246	0.01119
	0.4258	0.251	0.01142
	0.4313	0.246	0.01119
	0.5883	0.238	0.01083
	0.5523	0.238	0.01083
α-iron	0.3459	0.00126	0.00006
	0.3654	0.00110	0.00005
	0.3427	0.00114	0.00005
	0.3661	0.00140	0.00006

Table 5-4. Solubility of carbon in 304 stainless steel and α-iron [4-6].

Temperature (℃)	304 SS (wt%)	α-iron (wt%)
550	-	0.0013
727	-	0.022
871	0.0066	-
927	0.035	-
1079	0.077	-
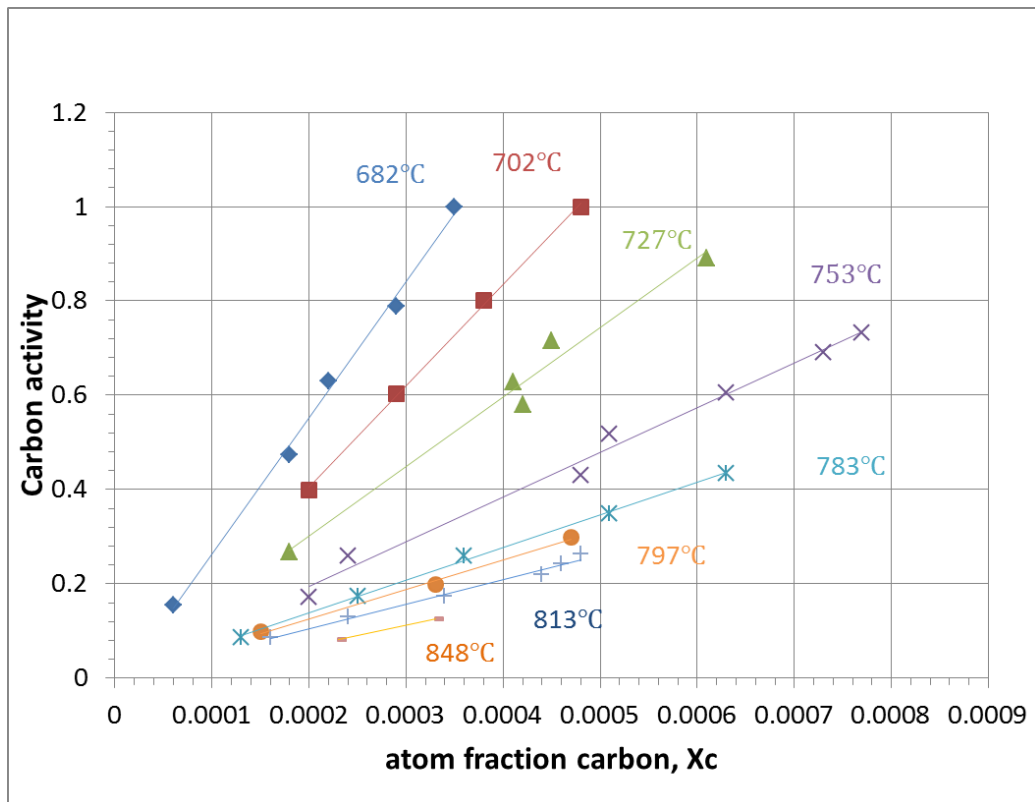
Figure 5-2. The activity of carbon in Fe-C ferrite system as a function of carbon concentration.
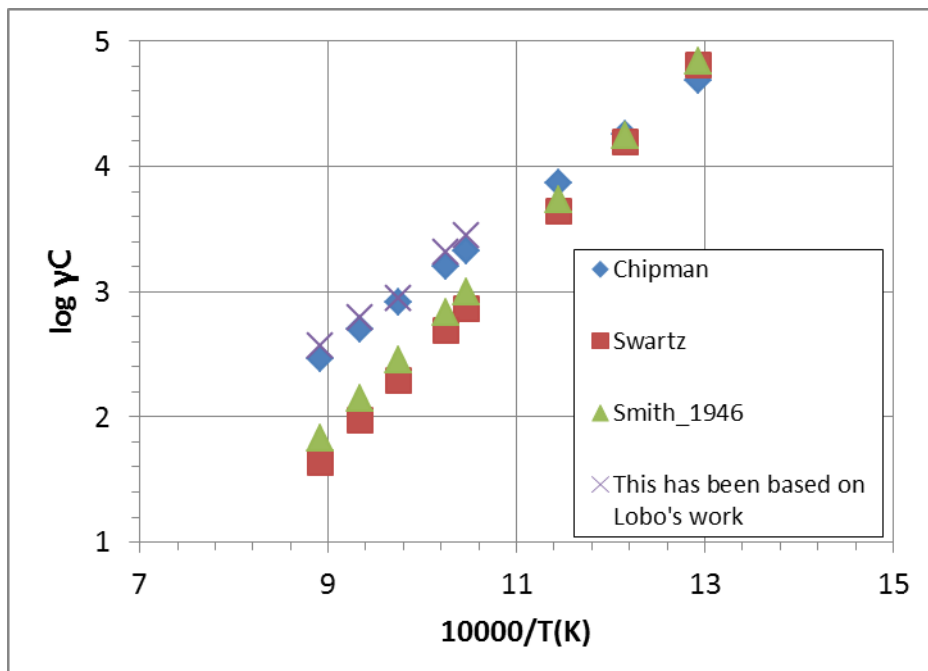
Figure 5-3. Activity coefficient of carbon in Fe-C ferrite system as a function of reciprocal temperature obtained from the results of different investigators.

Since carbon activity is defined as follow:

$$\ln \alpha_C = \ln \gamma_C + \ln N_C,$$
(5-8)

where γ_C is the activity coefficient of carbon in the sample.

To define the carbon activity coefficient of carbon in the α-iron in this study, the results of different investigators [8-13] for the variation of the activity coefficient of carbon in ferrite with carbon concentration in the Fe-C binary system are shown in Figure 5-2 and Figure 5-3.

Figure 5-2 is reproduced from Lobo's work [8] and shows carbon activity of carbon in Fe-C ferrite as a function of carbon concentration at different temperatures. To calculate activity coefficient of carbon, the carbon activity is divided by carbon atom fraction, and the summarized data is listed in Table 5-5. In the Table, the activity coefficient of carbon, $\log \gamma_C$, is at each temperature is shown to be almost constant. So the carbon activity data is compared to other data obtained from different investigators [9-13] in the Figure 5-3. Based on Smith and Swartz's data, Chipman have made a correlation of the activity coefficient of carbon as a function of a reciprocal temperature as follow:

$$\log \gamma_C = \frac{5550}{T} - 2.49$$
(5-9)

Lobo's data show similar value with other data in the Figure 5-3 and using that new correlation is obtained from Figure 5-3 as follow:

$$\log \gamma_C = \frac{5672}{T} - 2.52$$
(5-10)

Activity coefficient of carbon in Fe-C ferrite system as a function of reciprocal temperature obtained from the results of different investigators.

The average values of Eqs. 5-9 and 5-10 is as follow:

$$\log \gamma_C = \frac{5611}{T} - 2.505$$
(5-11)

Table 5-5. Carbon activity coefficient in equilibrated Fe-C ferrite [8].

Temperature (°C)	atom fraction	α_C	$\log \gamma_C$
682	0.00006	0.158	3.42
	0.00018	0.473	3.42
	0.00022	0.63	3.46
	0.00028	0.788	3.45
	0.00034	1	3.47
702	0.0002	0.4	3.30
	0.00029	0.6	3.32
	0.00038	0.8	3.322
	0.00047	1	3.33
727	0.00018	0.268	3.17
	0.00042	0.58	3.14
	0.00041	0.625	3.18
	0.00046	0.714	3.19
	0.00061	0.892	3.17
753	0.0002	0.172	2.93
	0.00024	0.259	3.03
	0.00048	0.431	2.95
	0.00051	0.517	3.01
	0.00063	0.603	2.98
	0.00072	0.689	2.98
	0.00076	0.732	2.98
783	0.00013	0.087	2.83
	0.00023	0.174	2.88
	0.00037	0.261	2.85
	0.00051	0.348	2.83
	0.00064	0.434	2.83
797	0.00015	0.1	2.82
	0.00033	0.2	2.78
	0.00048	0.3	2.80
813	0.00017	0.088	2.71
	0.00025	0.131	2.72
	0.00033	0.175	2.72
	0.00044	0.219	2.70
	0.00046	0.244	2.72
	0.00046	0.263	2.76
848	0.00023	0.084	2.56
	0.00033	0.127	2.58

* α_C is the activity of carbon.

* $\log \gamma_C$ is the activity coefficient of carbon.
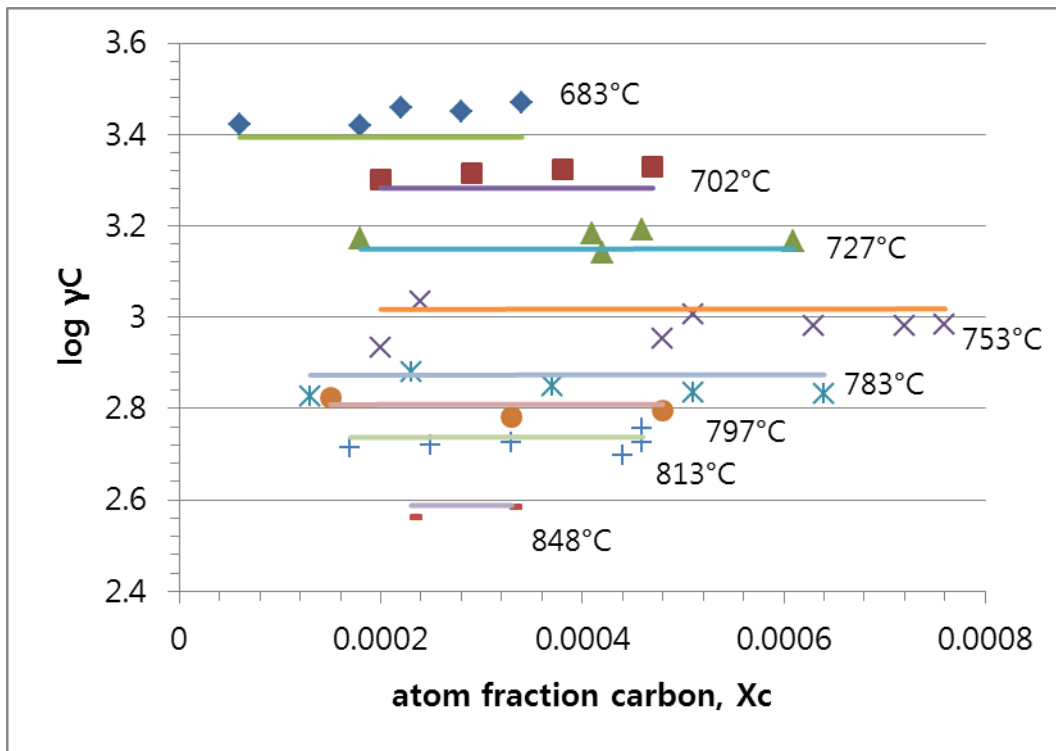
Figure 5-4. The activity coefficient of carbon in Fe-C ferrite as a function of carbon concentration.
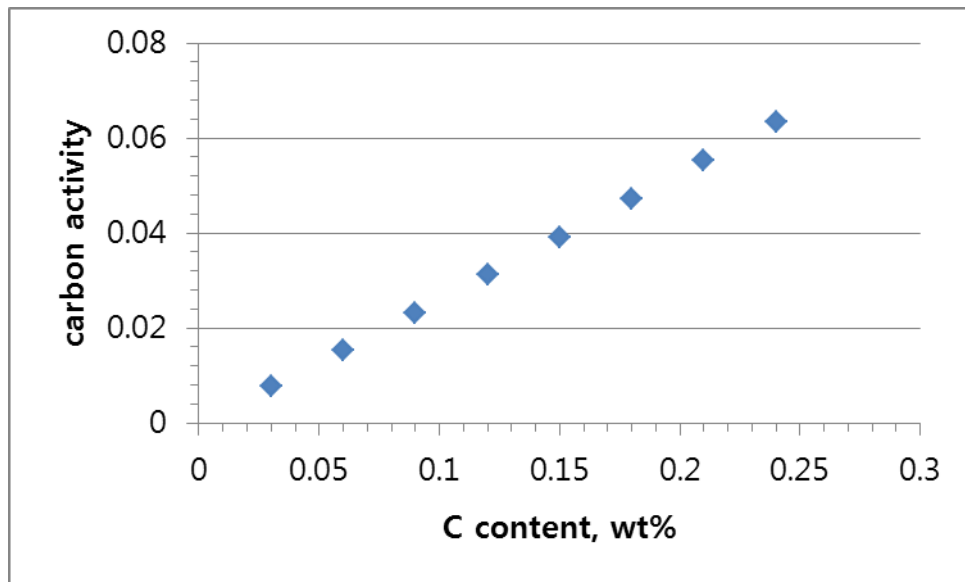
(a)
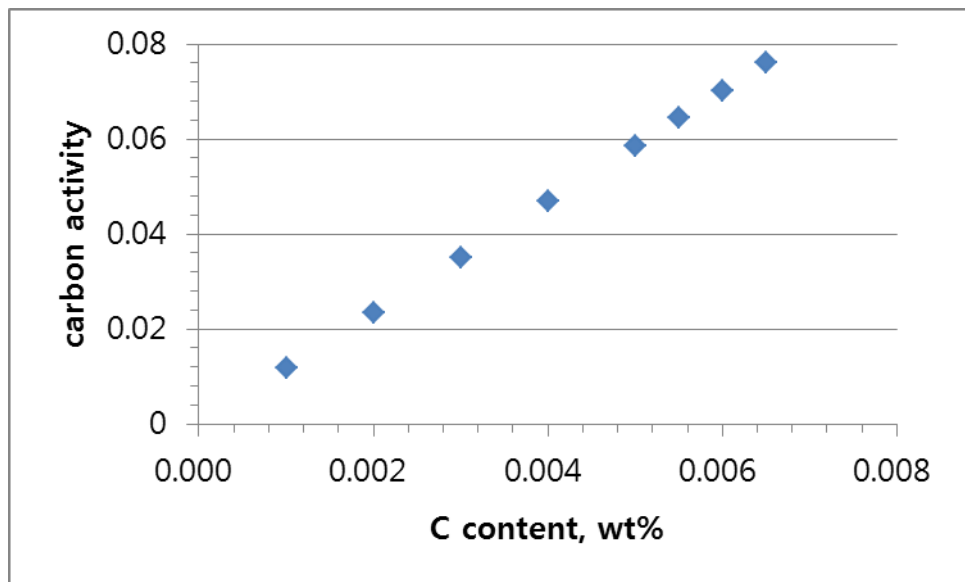
(b)

Figure 5-5. Carbon activity calculation as function of carbon concentration at 550°C using chemical composition of (a) 304 SS and (b) α-iron.
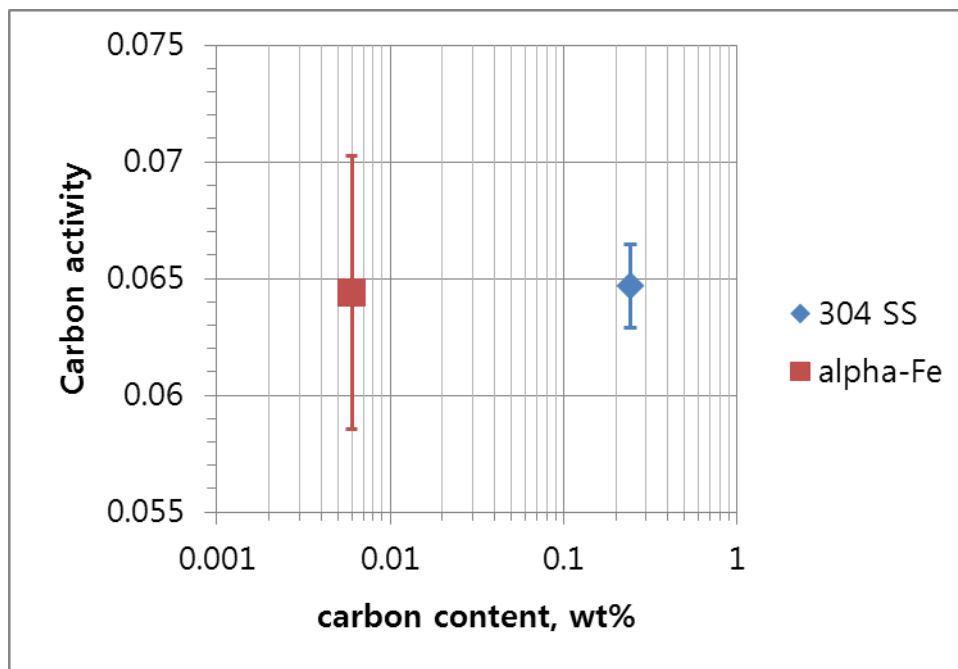
Figure 5-6. Carbon activity calculated in 304 SS and α-iron based on equilibrated carbon concentration.

Since the activity coefficient of carbon is a constant at a temperature, Eq. 5-7 is used as reference for the calculation of carbon activity of samples which were equilibrated in static liquid sodium at 550℃.

At the Eq. 5-1, the first five terms of right hand is defined from the activity coefficient of carbon in Fe-C austenitic as a function of carbon concentration. For the Fe-C ferrite system to calculate carbon activity in liquid sodium in this study, new term to determine carbon activity is defined as follow:

$$
\log \gamma_C = \log(\frac{10}{1-N_C}) + (1.2 - \frac{1.35}{T})(\frac{N_C}{1-N_C}) \\
-4.25 + \frac{5200}{T}.
$$
(5-12)

Based on the Eq. 5-12, this correlation is plotted in Figure 5-4 and compared to the Lobo's data which was proved to have similar data with other investigators' data [9-12].

Eq. 5-11 shows carbon activity coefficient is as a function of temperature, however, Eq. 5-12 shows carbon activity coefficient of carbon as function of carbon concentration at temperatures.

Since the relation in Eq. 5-8, the carbon activity is calculated as follow:

$$
\log \alpha_C = \log(\frac{10N_C}{1-N_C}) + (1.2 - \frac{1.35}{T})(\frac{N_C}{1-N_C}) \\
-4.25 + \frac{5200}{T}.
$$
(5-13)

5.4 Results and Discussion

The carbon activity calculation using Eqs. 5-7 and 5-13 as function of carbon concentration is shown in Figure 5-5 (a) and (b), respectively. Since 304 SS foil sample is used to calculate a reference carbon activity to compare to carbon activity in α-iron in this study, chemical composition of the sample is used to calculate Eq. 5-7. Also the carbon activity calculation for α-iron using Eq. 5-13 is shown in Figure 5-5 (b).

To compare carbon activity in α-iron foil samples to carbon activity in 304 SS, Figure 5-6 show the carbon activity calculated in both type of foil samples. Based on the carbon concentration in the foil samples which were equilibrated in static liquid sodium at 550℃ for 300h as listed in Table 5-3, the carbon activity is calculated. Figure 5-6 shows that the average values of carbon activity in 304 SS and α-iron foil samples are 0.0647 and 0.0644, respectively

Even though the carbon concentration in both 304 SS samples is two orders higher than that in α-iron foil samples, the calculated average carbon activity in both types of samples shows similar values as shown in Figure 5-6.

(a)

Fe$_3$C →

20 nm
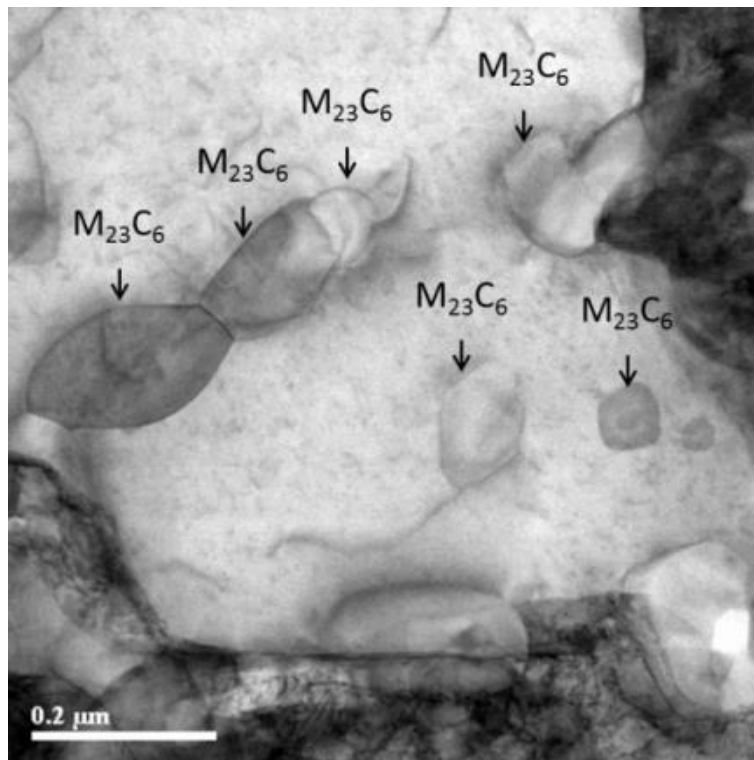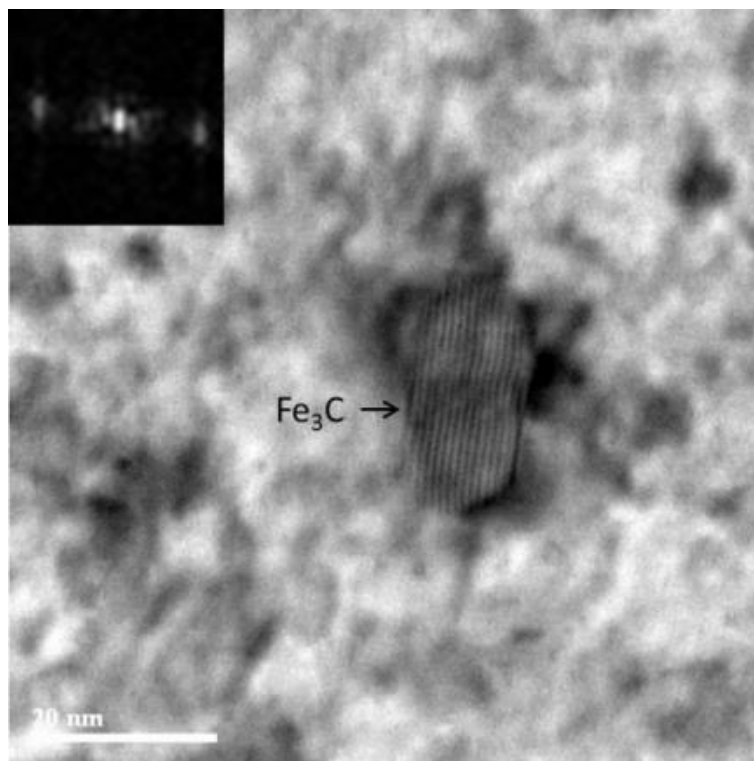
(b)
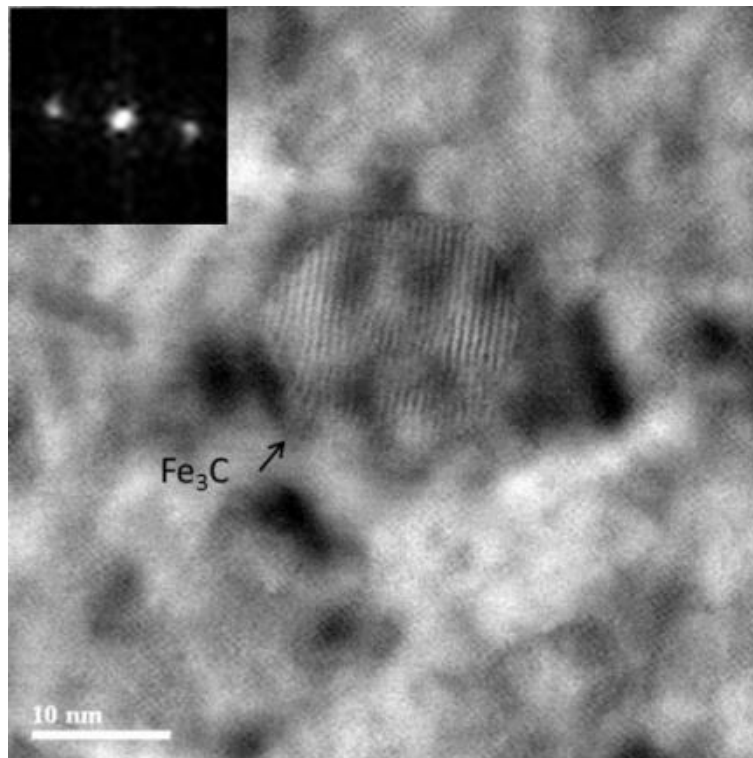
(c)

Figure 5-7. BF-STEM image of austenitic 304 SS foil sample (a), BF-STEM images of α-iron foil sample (b) and (c), both 304 SS and α-iron foil samples were equilibrated in static liquid sodium at 550°C for 300 h and fabricated by focused ion beam (FIB). (*Additional TEM analysises are in Appendix C.)

The results for the α-iron are particularly useful for determining the carbon activity in sodium at 550℃, because the equilibration time is quite shorter compared to 304 SS and sodium temperature in SFR is closed to between 550-650℃ where ferrite phase is stable [6].

Since austenitic 304 SS and α-iron foil samples contains few hundreds ppm of impurities, the carbide forming effect of impurities should be considered. Carbides former impurities such as Ti, Zr, Nb, V, and Ta are not contained in both foil samples, only $M_{23}C_6$ carbide in 304 SS and Fe_3C carbide in α-iron foil samples are observed by TEM analysis as shown in Figure 5-7. The Cr carbide term is considered as last term in right hand of Eq. 5-7, also Eq. 5-13 also need an additional terms to consider Fe_3C formation which can modify the carbon activity for further work.

5.5 Conclusions

For measurement of carbon activity in liquid sodium, α-iron foil samples which were equilibrated in static sodium at 550℃ for 300h, have shown closed value of the carbon activity calculated   in 304 SS foil samples which were also equilibrated in the same environment. Since 304 SS foil sample works as a role of reference carbon activity,

Developed relationship of carbon activity and carbon concentration in ferrite iron, as Eq. 5-13, can be used to determine carbon activity of liquid sodium.

5.5 Reference

1. K. Natesan and T. F. Kassner, Nucl. Technol., 19 (1973) 46.

2. S. R. Pillai and C. K. Mathews, J. Nucl. Mater., 150 (1987) 31.

3. V. H. Tuma, P. Groebner and K. Loebl, Archiv. Eisenhuttenw., 9 (1969) 727.

4. S. J. Rosenberg and C. R. Irish, J. Res. Nat. Bur. Stand., 48 (1952) 2281.

5. W. D. Callister and D. G. Rethwisch, Fundamentals of Materials Science and Engineering, Ch. 10, John Wiley & Son, Singapore (2008).

6. J. Chipman, Metall. Trans., 3 (1972) 55.

7. K. Natesan and T. F. Kassner, Metall. Trans., 4 (1973) 2557.

8. J. A. Lobo and G. H. Geiger, Metall. Trans. A., 7A (1976) 1347.

9. R. P. Smith, J. Am. Chem. Soc., 68 (1946) 1163.

10. R. P. Smith, Trans. TMS-AIME., 224 (1962) 105.

11. J. C. Swartz, Trans. TMS-AIME., 239 (1967) 68.

12. J. C. Swartz, Trans. TMS-AIME., 245 (1969) 1083.

13. T. Hejnal, Czech. J. Phys. B., 32 (1982) 1126.

VI. SODIUM CORROSION MODEL

6. 1 Introduction

This chapter focused on sodium corrosion model. Previous developed sodium corrosion model is empirical based on their experimental results. Sodium corrosion is dependent on impurities (oxygen, carbon, and nitrogen) concentration, temperature, velocity, and alloying element, the tendency of effect was well known from the literatures.

Brush [1] and Zhang et al. [2, 3] have been developed fundamental corrosion models by theoretical methods to analysis corrosion behavior of material in sodium environment. The theoretical analysis based on the literature, Zhang [2] have mentioned that the oxidation effect on corrosion rate of material is not considered and dissolution of iron into sodium is controlled by oxygen concentration. However, literature [4-10] show that the surface, internal or intergranular oxidation during their experimental results. Depending on oxygen concentration in liquid sodium, the oxidation process is differed. In recent study [8], austenitic stainless steel was exposed to liquid 923 K liquid sodium containing 200 μg/g of dissolved oxygen and intergranular oxidation was observed.

Thorley et al. [9] have reported the formation of a ferritic layer in a 316 SS specimen exposed to sodium at 848 K. These authors have reported the formation of $NaCrO_2$ in a loop with sodium containing 10 ppm oxygen at regions away fro mthe high temperature zone in the downstream and upstream zone. Even though the formation of $NaCrO_2$ in the sodium/steel system has been established beyond doubt, there is considerable discrepancy between theoretically calculated values and that experimentally measured on the threshold oxygen for its formation. In the literature [10], the attempt is to calculate the threshold oxygen level when sodium is in contact with austentici stainless steel (AISI 304 SS, 316 SS, D9 alloys) and ferritic/martensitic steel (Fe-9Cr-1Mo and Fe-2.25Cr-1Mo alloys) using a new expression on the Gibbs energy of formation of $NaCrO_2$. That new expression has been obtained by regression analysis of different reliable measurements reported in the literature [11-17] and summariezed in Table 6-1.

Based on corrosion behavior at the surface of the steels, two different corrosion models are suggested in thie thesis due to its different corrosion mechanism.

The first case is cotrolled only dissolution process at the surface of material. In Ganesan's work [18], 304 SS specimen was exposed flowing sodium containing 1-2 ppm oxygen at 823 K for 60,000 h and at 873 K for 20,000 h. After exposure, at the cross section of the specimen, depleted layer by the depletion of nickel and manganese were observed and oxidation process was not observed as shown in Figure 6-1 (a).

The second case is controlled by both dissolution and oxidation processes from the surface. In Courouau's work [5], T91 specimen was exposed to liquid sodium containing 10 wppm of oxygen at 823 K for 1600 h. After the exposure, at the cross section of the specimen, both chromium depleted zone and surface (or internal) oxidation of $NaCrO_2$ were observed as shown in Figure 6-1 (b).

The oxidation process at the surface is followed by the threshold oxygen level for formation of $NaCrO_2$ of each steels and typical sodium-cooled fast reactor is operated 9-10 ppm of oxygen in liquid sodium environment. Based on data in Table 6-1, stability of $NaCrO_2$ as fuinction of temperature and oxygen concentration is depicted in Figure 6-2 (a). In typical SFR, oxygen concentration in liquid sodium is controlled by cold trap system, and the contolled oxygen level is near 9-10 ppm corresponding to oxygen saturation at temperature between 280 K and 310 K. In this environment, oxidation process at the surface of each steels is thermodynamically occur as shown in Figure 6-2 (b). Due to higher oxygen concentration in SFR system than the threshold oxygen level for formation of $NaCrO_2$, oxidation mechanism is more carefully considered.

In this chapter, two corrosion models for sodium corrorion is suggested using schematic illustration and it is qualitatively compared to author's experimental results. Quantitative analysis such as the weight loss by the model development will be calculated for further work.

6. 2 Corrosion model

The corrosion models based on ferritic/martensitic steel is suggested in Figure 6-3. Case I corrosion model suggests that only dissolution occurred at the surface. In ferritic/martensitic steel, chromium is first depleted and later iron depletion occurs. It causes the surface recession since iron is the main element in the chromium depleted zone. Case II corrosion model suggests that both chromium depletion and internal (or intergranular) oxidation first occur and later iron depletion occurs. It causes the surface recession. For detail explanation, Figure 6-4 shows the oxidation mechanism while the material is exposed to liquid sodium containing high level oxygen. When ferritic/martentici steel is exposed to sodium containing oxygen, chromium is diffused to the surface through the prior austenite grain boundaries. This behavior is drived by dissolution process. When chromium is diffused through the prior austenite grain boundaries, chroium meet sodium oxide (Na_2O) at the surface. Then, the $NaCrO_2$ reaction first occurs at the the prior austenite grain boundaries. Some chromium which is diffused into liquid sodum, meet Na_2O in liquid then $NaCrO_2$ reaction occurred in the liquid. While oxidation process at the surface and in liquid, Na_2O also diffused into the solid through the prior austenite grain boundaries and lath boundaries. In the solid, diffused chromium from the matrix also meet Na_2O and $NaCrO_2$ reaction occurred as intergranular oxidation. As the results, there are

chromium depleted zone and pore due to chromium depletion. This process is fully introduced in Figure 6-4. However, the mass flux of chromium in liquid, $J^{'}_{Cr}$, is more dominant than the mass flux of chromium in solid, J_{Cr}. Since the results of 300 h of shor-term compatibility test of Gr.92 and HT9 steel with oxygen saturated sodium at 923 K shows significant higher weight loss than that results at 823 K. In Figure 6-7, the cross-section of Gr.92 steel samples after immersed in oxygen saturated sodium at 923 K is shown, the intergranular carrion is observed. To compare chemical depth profile between 823 K and 923 K results, GD-OES depth profiles of this test are shown in Figure 6-8 to 6-9.

GD-OES results show that the depth profiles of sodium peak in the matrix is near 40 μm at 923 K and near 20 μm at 823 K. Assuming that the sodium peak indicates $NaCrO_2$, the mass flux of Na_2O in solid, J_{Na_2O}, at 923 K is offcourse higher than that at 823 K.

Discussed above phenomena will be used to calculate the weight loss value for further work.

Table 6-1. Threshold oxygen level in sodium for the formation of NaCrO₂ in contact with different alloys [10].

Material	Equation $\ln C_O = A + B/T(K)$	Threshold oxygen concentration (ppm)		
		573 K	773 K	973 K
304 SS	12.1126-9734.8/T	0.00076	0.619	8.244
316 SS	12.3233-9949.8/T	0.0064	0.576	8.126
D9	10.2537-7793.4/T	0.0328	1.17	9.57
Fe-9Cr-1Mo	13.0096-10769.6/T	0.0031	0.394	7.03
Fe-2.25Cr-1Mo	13.6242-10761.4/T	0.0059	0.734	13.1
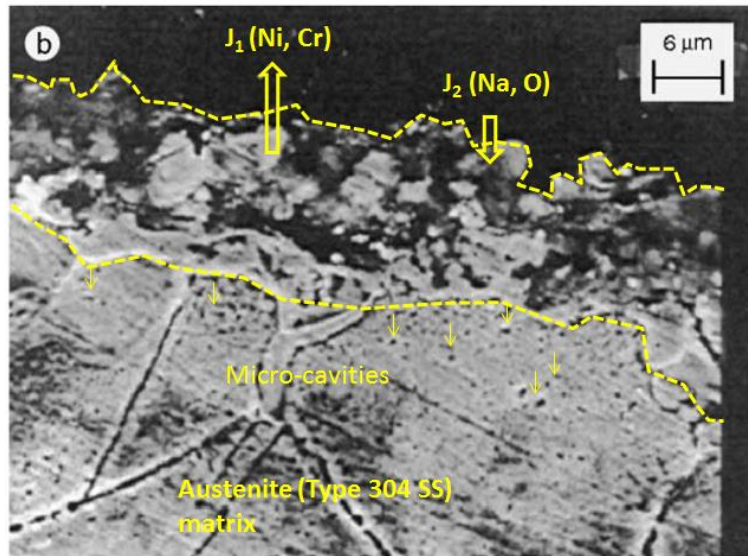
(a)
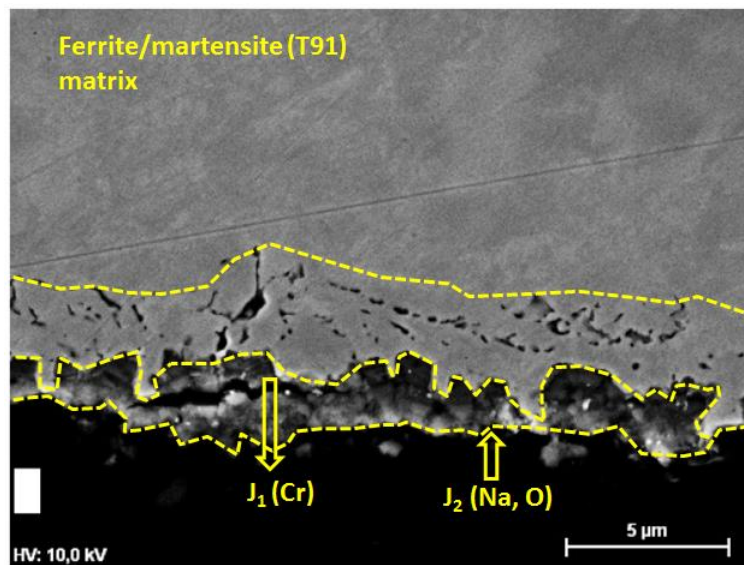
(b)

Figure 6-1. SEM images of cross-section; (a) of 304 SS specimen exposed to flowing sodium containing 1-2 ppm oxygen at 823 K for 60,000 h (additional exposure at 873 K for 20,000 h), and (b) of T91 specimen exposed to liquid sodium containing 10 wppm of oxygen at 823 K for 1600 h [5, 18].
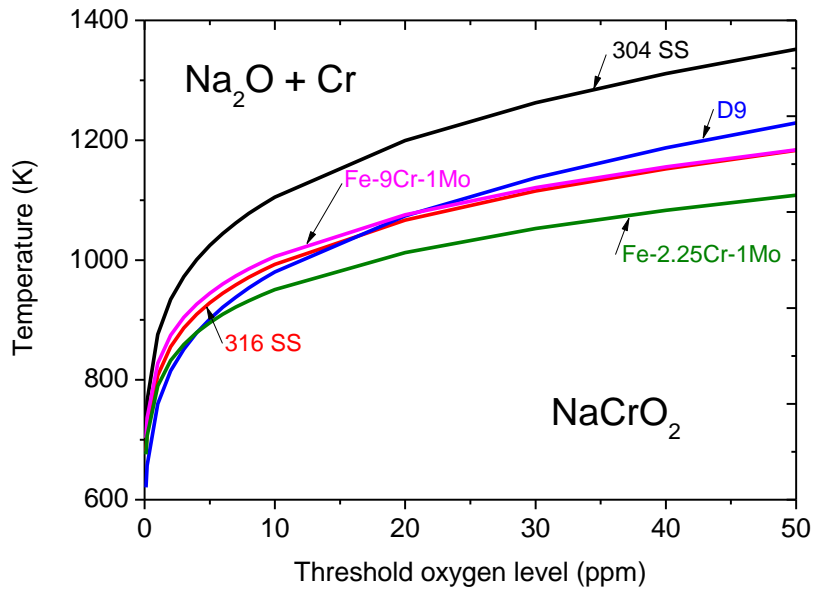
(a)
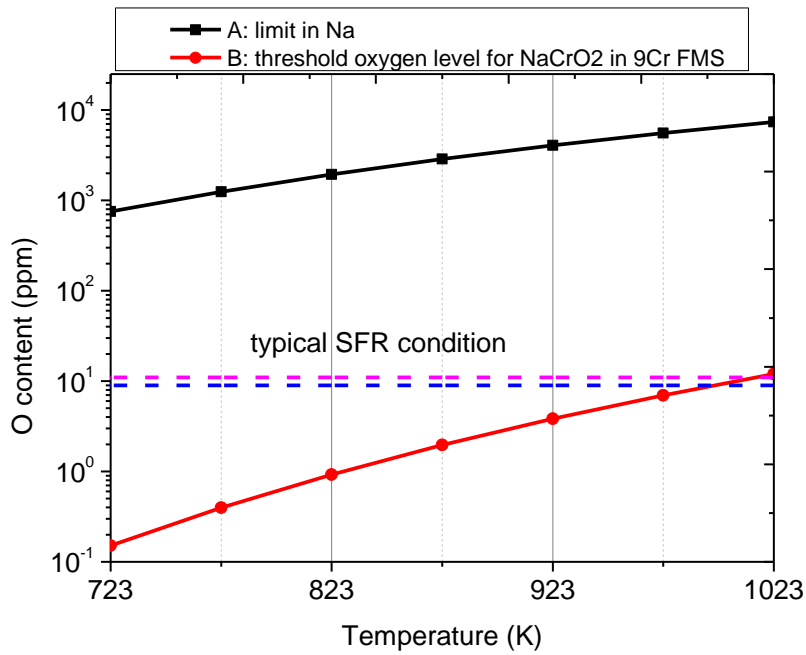
(b)

Figure 6-2. The graph of threshold oxygen level for NaCrO$_2$ on 9Cr ferritic/martensitic steel as function of oxygen concentration dissolved in liquid sodium (a) and the oxygen concentration in typical SFR (b).

• Case I

Liquid

J'_{Na-O} : Mass flux of Na_2O in liquid
J_{Na-O} : Mass flux of Na_2O in solid
J'_{Cr} : Mass flux of Cr in liquid
J_{Cr} : Mass flux of Cr in solid
RΔt: surface recession
Y: reaction layer thickness

y

J'_{Fe} J'_{Cr}

Fe(t_1)
Fe(t_2)   RΔt
Fe(t_3)   Y   y J_{Cr}
x   Cr depleted zone

Fe

Cr

concentration   solid
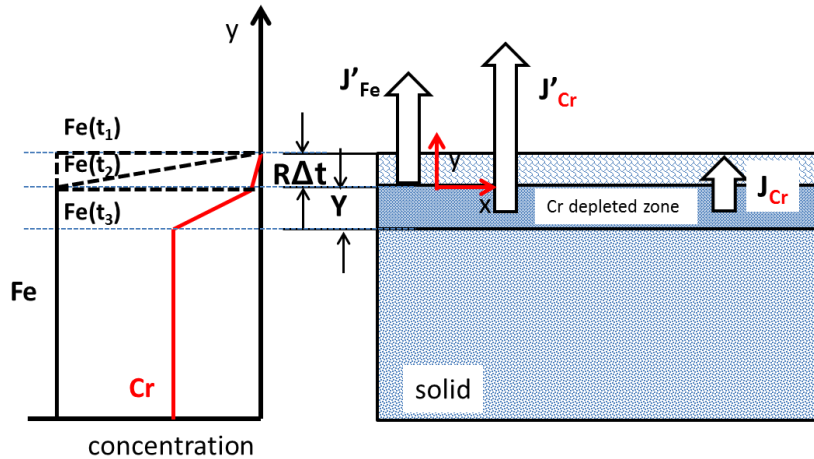
(a)

• Case II

Liquid

J'_{Na-O} : Mass flux of Na_2O in liquid
J_{Na-O} : Mass flux of Na_2O in solid
J'_{Cr} : Mass flux of Cr in liquid
J_{Cr} : Mass flux of Cr in solid
RΔt: surface recession
Y: reaction layer thickness

J'_{Na-O}

J'_{Na-O} $NaCrO_2$

FeO J'_{Cr} J_{Na-O}

y   y

Fe(t_1)
Fe(t_2)   RΔt J'_{Fe}
Fe(t_3)   y
x $NaCrO_2$ Na   O

Fe   Y   Fe

Cr depleted zone J_{Cr} Cr

Cr   solid

concentration   concentration
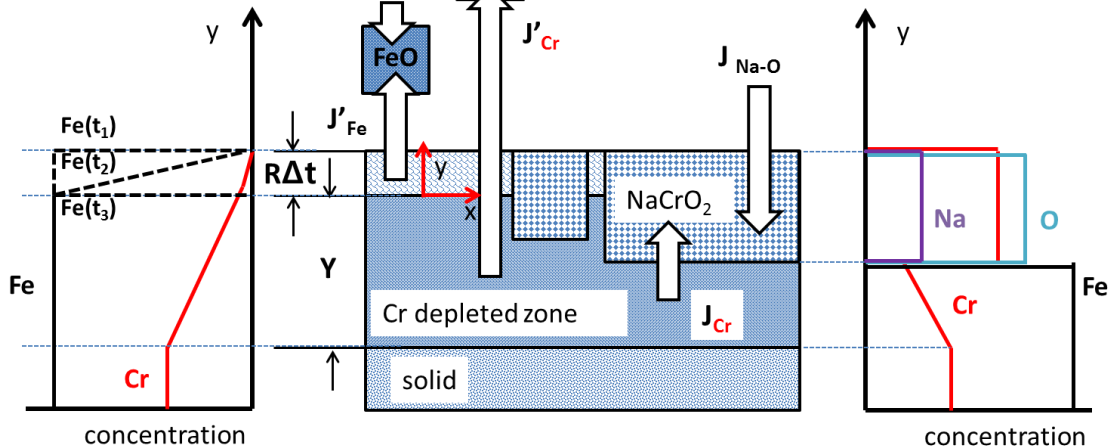
(b)

Figure 6-3. Corrosion mechanism of (a) chase I mode: shows selective depletion of chromium and surface recession by iron depletion into sodium and (b) case II mode: shows internal or intergranular oxidation, accelerated depletion of chromium and surface recession by iron depletion into sodium.

- Stage-1: Cr diffusion onto surface
  - Cr
  - Na_2O

Liquid metal

surface

Martensite lath

Prior austenite grain boundaries

(a)

- Cr
- Na_2O
- Pore
- $NaCrO_2$
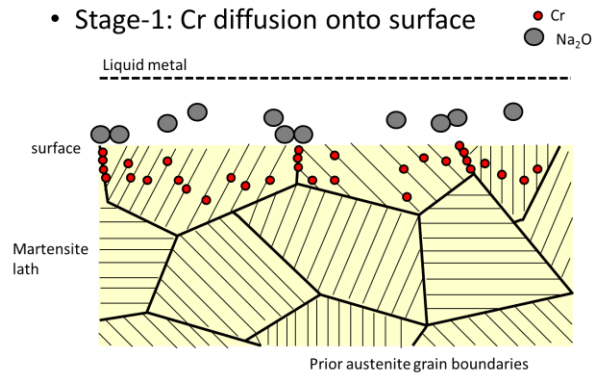
- Stage-2: local oxidation (g.b)

Liquid metal

surface

Martensite lath

Prior austenite grain boundaries

(b)

- Cr
- Na_2O (in liquid)
- Na_2O (in solid)
- Pore
- $NaCrO_2$
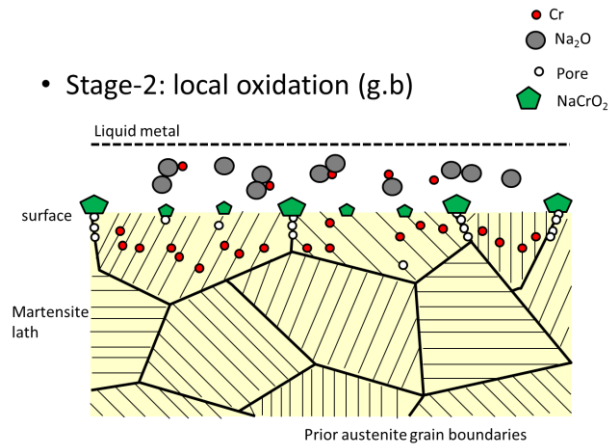
- Stage-3: Na_2O penetration

Liquid metal

surface

Martensite lath

Prior austenite grain boundaries

(c)

1 2 2
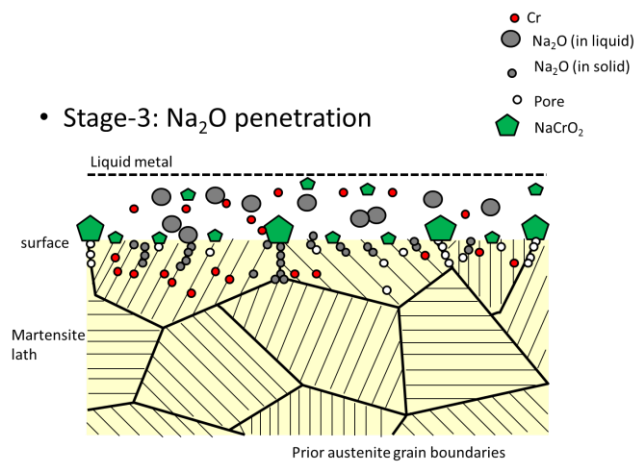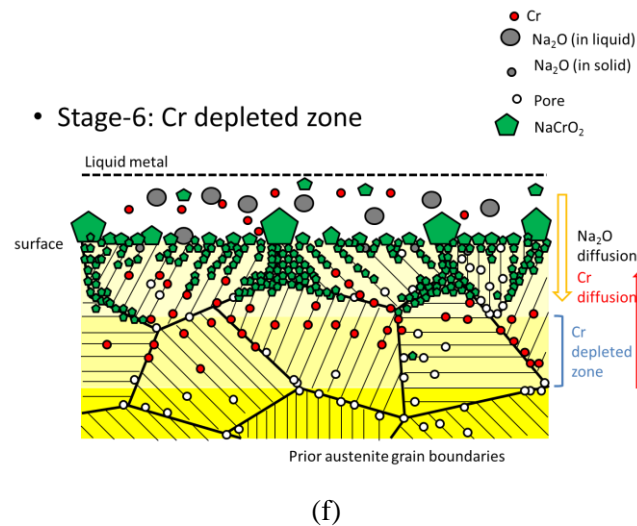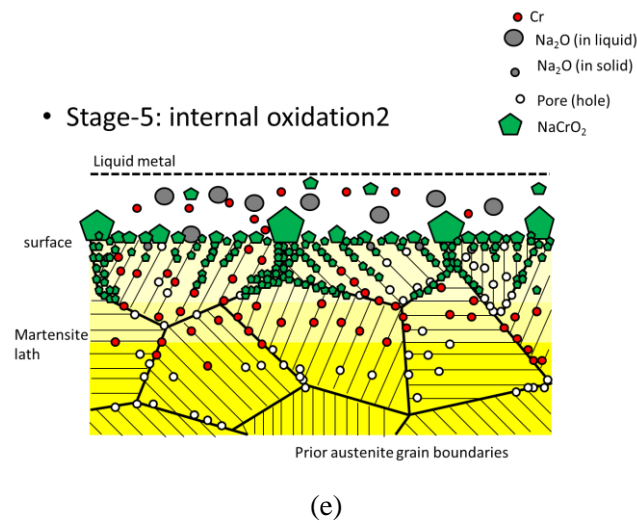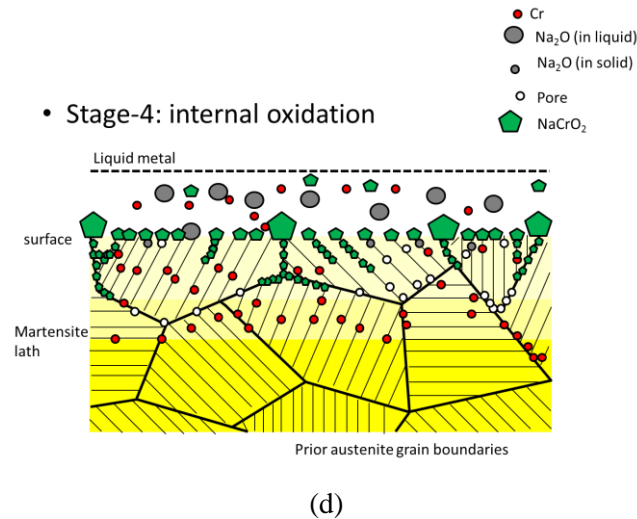
Figure 6-4. Oxidation mechanisms of ferritic/martenstici steel in liquid sodium containing high level of oxygen concentration.
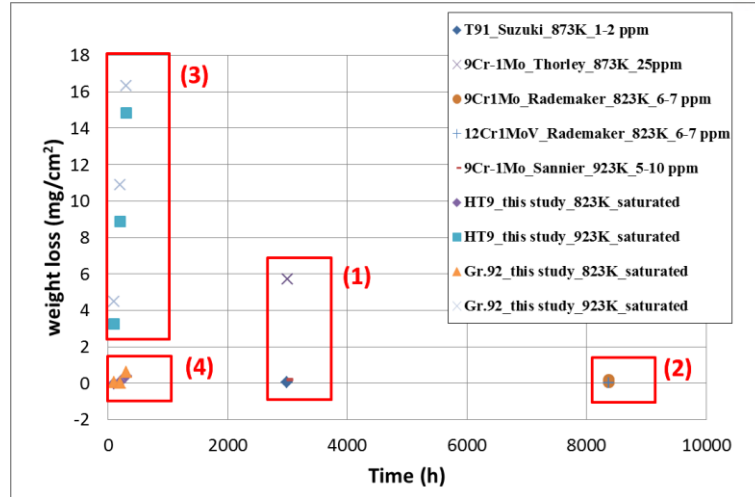
(a)
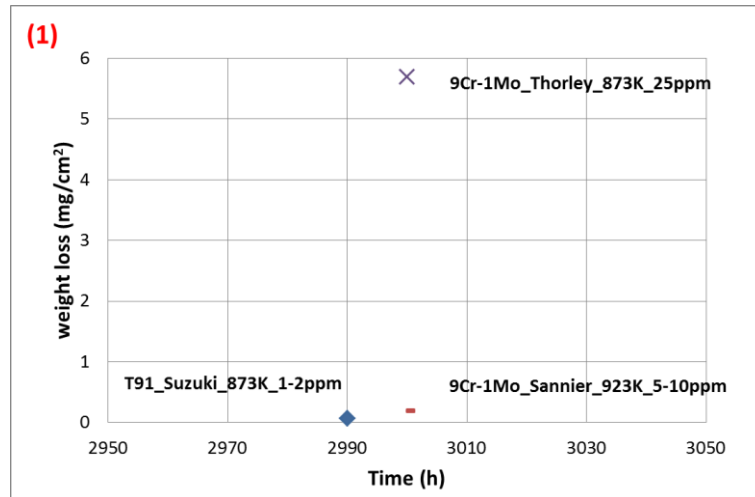
(b)
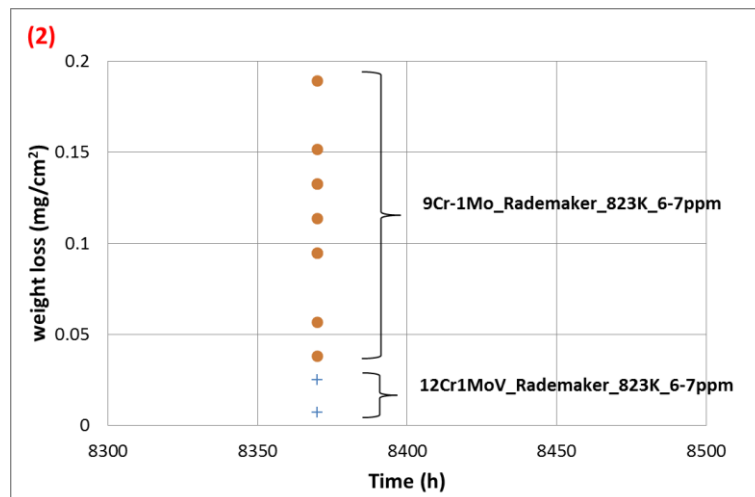
(c)
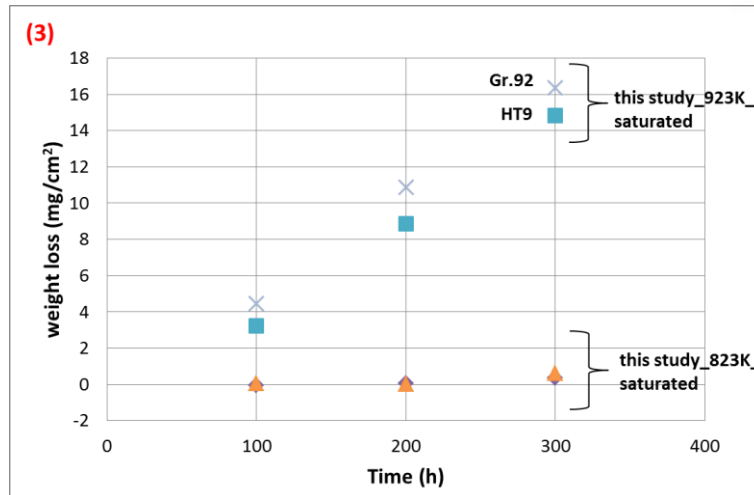
(d)
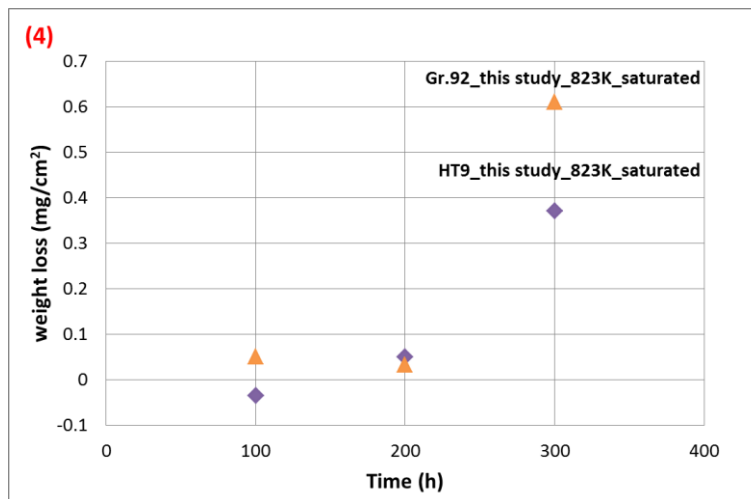
(e)

Figure 6-5. The comparison graphs of the weight loss after exposure to liquid sodium at each conditions; (a) all results, (b) 9Cr-1Mo sresults at 823K and 873K [18-20], (c) 9Cr and 12Cr steels exposed to same condition at 823 K sodium containing 6-7 ppm oxygen [7], (d) Gr.92 and HT9 steels exposed to sodium at 823 K and 923 K with saturated oxygen condition, and (e) Gr.92 and HT9 steels exposed to sodium at 823 K with saturated oxygen condition.
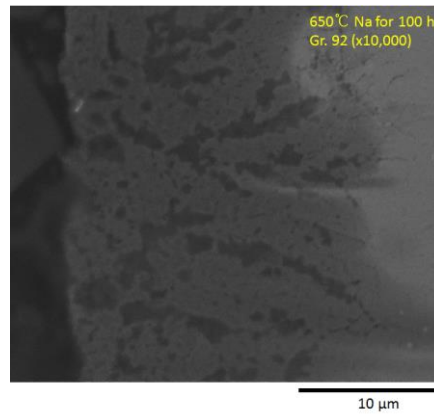
(a)
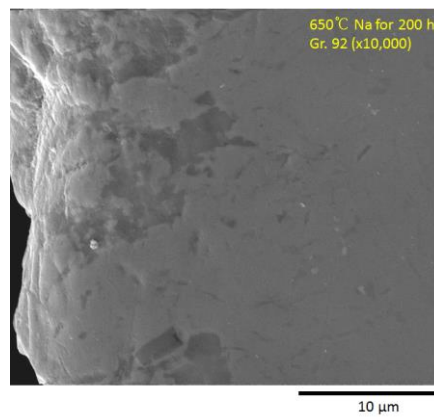
(b)
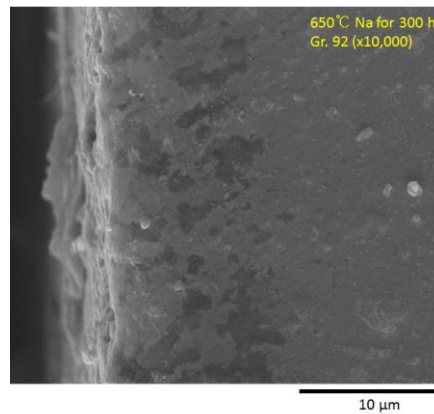
(c)

Figure 6-7. SEM images of the cross-section of Gr.92 steel after exposure to oxygen saturated sodium at 923 K after exposure to (a) 100 h, (b) 200 h and (c) 300h.
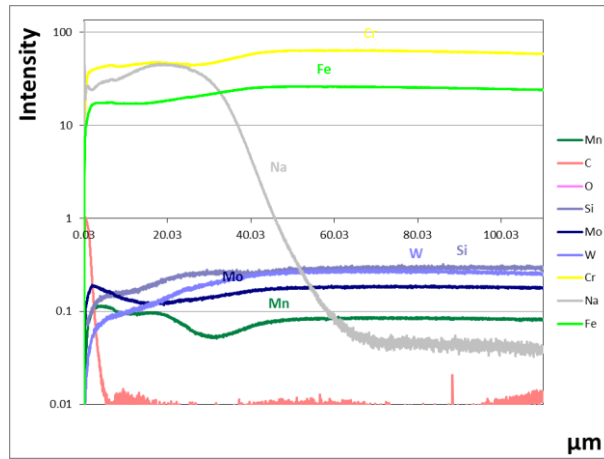
(a)
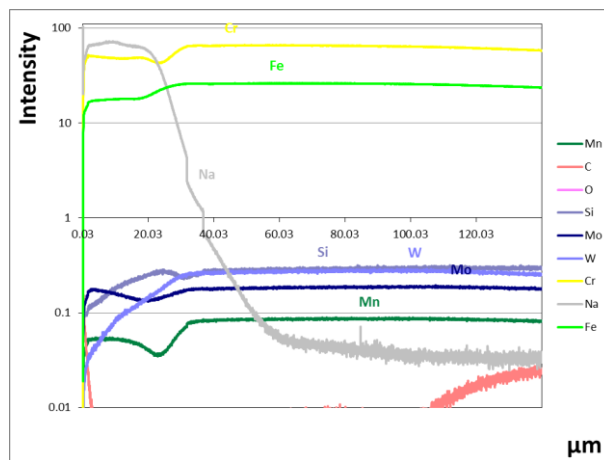
(b)
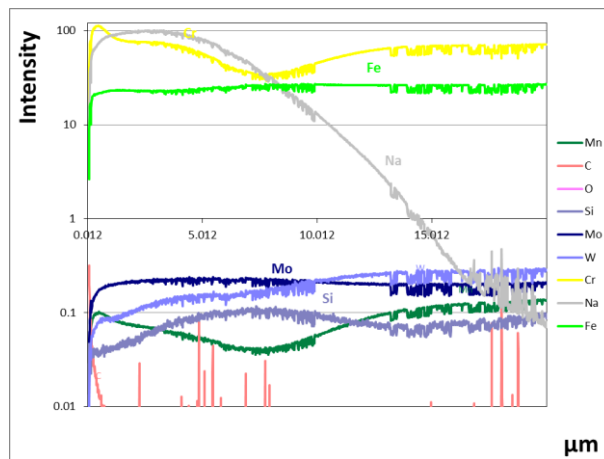
(c)

Figure 6-8. GD-OES depth profiles on Gr.92 samples immersed in liquid sodium at 923 K after exposure to (a) 100 h, (b) 200 h and (c) 300 h (under re-analyses).
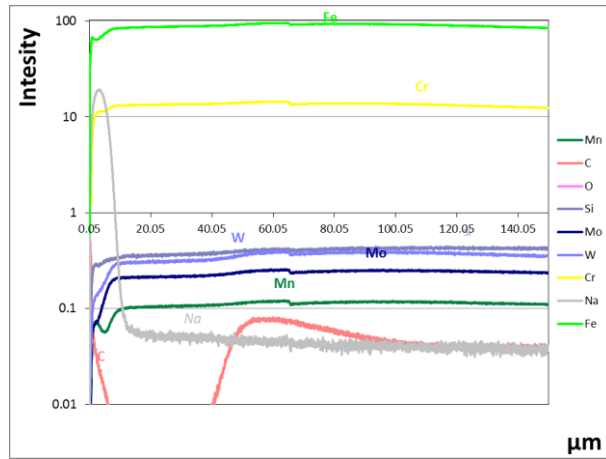
(a)
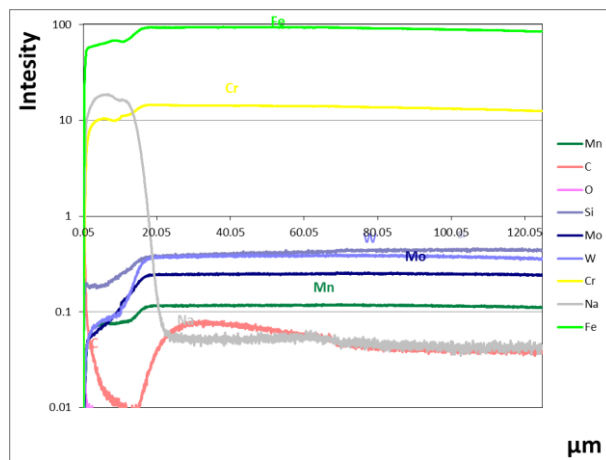
(b)
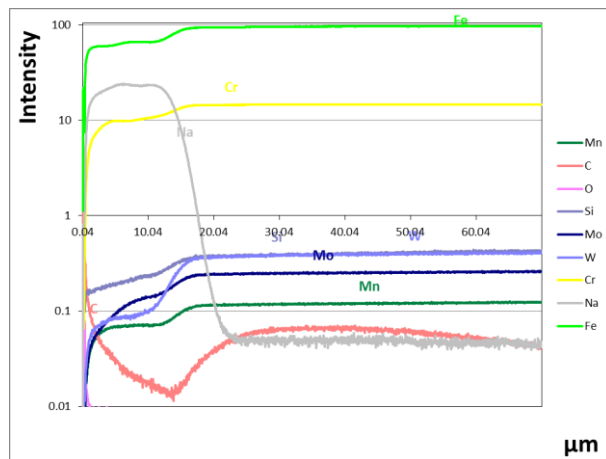
(c)

Figure 6-9. GD-OES depth profiles on Gr.92 samples immersed in liquid sodium at 823 K after exposure to (a) 100 h, (b) 200 h and (c) 300 h.

6.3 Reference

1. E.G. Brush, GEAP-4832, General Electric, 1965.

2. J. Zhang, T.F. Marcille, R. Kapernick, Corrosion, 64 (2008) 563.

3. J. Zhang, P. Hosemann, S. Maloy, J. Nucl. Mater. 404 (2010) 82-96.

4. F.B. Ce´le´rier, J.L. Courouau, C. Desgranges, L. Martinelli, F. Rouillard, in: Proceedings of International Congress on Advances in Nuclear Power Plants (ICAPP) 2011, Nice, France, May 2-5 (2011) 2392-2402.

5. J-L. Courouau, F.B. Ce´le´rier, V. Lorentz, T. Dufrenoy, in: Proceedings of International Congress on Advances in Nuclear Power Plants (ICAPP) 2011, Nice, France, May 2-5 (2011) 2439-2449.

6. S. He´mery, T. Auger, J.L. Courouau, F. Balbaud-Ce´le´rier, Corros. Sci. 76 (2013) 441-452.

7. P.L.F. Rademakers et al., J. Nucl. Mater. 97 (1981) 309-318.

8. M. Rivollie, J.L. Courouau, M.L. Giorgi, F. Jomard, V. Lorentz, M. Tabarant, Eurocorr 2014, Pisa, Italy, EFC.

9. A.W. Thorley, A. Blundell, J.A. Bardsley, Materials Behavior and Physical Chemistry in Liquid Metal Systems, Eds. H.U. Borgstedt, (Plenum, New York, 1982) 5.

10. S.R. Pillai, H.S. Khatak, J.B. Gnanamoorthy, J. Nucl. Mater. 224 (1995) 17.

11. S.A. Jansson, E. Berkey, in: Corrosion of Liquid Metals, Eds. J.E. Draley, J.R. Weeks (Metallurgical Society of AIME, New York, 1970) 479.

12. M.G. Adamson, E.A. Aitken, D.W. Jeter, Proc. Int. Conf. on Liquid Metal Technology in Energy Production, Seven Springs, 1976 (National Technology Information Service, Springfield, 1976) CONF-760503, part II, p. 866.

13. C.F. Knights and B.A. Philips, in: High Temperature Chemistry of Inorganic and Ceramic Materials, Special Publication No. 30 (Chemical Society, London, 1977) p. 134.

14. B.J. Shaiu, P.C.S. Wu and P. Chiotti, J. Nucl. Mater. 67 (1977) 13.

15. S.A. Frankham, Ph.D Thesis, University of Nottingham, UK (1982).

16. O.M. Sreedharan, B.S. Madan and J.B. Gnanamoorthy, J. Nucl. Mater. 119 (1983) 296.

17. N.P. Bhat, K. Swaminathan, D. Krishnamoorthy, O.M. Sreedharan and M. Sundaresan, Proc. 3rd Int. Conf. on Liquid Metal Engineering and Technology, Oxford, 1984 (The British Nuclear Energy Society, London, 1984) vol. I, p. 323.

18. T. Suzuki, I. Mutoh, J. Nucl. Mater. 149 (1987) 41-50.

19. A.W. Thorley, C. Tyzack, in: Proc. Conf. Liquid Metals. (British Nuclear Energy Society, 1973) 257.

20. J. Sannier, Chemical Aspects of Corrosion and Mass Transfer in Liquid Sodium, Eds. S.A. Jansson, Proc. Symp., October 1971 (Metallurgical Society of AIME) p. 278.

7. CONCLUSIONS

7.1 Compatibility test of Gr.92 with liquid sodium

In order to investigate the effect of liquid sodium containing dissolved oxygen on precipitates in Gr. 92 steel, specimens were exposed to liquid sodium or to an argon environment at 650℃ for certain times up to 3095 h.

1. Intergranular oxidation (NaCrO2) and a chromium depletion zone were observed at the surface for sodium-exposed specimens, but not observed in argon-exposed specimens.

2. V-rich MX-type carbonitride and M23C6 were found in the as-received specimen.

3. At the interface between Cr-depleted zone and the bulk steel matrix in specimens exposed to sodium, the main precipitate observed was M23C6, while Laves phase was the main observed precipitate in specimen at the bulk steel matrix in specimen exposed to sodium and in specimen exposed to the argon environment.

4. The equivalent circle diameter of precipitates in the as-received specimen is the lowest, while sodium-exposed (1583 h) and argon-exposed (1601 h) specimens have similar distributions. For longer exposure times, the equivalent circle diameter of precipitates for sodium-exposed specimens (3095 h) showed higher % than that in argon-exposed specimens (2973 h).

5. In a thermodynamic simulation of long sodium exposure time (depletion to 4 wt% and 5 wt% Cr in the matrix), Laves phase was not formed for most values of C-content (except 0.01 wt%).

7.2 Oxygen measurement

In order to use an potentiometric cell that is functional in liquid sodium at low temperature, the oxide-based electrolytes, gadolinia-doped ceria (GDC-10A and GDC-B), were evaluated as candidate materials due to their known oxygen ion conductivity. Thermochemical stability, conductivity measurements, and emf measurement tests were conducted for these solid electrolytes. The thermochemical stability tests for the GDC-10 (A and B) demonstrated defected surface following exposure to liquid sodium at 200 ℃ for a certain period of time. While exposure to Na, ceria is easily react with sodium or sodium oxide to form ternary oxides such as $NaCeO_2$ and Na_2CeO_3. It is assumed that the ternary compounds were formed and it is not deposited to the surface of the cells. Conductivity measurements as a function of temperature demonstrated the slightly higher conductivity of the GDC-10 A specimens relative to the GDC-10B. The calculated solubility at 450–520K data show higher gradient at the test temperature and it is believed that the behavior is caused

by n-type electrical properties in oxygen saturated sodium environment since the electrolytes were in reducing condition in sodium environment with the formation of ternary compounds ($NaCeO_2$ and Na_2CeO_3) and the lower oxygen partial pressure limit.

7.3 Carbon measurement

For measurement of carbon activity in liquid sodium, α-iron foil samples which were equilibrated in static sodium at 550℃ for 300h, have shown closed value of the carbon activity calculated in 304 SS foil samples which were also equilibrated in the same environment. Since 304 SS foil sample works as a role of reference carbon activity,

Developed relationship of carbon activity and carbon concentration in ferrite iron, can be used to determine carbon activity of liquid sodium.

7.4 Corrosion model

Two diffent mode of corrosion mechanism is suggested. Case I corrosion model suggests that only dissolution occurred at the surface. In ferritic/martensitic steel, chromium is first depleted and later iron depletion occurs. It causes the surface recession since iron is the main element in the chromium depleted zone. Case II corrosion model suggests that both chromium depletion and internal (or intergranular) oxidation first occur and later iron depletion occurs. It causes the surface recession. For further work, weight loss value will be calculated by using discussed analysis.

APPENDIX.

Appendix A.

(*Additional TEM analysis)
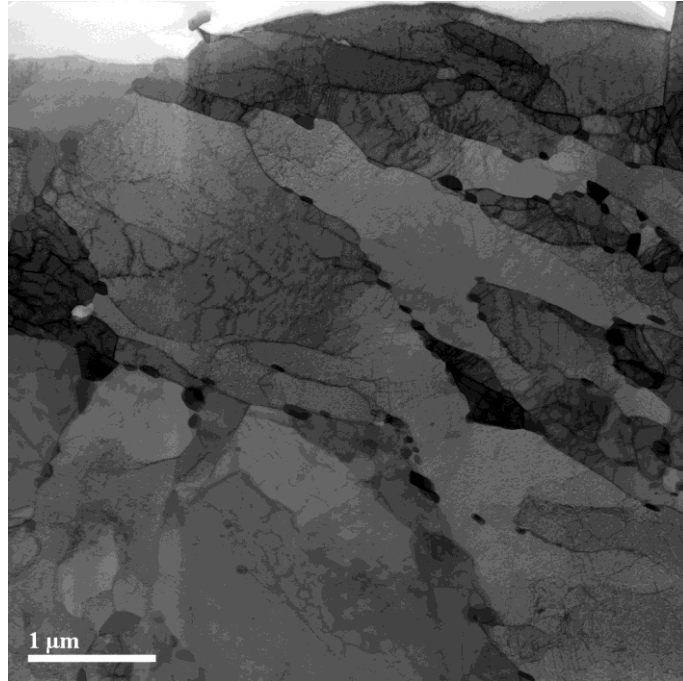
(a)
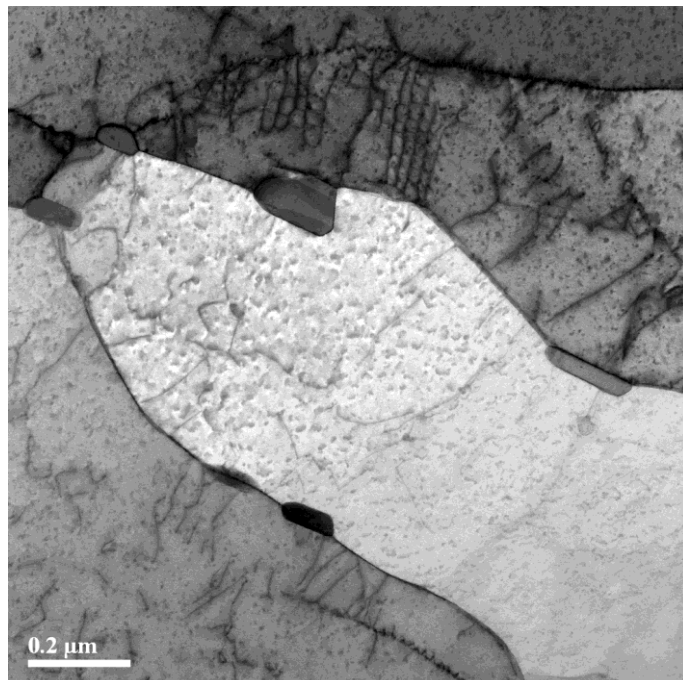
(b)
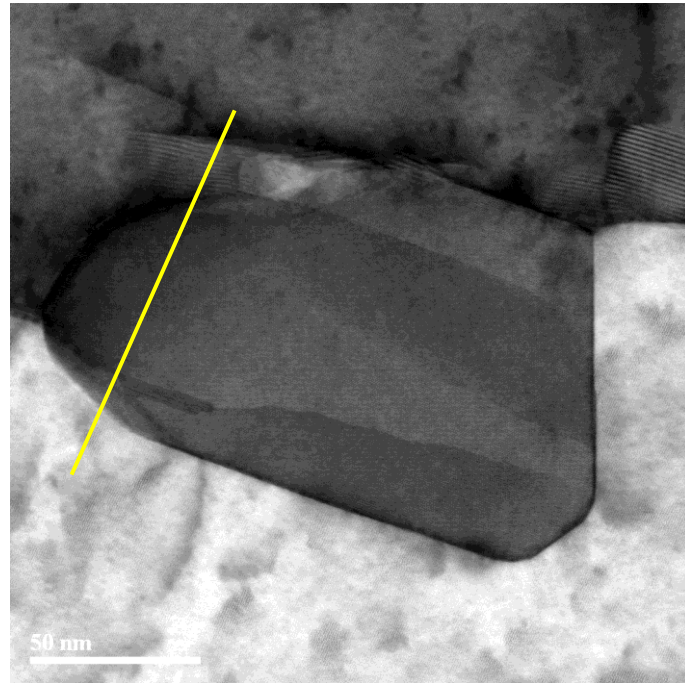
(c)
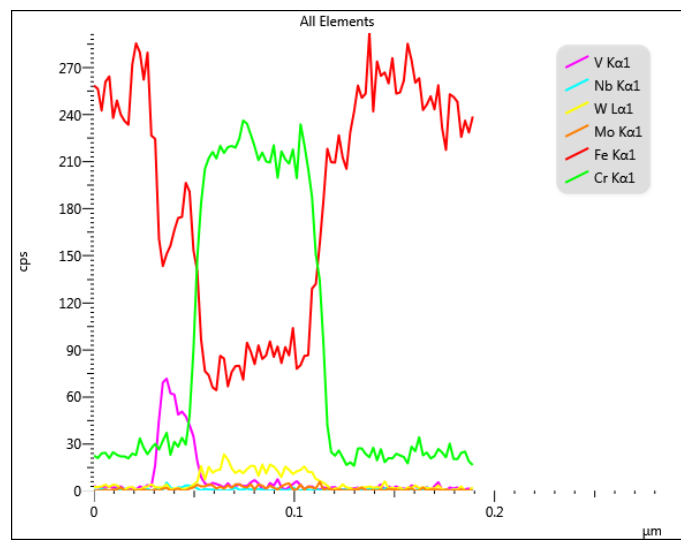
(d)
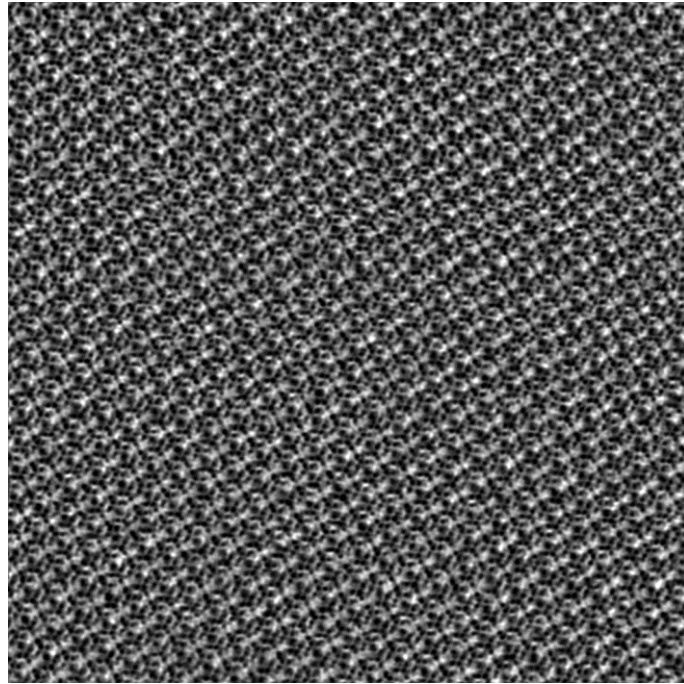
(e)
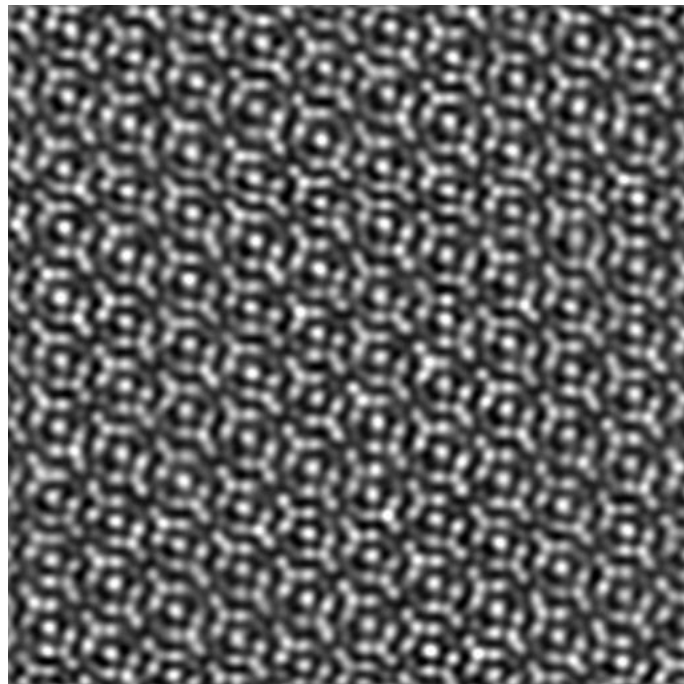
(f)
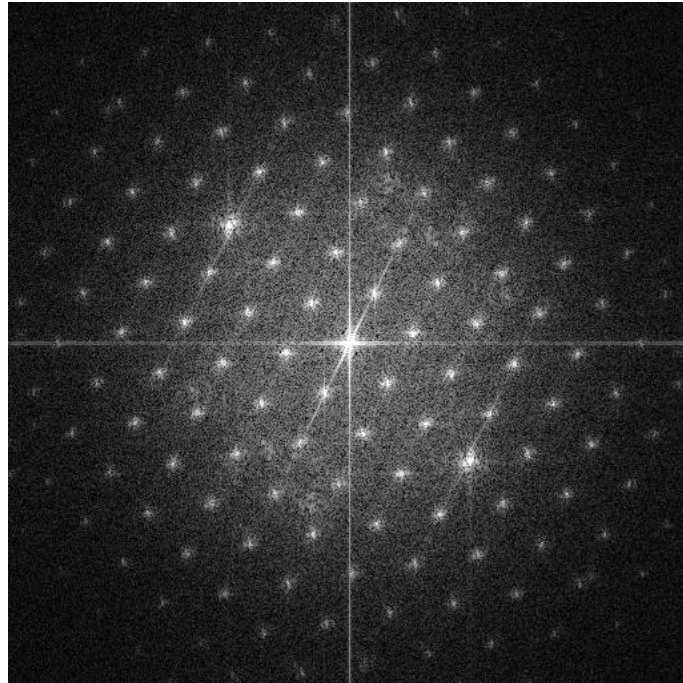
(g)

Figure A-1. The BF-STEM images of $M_{23}C_6$ carbide from samples fabricated by focused ion beam (FIB) at the bulk steel matrix near inner surface in Na-exposed for 1583h.

(a)

(b)

Fe Kα1

Cr Kα1

500nm

500nm

W Lα1

V Kα1

500nm

500nm

Mo Kα1

Nb Kα1
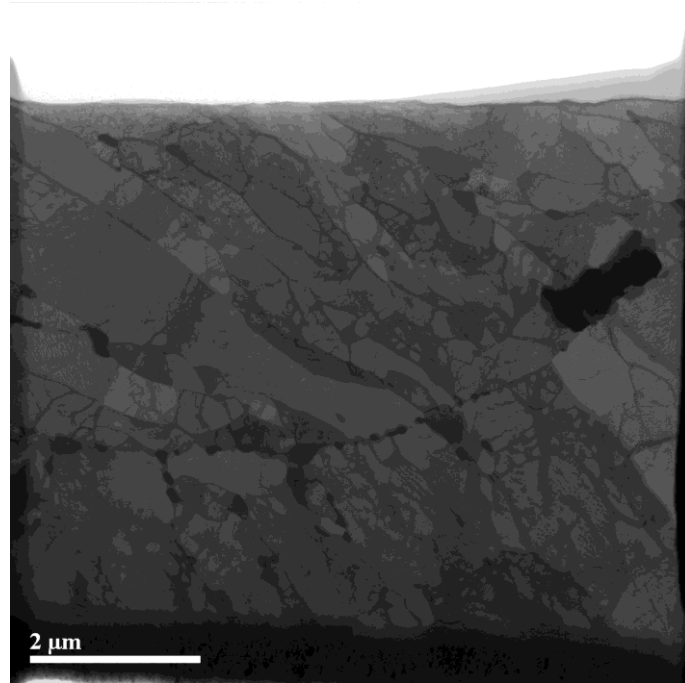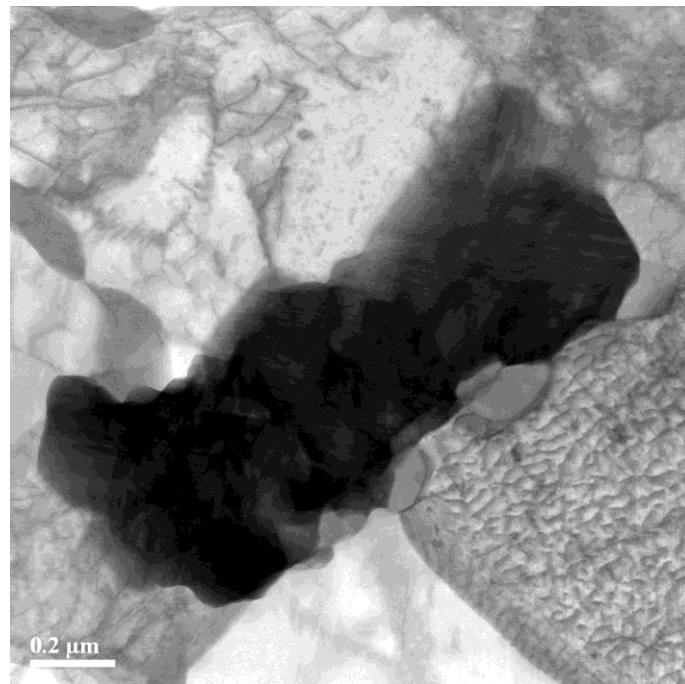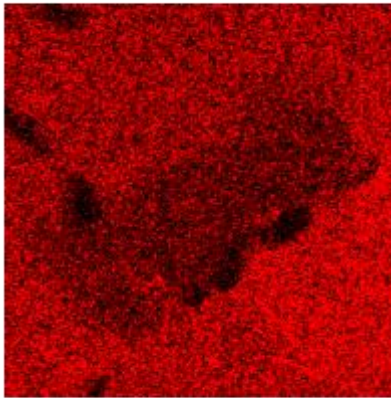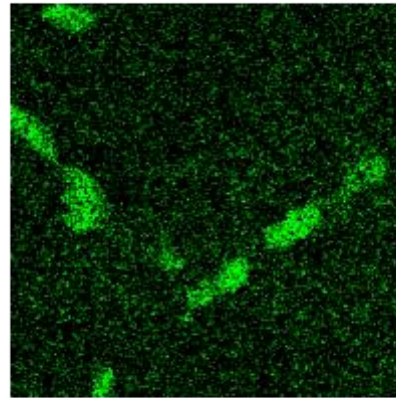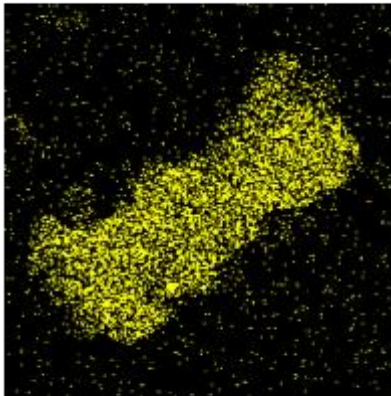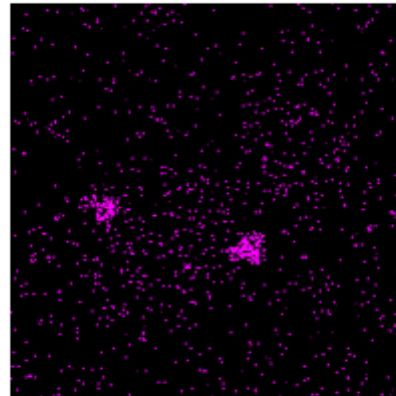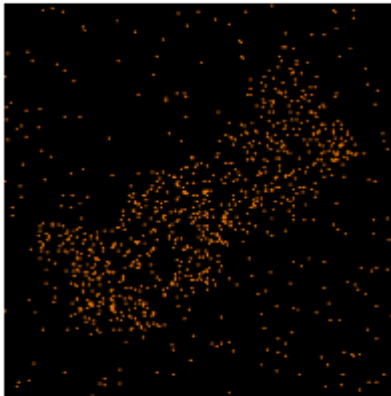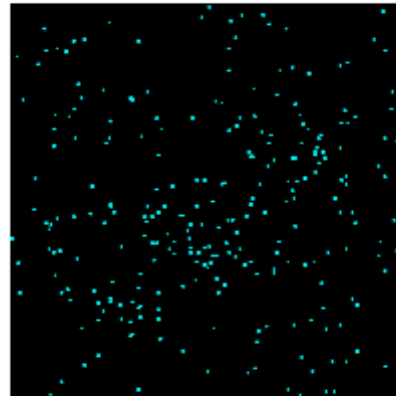
500nm

500nm

(c)
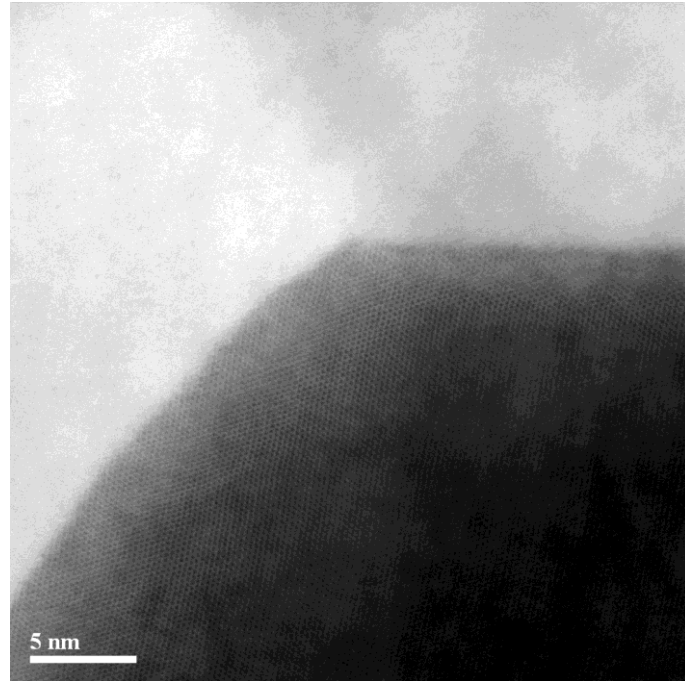
(d)
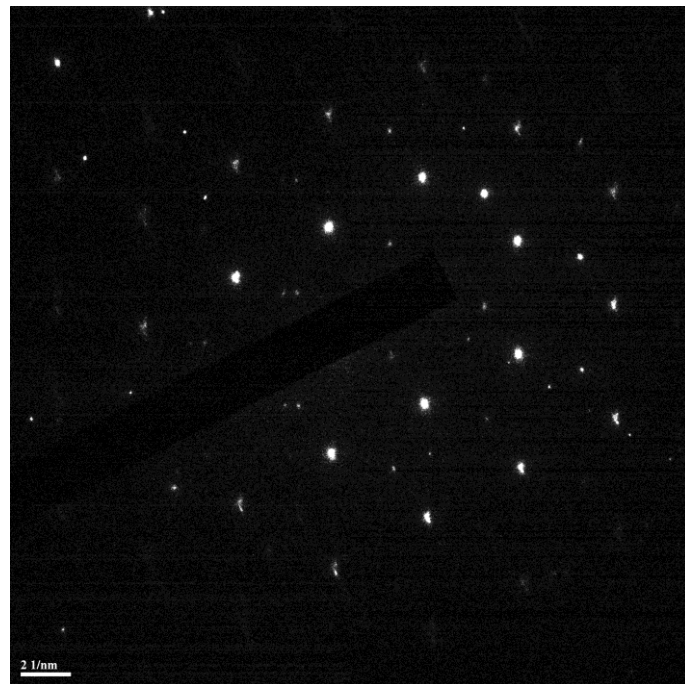
Figure A-2. The BF-STEM images, EDS analysis and DP of Laves phase from samples fabricated by focused ion beam (FIB) at the bulk steel matrix near inner surface in Na-exposed for 3095h.

(a)

(b)

1 4 1

Fe Kα1

Cr Kα1

500nm

500nm

Mn Kα1

W Lα1

500nm

500nm

V Kα1

Mo Kα1

500nm

500nm
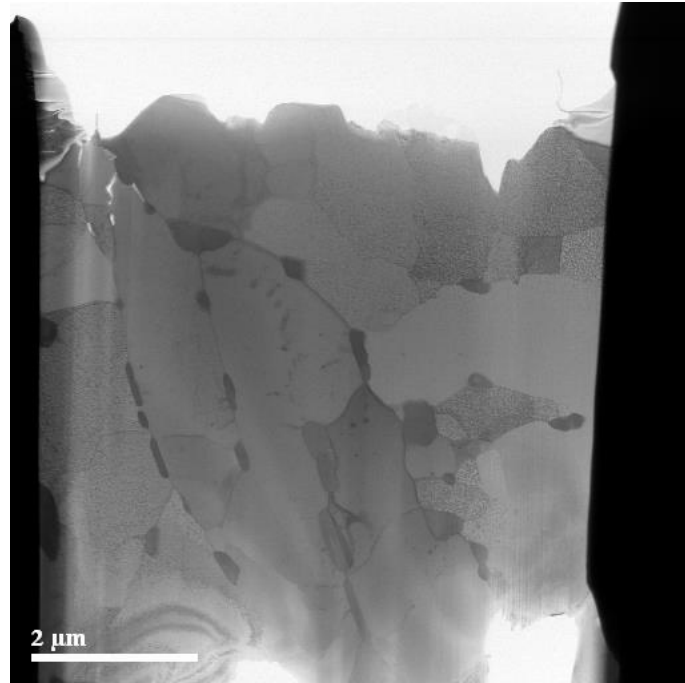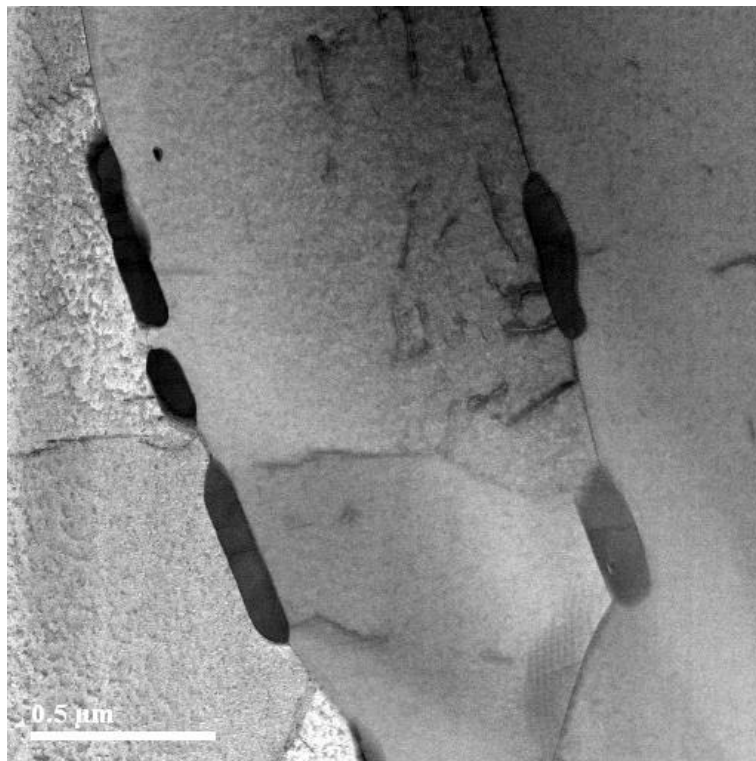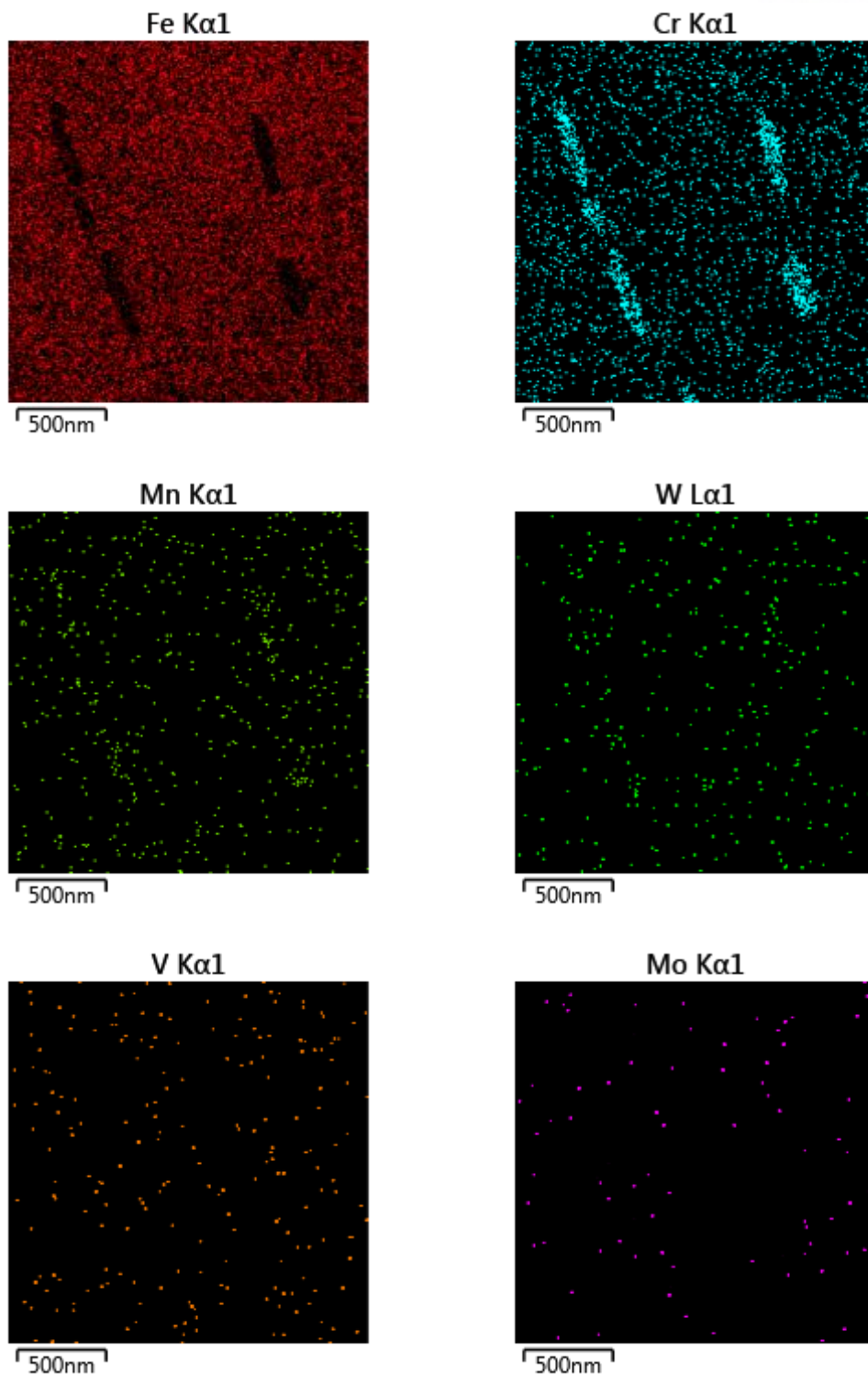
(c)

Figure A-3. The BF-STEM images and EDS analysis of $M_{23}C_6$ carbide from samples fabricated by focused ion beam (FIB) at the interface between the Cr-depleted zone and the bulk steel matrix in Na-exposed for 3095h.
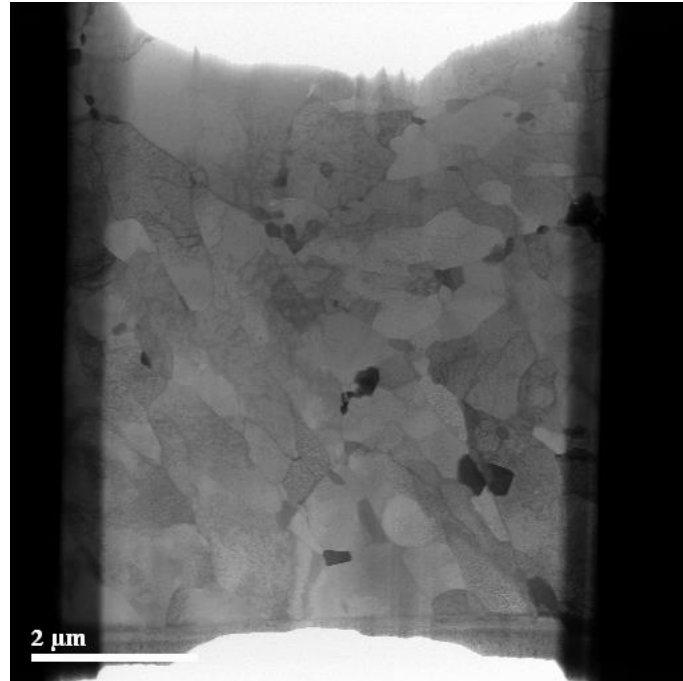
(a)
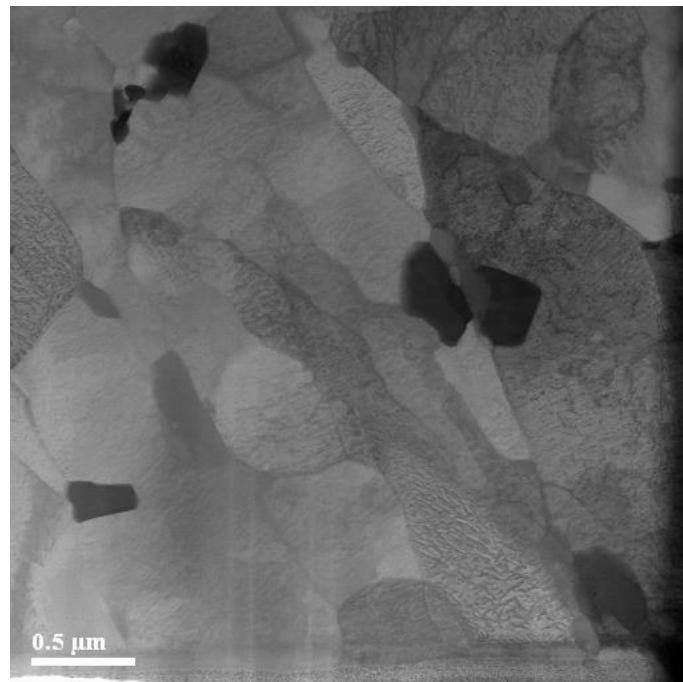
(b)
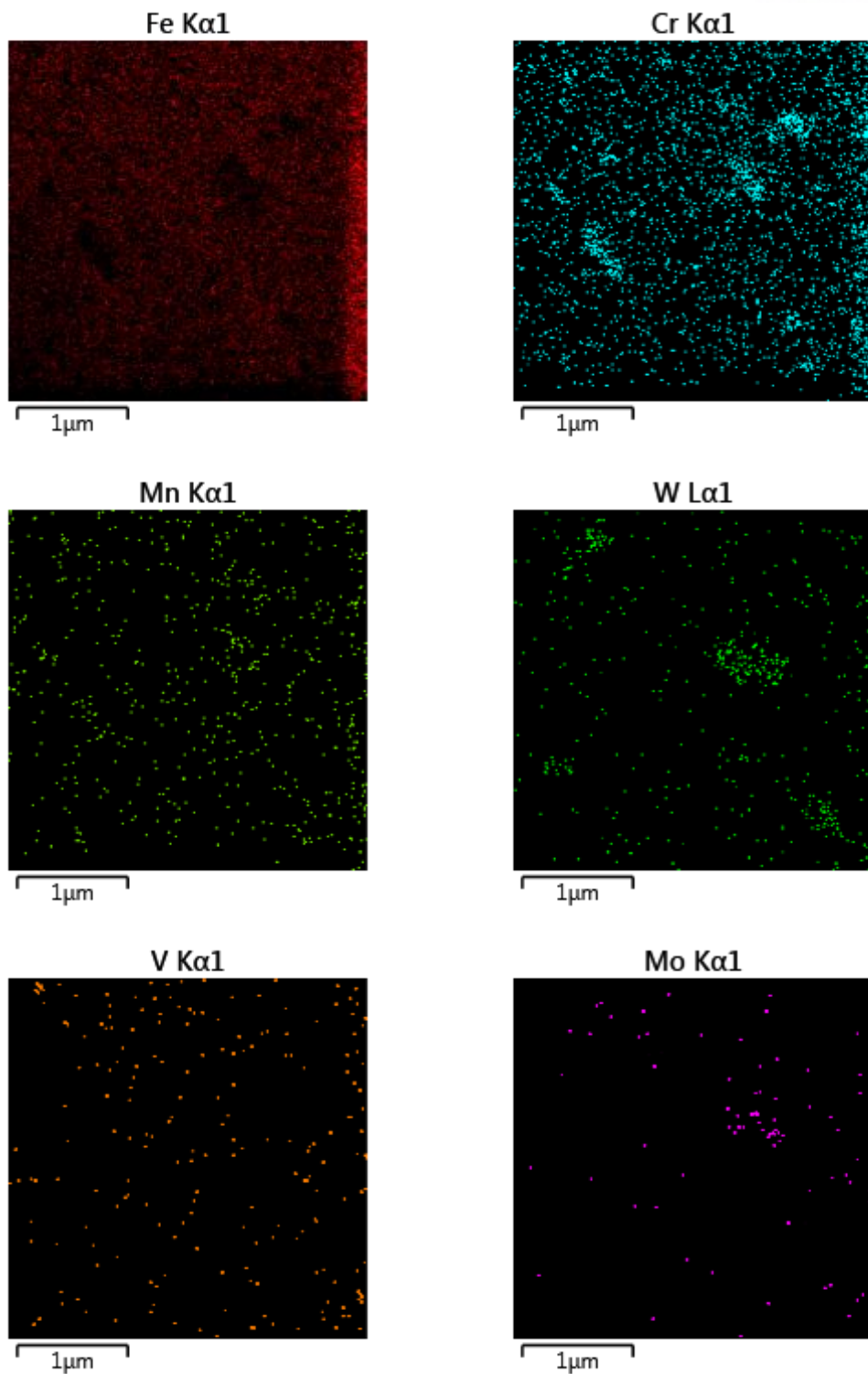
(c)

Figure A-4. The BF-STEM images and EDS analysis of Laves phase from samples fabricated by focused ion beam (FIB) at the interface between the Cr-depleted zone and the bulk steel matrix in Na-exposed for 3095h.

Appendix B.
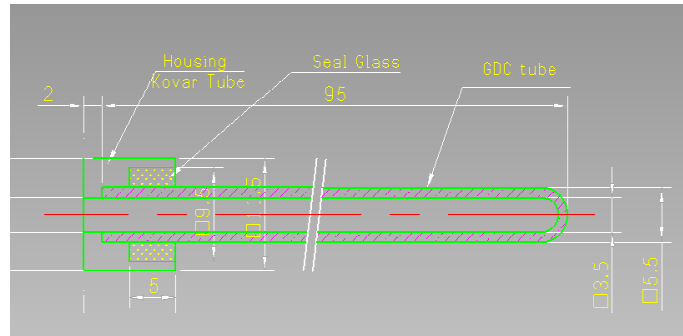
(a)

(b)
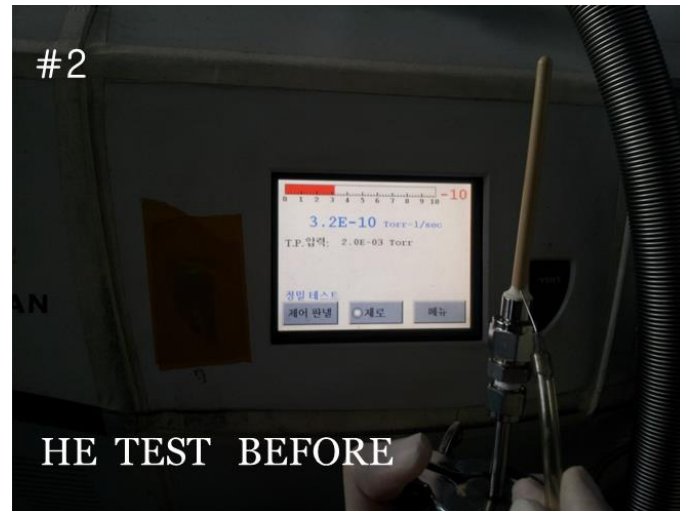
(c)

(d)

Figure B-1. The sealing of the cell, cement joining which has similar the coefficient of thermal expansion with Fe-Ni alloy was introduced between Fe-Ni alloy and both GDC tubes. (a) shows GDC and cell joining design, (b) shows drying process in dry oven at 95 °C after cement joining, (c) shows helium leak test preparation and (d) shows negligible helium leakage at the joining.

Appendix C.
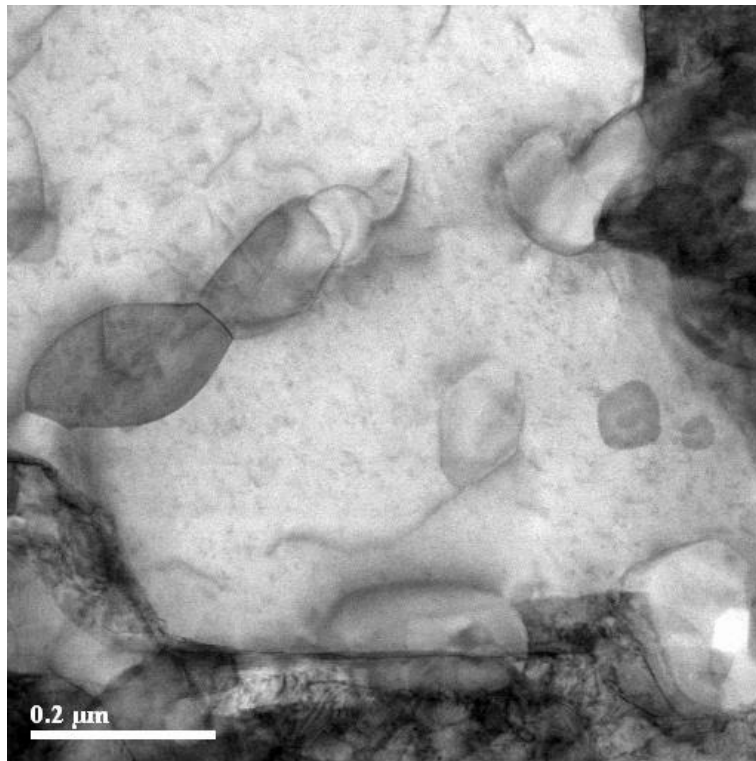
(a)
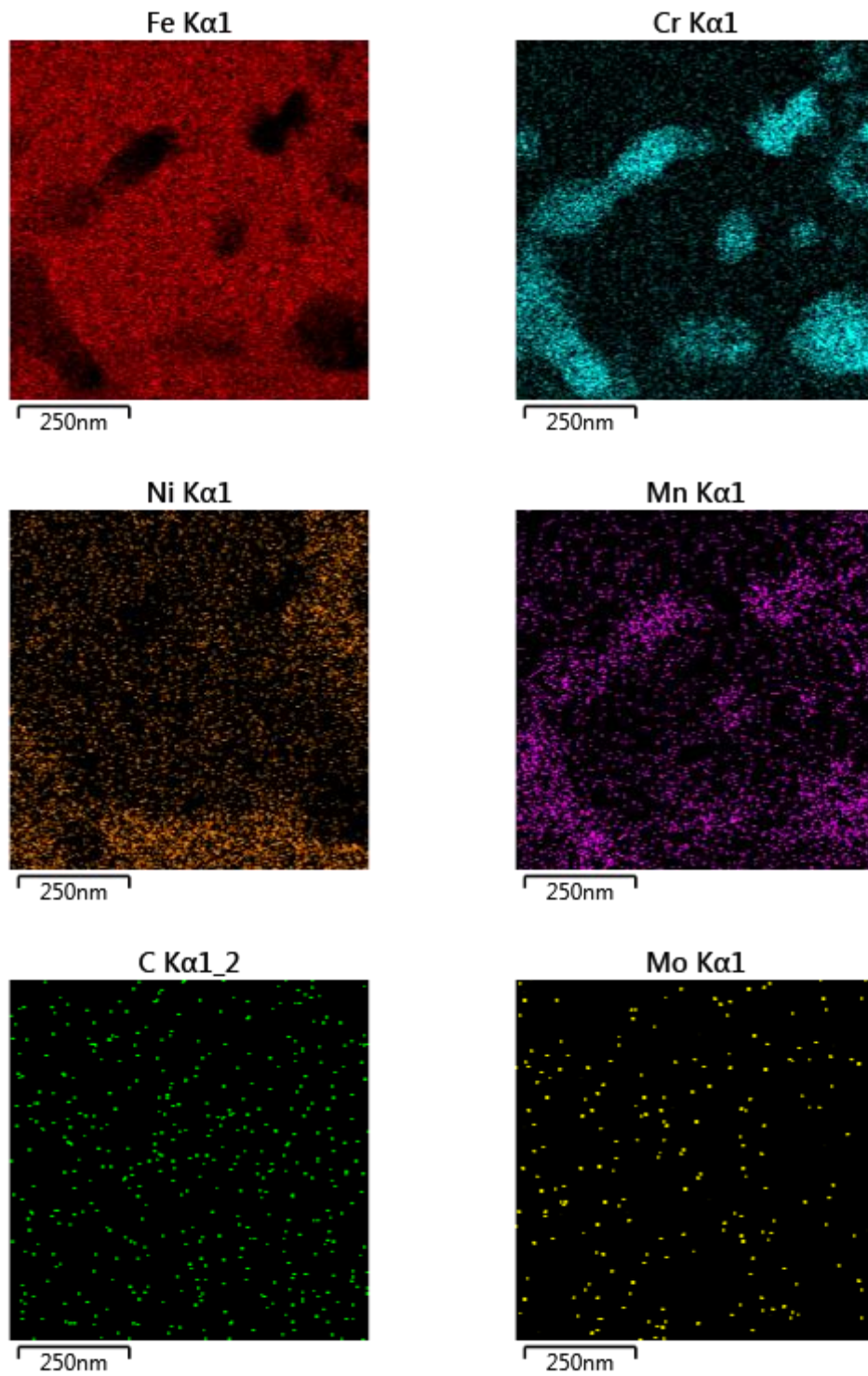
(b)

Figure C-1. BF-STEM image and EDS analysis of $M_{23}C_6$ carbide in austenitic 304 SS foil sample after equilibration in liquid sodium at 550°C for 300 h.

보다 열심히 해나간다면 졸업은 물론이고, 좋은 결실 많이 맺을거야. 상일아, 유니크한 연구 주제뿐만 아니라 유니크한 성격도 앞으로 쭈욱 발산해 나가길 바란다. 그리고 이상하리만치 같이 늦게 퇴근하는 라인 승현, 태호는 지금 잘하는 만큼 앞으로도 초심 잃지말고 하다보면 졸업은 금방 일꺼야. 광범아 너의 초능력은 좀 더 일찍 연구실에 와서 마음껏 펼치기 바라며, 훌륭한 연구결과들 많이 내길 기대하고 있을께. 승창아 지금처럼 묵직하게 일 해나가다 보면 지금처럼 좋은 결실 많이 맺을 수 있을거야. 정원아 늦게 들어온 만큼, 넌 군대에서 겪은 경험으로 현재 연구의 장애물들을 잘 헤쳐 나갈거라 믿는다. 정기도 이제 대학원 생활 시작하는 만큼 원대한 목표를 가지고 시작하길 바랄께. 그리고 액체금속 부식 연구를 이어받은 부사수 정현!! 지금 하고 있는 연구를 계속 발전시켜 나가고 더 좋은 연구 많이 하길 바란다. 지금 잘 하고 있는만큼 앞으로도 사소한 것에서부터 관심 가지며 해결해 나간다면 흥미로운 결과들 많이 밝혀 나갈 수 있을거야. 입학동기로 대학원생활을 같이 시작했지만, 지금은 나보다 먼저 사회에서 각자의 역할을 하고 있는 KAERI 이승원박사님, ANL 김종진박사에게도 고마운 마음을 전합니다. 랩 초창기에 3 명이서 국내학회며 미국학회를 참 많이도 같이 다녔던 것 같네요. 그리고 우리연구실 석사 졸업생이자 현대제철에서 일하고 있는 정석이와 KAERI 에서 일하고 있는 주앙에게도 고마운 마음을 전합니다.

그리고 열수력 연구실, 성대야 지난 동안 연구적으로 많은 도움도 받았는데, 이번에 같이 졸업하게 되서 더없이 반갑다. 앞으로도 많은 연락을 주고받으면서 지내도록 하자. 사라야! 지난 5 년간 수업도 같이 열심히 듣고, Q.E 도 같이 보고 했는데, 남은 기간 좀만 더 열심히 해서 얼른 졸업하길 바랄께. 한! BAERI 과제하면서 너랑 술을 제일 많이 마신거 같다. 앞으로도 연구 외적으로 내적으로 왕성한 행보 이어가길 바란다. 그리고, 경모, 인국, 성보, 석빈, 효, 영신아, 연구실 놀러 가면 인사 잘 해주고 반겨줘서 고마웠어. !! 방인철 교수님 지도 아래 좋은 연구 많이 하길 바랄게.

노심 연구실의 태우, 현석이, 수영이, 치동이, 지원이 모두 고마워. 핵연료 연구실 동갑내기 병진이, 제균이, 지현이, 관윤이, 태원아 같이 지낸 시간 참 즐거웠고 많이 생각날거야. 방사선 연구실의 동한형 좀만 더 고생하시구, 욱제도 지난 동안 고마웠어.

KAERI 고속로핵연료개발팀의 박상규박사 및 팀원들인 형민, 제웅, 은희에게도 고마운 마음을 전합니다. 특히, 바쁜 시간 쪼개서 이것 저것 많이 도와준 형민아 고마웠어!

초등학교 동창이란 이름으로 20 년 가까이 만나고 있는 친구 작당들 (!), 우영과 정현, 그리고 대광에게 고마운 마음을 전합니다. 힘들 때 너희와 함께 한 술 한잔이 큰 위로이자 힘이 되었다. 앞으로도 꾸준히 함께 하길 바란다.

항상 빠질 수 없는 제 인생의 가장 중요한 사람들인 가족들, 특히 부모님에게 감사의 마음을 전합니다. 지난 30 년 넘는 세월동안 모든 정성으로 키워주신 덕분에 오늘의 제가 있게 되었습니다. 그리고 물심양면으로 많이 도와준 누나, 매형, 형, 형수 모두에게 깊은 감사의 마음을 전합니다. 삼촌, 외삼촌에게 많은 용기와 힐링을 주는 성환이, 소예, 승민, 예현이 모두 무럭무럭 자라서 큰 꿈을 가지며 살게 되길 바라며, 이 감사의 글을 마칩니다.

<div align="right">2015 년 1 월 가막골에서</div>

신상훈